



BEN-GURION UNIVERSITY OF THE NEGEV

THE FACULTY OF ENGINEERING SCIENCES

DEPARTMENT OF MECHANICAL ENGINEERING

Analysis, Modeling and Experiments of a Wave-Robot Locomotion in Various Environments

THESIS SUBMITTED IN PARTIAL FULFILLMENT OF THE REQUIREMENTS FOR
THE M.Sc. DEGREE

By: Lee-Hee Drory

Supervised by: Dr. David Zarrouk

November 2019



BEN-GURION UNIVERSITY OF THE NEGEV

THE FACULTY OF ENGINEERING SCIENCES

DEPARTMENT OF MECHANICAL ENGINEERING

Analysis, Modeling and Experiments of a Wave-Robot Locomotion in Various Environments

THESIS SUBMITTED IN PARTIAL FULFILLMENT OF THE REQUIREMENTS FOR
THE M.Sc. DEGREE

By: Lee-Hee Drory

Supervised by: Dr. David Zarrouk

Author: Lee-Hee Drory

Date: 19.11.2019

Supervisor: David Zarrouk

Date: 19.11.2019

Chairman of graduate studies committee:

ד"ר בני בר-און
יו"ר לימודי מוסמכים
המחלקה להנדסת מכונות

Date: 20.11.2019

November 2019

Abstract

This research presents the modeling, experimenting and motion analysis of a miniature wave-like robot named SAW: a Single Actuator Wave robot. The main goal of this research is to develop a miniature robot suitable for use in medical procedures in human body, like in the intestines, by reinventing and transforming the current design of the robot. We also aimed to perform extensive analysis of the robot's motion in various environments and determine under which conditions the robot can advance.

First, we review the first prototypes of the robot and evaluate the design specifications. The robot's structure and mechanical design are described, and we explain the motion mechanics of how the robot advances. We describe a number of models of the robot manufactured with different methods and materials.

Furthermore, we present an analysis of the robot's motion in different environments. We start by developing two locomotion models to characterize the cases where the robot advances in a straight environment: between two surfaces or on a single surface. For each model we specify the conditions in which the robot can advance. For motion on a single surface, we show that the robot advancement is not continuous and we use a simulation to demonstrate the advancing-sliding motion of the robot, affected by a number of parameters.

Next, we continue by analyzing the robot's motion between curved surfaces in different cases of orientation. We show the motion modeling in the different cases and the geometrical condition required from the robot to fit in different geometries of the surfaces, as well as a numerical simulation demonstrating the motion in the different cases.

Finally, we describe multiple experiments performed with different models of the robot to experimentally validate our simulation and analysis. We show the design and manufacturing of highly flexible tube-like shapes we developed from silicone rubber, as well as an experiment system designed to measure forces applied on the wave of the robot inside the flexible tubes. We then show multiple experiments conducted between compliant surfaces, inside flexible tubes and in pig's intestines, both straight and in curved shapes.

Key Words

Robotics; Wave robot; Wave locomotion; Motion modeling; Medical robot; Endoscopic robot; Compliant surfaces; Compliant tubes; Robot design.

Acknowledgments

First, I would like to express my gratitude to my supervisor, Dr. David Zarrouk, for the guidance and encouragement during my research and thesis writing. I would like to thank him for all the support, patient advice and the trust he placed in me.

A special thanks goes to my friends and colleagues, Dana Erez, Nir Meiri and Dan Shachaf, for the collaboration and brain storming on a daily basis, which made my work much more productive and fun than I thought it could be.

I would also like to thank my friends and fellow masters students for their support, the shared lunches and laughter during our time in the university and off it. I would like to thank my roommate and dear friend Noa Afik, for the constant support, the love and advice, and the chattering and presentation practicing through the nights during my studies.

Finally, I would like to thank my family for loving and supporting me and for providing me with continuous encouragement throughout my years of study and throughout the research process and the thesis writing.

Table of Contents

Nomenclature	v
List of Tables	vii
List of Figures	vii
1 Introduction	1
2 Background.....	3
2.1 Gastro-Intestinal Tract.....	3
2.1.1 The Structure of the Intestines	4
2.1.2 Locomotion inside the intestines	5
2.2 Previous Models of the SAW Robot	5
2.3 Wave parameters	7
2.4 Kinematic Analysis	8
3 Mechanical Design	9
3.1 Product Design Specifications.....	9
3.2 Robot's Structure and Components.....	9
3.3 Materials and Properties	12
3.4 Advancing Mechanics	13
3.5 Link Design	14
4 Analysis and Motion Modeling	16
4.1 Center of Mass.....	16
4.2 Motion between Two Surfaces.....	18
4.3 Crawling On a Single Surface	19
4.4 Crawling Between Curved Surfaces.....	22
4.4.1 Locomotion Definition.....	22
4.4.2 Geometrical Validity Conditions for the Cases	23
4.4.3 Case A of Orientation	28
4.4.4 Case B _I of Orientation.....	30
4.4.5 Case B _{II} of Orientation.....	34
4.4.6 Case C of Orientation.....	36
5 Motion Simulations	38
5.1 Crawling On a Single Surface	38
5.2 Crawling Between Two Curved Surfaces	42
6 Experiments	46
6.1 Motion Experiments in 2D	46

6.1.1	Experiment System: Flexible Surfaces	46
6.1.2	Experiments between Two Compliant Surfaces	46
6.1.3	Experiment of Motion on a Single Surface.....	48
6.2	Forces Measuring in Tubes	48
6.2.1	Propulsion and Resisting Forces	48
6.2.2	Experiment System: Forces Measurement Device for Flexible Tubes.....	50
6.2.3	The Experiments of Forces Measurement	52
6.3	Motion Experiments in Tubes	56
6.3.1	Experiment System: Flexible Tubes	56
6.3.2	Experiments of Motion inside Compliant Tubes	57
6.4	Motion Experiments in Pig's Intestines	58
7	Conclusions	62
8	References	63
9	Appendices	66

Nomenclature

Symbol	Units	Meaning
A	mm	Amplitude of the wave
a	mm	Perpendicular in a triangle formed in case C of orientation
AR	-	Advance Ratio
ATR	%	Advance Time Ratio – advancing time divided by the total time of motion
b	mm	Diagonal of the robot's length
D	mm	Distance between curved surfaces
d	mm	Distance between the COM and the start of the wave
f	Hz	Frequency of the helix's rotation
F_{ext}	N	External force applied on the robot
f_{ki}	M	Friction force at point i
F_{th}	N	Thrust force propelling the robot
$F_{thrust}^{(i)}$	N	Thrust force generated in case i
h_{COM}	mm	Height of the COM from the ground
k	rad/mm	Wave number
L	mm	Wavelength / pitch of the helix
l	mm	Total length of the robot
l_{A/B_I}	mm	The threshold length of the robot between cases A and B _I
$l_{B_I/B_{II}}$	mm	The threshold length of the robot between cases B _I and B _{II}
$L_{B_{II}/C}$	mm	The threshold length of the robot between cases B _{II} and C
L_c	mm	Advance of the robot in one helix rotation
L_{head}	mm	The length of the head of the robot
L_{link}	mm	Width of the links
$L_{segment}$	mm	The length of a segment of one link and a piece of the helix
L_{wave}	mm	The total length of the wave part of the robot
$m_{helix_per_link}$	gr	The mass of a segment of the helix
$m_{segment}$	gr	The mass of a segment of the wave
N_i	N	Normal force at point i
P	W	Power supply for the robot
R	mm	Radius of curved surfaces
r	mm	Height of the links
r_{in}	mm	Radius of the inner surface
r_{out}	mm	Radius of the outer surface

T	sec	Period of the sine wave
V_{link}	cm/sec	Speed of the tip of the link
V_{Robot}	cm/sec	Velocity of the robot
V_{wave}	cm/sec	Velocity of the wave
w	mm	Width of the wave/ the robot
W_b	gr	Weight of the battery
W_r	gr	Weight of the robot
x_1	mm	Distance between the COM and the contact point of the wave with the ground
x_2	mm	Distance between the COM and the contact point of the head with the ground
\bar{x}_{head}	mm	Center of mass location of the head
\bar{x}_{Robot}	mm	Center of mass location of the robot
\bar{x}_{wave}	mm	Center of mass location of the tail (wave)
α	degrees	Angle formed between the diagonal of the robot and the length vector of the robot (case B)
β	degrees	Angle formed between the outer radius and the diagonal of the robot (case B)
γ	degrees	Angle formed between the inner radius and the width vector of the robot (case B)
θ	degrees	Angle formed between the inner and outer radii (cases C,D)
μ	-	Friction coefficient
ρ	degrees	Angle between the robot and the tangent to the outer surface in the contact point
φ	degrees	Angle formed between the inner and outer radii (case B)
ω	rad/sec	Angular frequency

List of Tables

Table 5.1: Parameters considered in the single surface simulation	39
Table 5.2: Parameters considered in the curved surfaces simulation	44
Table 9.1: Design challenges and the solutions suggested	66
Table 9.2: Detailed mass and length values and the COM calculations	74
Table 9.3: Experiments results of the motion between two surfaces and inside tubes	85
Table 9.4: Calculated average and STD from the experiments data.....	86

List of Figures

Figure 1.1: The miniature SAW robot	2
Figure 2.1: Structure of the digestive system.....	3
Figure 2.2: The first two models of the SAW robot as presented by Zarrouk et al. [25]	5
Figure 2.3: Previous versions of the SAW robot	6
Figure 2.4: A helix function and its projection on XY, XZ planes.....	7
Figure 3.1: The SAW robot main components	10
Figure 3.2: The latest model of the robot.....	11
Figure 3.3: VeroWhitePlus printed parts	12
Figure 3.4: Parts of the robot manufactured in brass	12
Figure 3.5: The lasted designs of the robot, brass helix and Vero links (Model 7v), and a model with brass links and helix (Model 7b).....	13
Figure 3.6: Side view of the wave. The contact point with the ground sticks to the ground and causes the robot to advance.	13
Figure 3.7: Link structure	14
Figure 3.8: Front and isometric view of the three link designs, showing the spaces between the spikes to avoid collision of the links during motion.	15
Figure 3.9: a) The flexible structure of the links joined by a nylon wire (outlined in yellow). b) Narrow end of the wave (top view) to allow smoother movement backwards.	15
Figure 4.1: Sketch of the center of mass parameters	17

Figure 4.2: Free body diagram of the robot crawling between two surfaces. N is the normal force, f_k is the friction force at the contact points of the robot with the surfaces and F_{ext} is an assumed external force.	18
Figure 4.3: Free body diagram of the robot on a single surface, considering normal and friction forces, the weight of the robot and an external force.	20
Figure 4.4: Curved surfaces with radius R , distance D between the surfaces, inner radius r_{in} and outer radius r_{out} , with the robot with length l and width w	22
Figure 4.5: Four cases of the orientation of the robot while placed between the two curved surfaces	23
Figure 4.6: The condition for validation of case B	24
Figure 4.7: Threshold length of the robot between cases A and B _I	24
Figure 4.8: The geometry of the robot with a tangent contact point with the inner surface	25
Figure 4.9: Threshold length of the robot between cases B _I and B _{II}	25
Figure 4.10: The geometry of the robot in case C between the surfaces	26
Figure 4.11: Threshold length of the robot between cases B _{II} and C	26
Figure 4.12: Diagram of length threshold conditions between the cases of orientation....	27
Figure 4.13: Case A of crawling between curved surfaces, contacting the outer wall, rotating outward and advancing.....	28
Figure 4.14: Case A of crawling between curved surfaces, contacting the outer wall, rotating inward and stopping	28
Figure 4.15: Case A, the robot touching the outer surface	29
Figure 4.16: The robot crawling between curved surfaces in Case B _I , (a) crawling freely between the surfaces and contacting the surface in a single corner, (b) rotating inwards around the corner and generating two contact points in the corners of the robot.....	30
Figure 4.17: The robot between the surfaces in Case B _I after inward rotation, with touching corners. The radii of the surfaces and the robot's diagonal create a triangle.....	31
Figure 4.18: The robot crawling between the surfaces in Case B _I , with the corners of the robot contacting the tube walls	32
Figure 4.19: Critical μ values for case B _I	33
Figure 4.20: The robot crawling between the surfaces with two contact points with the outer and inner surfaces (case B _{II})	34
Figure 4.21: Critical μ values for case B _{II}	35
Figure 4.22: The robot crawling between surfaces with three contact points (case C)	36

Figure 5.1: Pseudocode of the motion simulation on a single surface. x_2 is constant and equals the distance between the COM and the contact point of the head with the ground. x_1 is the distance between the COM and the contact point of the wave with the ground, which is varying with time.	38
Figure 5.2: Simulation of the robot's movement on a rigid surface (also see video). Left – COM location closer to the head (sliding time of 0.34 cycle, right – COM location closer to the wave. The sliding time	40
Figure 5.3: The advance time ratio (ATR) of the robot in the simulation with different ratios of the head and wave COFs.	41
Figure 5.4: Pseudocode of the motion simulation between curved surfaces.	43
Figure 5.5: Screenshots from the curved surfaces simulation. From top to bottom: case A, case B _I , case B _{II} , case C. Three different frames for each case – time advancing in the frames from left to right.....	45
Figure 6.1: Flexible surfaces with a mesh structure	46
Figure 6.2: The robot moving between two flexible surfaces (left) and curved surfaces (right).	47
Figure 6.3: The robot moving on a rigid surface. The robot is partly moving and partly sliding, as predicted in the simulation.....	48
Figure 6.4: Cross-section of the links inside a tube in three different cases of contact between the robot and the tube: (a) collapsed tube-like surfaces, (b) corner contact points and (c) tightly inserted.	49
Figure 6.5: The force measurement experimental system that enables stretching the silicone tube and measure the forces acting on the waves, CAD model and the built system.....	50
Figure 6.6: Three-piece wave models that demonstrate the robot's wave. The transparent parts show the location of the yellow wave after stretching. Top: Normal stretching waves. Bottom: Sideways stretching waves.	52
Figure 6.7: Experiment with a 2mm-wall-thick tube. Front view (up) and top view (down) showing the tube in the starting position and in the stretched position. a) Normal stretching waves. b) Side stretching waves.	53
Figure 6.8: Results of the force measured in the experiment, for the normal waves (left) and the side waves (right)	54
Figure 6.9: Forces measured in the experiment in the normal direction vs. sideways. The solid line corresponds to $F_{normal}/F_{side}=1$, showing that the normal forces are always larger than the side forces.....	54
Figure 6.10: Top - 3D model of the molds. Bottom – a mold and the flexible tubes	56

Figure 6.11: The robot moving inside a 1 mm thick tube (left) and in a curved 1 mm thick tube (right)	57
Figure 6.12: First experiment in pig's intestines, model 5.	59
Figure 6.13: Second experiment in pig's intestines, straight shape with model 7b.....	60
Figure 6.14: Second experiment in pig's intestines, model 7v	60
Figure 9.1: The latest design of the robot prior to this project	67
Figure 9.2: The first improvement made in the robot - round links (model 1).....	68
Figure 9.3: Design with the concept of using a nylon wire to connect the links (model 2)	68
Figure 9.4: Demonstration of the twisting movement	69
Figure 9.5: Added bumps to eliminate the twisting motion (model 3).....	69
Figure 9.6: Creating one-piece links (model 4) and adding spikes to increase the robot's velocity (model 5)	69
Figure 9.7: Front and isometric view of the three link designs, showing the spaces between the spikes to avoid collision of the links during motion	70
Figure 9.8: Model 6 of the robot, improved by narrowing the head and adding fillets	70
Figure 9.9: Metal helixes with different parameters	70
Figure 9.10: Left: Three models of the end links, Right: Top view of the end of the wave	71
Figure 9.11: Left – CAD model of the robot with narrow tail (model 7), Right – the assembled robot with the added special links in the end of the wave.....	71
Figure 9.12: The final model of the robot, with brass helix and links	71

1 Introduction

Bioinspired crawling robots have been the topic of numerous studies and research groups in the last few decades. Their applications range from pipe maintenance to search and rescue purposes and crawling inside the biological vessels of the body.

When designing and developing crawling robots, two main locomotion methods have been investigated: inch-worm-like locomotion [1]-[23], and undulating locomotion which resembles a continuously advancing wave, among which we can find modeling and exploration of wave motion as well as snake inspired and wave producing robots [24]-[40]. Both methods feature various types of robots and locomotion mechanisms, including multiple links robots, mesh-wave structures [22],[41]-[43], pneumatic activated actuators [9],[44] and even origami robots [45]-[47]. One of the most common approaches to robot design is the minimalistic approach; i.e., a small number of motors and actuators, which is sometimes hard to implement when engaging in developing bio-inspired robot.

In these applications, the robots sometimes need to crawl over anisotropic and flexible terrains with varying surface properties, and respond with flexibility to different coefficients of friction and dimensions. More specifically, many researchers has recorded investigation and multiple experiments on properties and mechanics of the human intestines [48]-[52], in order to lay the groundwork for creating endoscopic capsules and robots.

Additionally, intestinal exploration oriented robotic capsules are being developed [47],[54]-[56], although currently the only commercialized product is the PillCam™ [57], that is a camera equipped swallowable capsule that moves naturally through the intestines using only the peristaltic motion of the bowels. With the recent focus on the robotic capsules, some researchers started conducting medical studies to evaluate the efficiency, advantages and future applications of robotic capsule assisted medicine [58]-[62].

Inspired by the wave-like locomotion of snakes and flagella and swimming patterns of miniature organisms, Zarrouk et al. previously presented the first Single Actuated Wave robot (SAW) [25], which is the first robot in the world that can generate a wave motion using only one motor. SAW generates its advancing wave by the combination of a rotating helix and a large number of links attached to each other by rotational joints. The first 25 cm long SAW robot successfully advanced over different surfaces and reached a maximum

speed of 57 cm/s. Because of the single motor, the robot can be miniaturized and adjusted to serve in future applications in medical procedures.

In this thesis, our focus is on the dynamics of locomotion of a miniature version of the SAW robot (Figure 1.1). Specifically, we investigate the conditions in which the robot can produce thrust and advance over flat surfaces, curved surfaces and inside tube-like flexible environments. In section 2, we present a short background of the human intestines and mathematical models to better understand the robot's operation and structure. In section 3, we present a description of the design of the miniature version of the robot, including the robot's structure, advancing mechanics and materials used for manufacturing. In section 4, we perform a dynamic analysis of the locomotion of the robot, crawling in different configurations and environments, and in section 5 we simulate the robot's motion using a numerical simulation. Finally, in section 6 we present multiple experiments we performed using the robot in different crawling conditions, as well as a forces measuring experiment designed to measure the forces applied on the robot while crawling inside a tube.

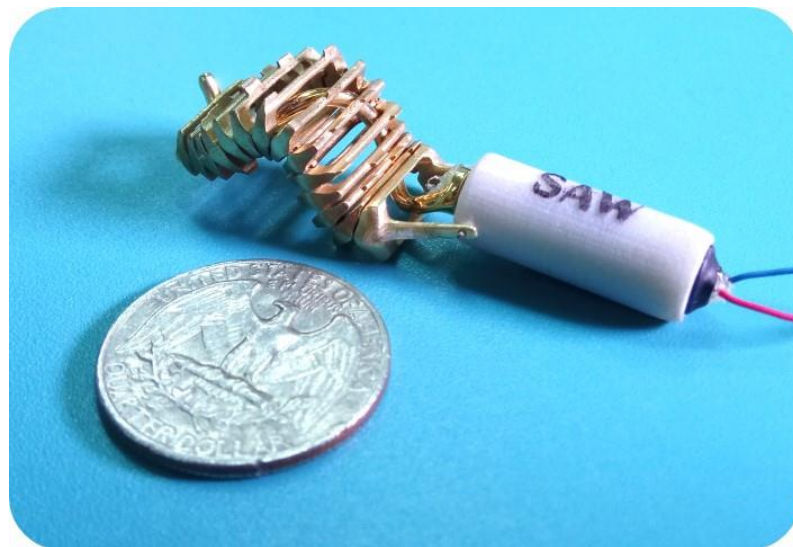


Figure 1.1: The miniature SAW robot

This research was published and presented in the International Conference on Robotics and Automation (ICRA), that took place in Montreal, Canada, under the title “Locomotion Dynamics of a Miniature Wave-Like Robot, Modeling and Experiments” **שגיאה! מקור**. Additionally, we presented this research in the 35th Israeli Conference on Mechanical Engineering (ICME 2018) and in the 6th Israeli Conference on Robotics (ICR 2019). **ההפניה לא נמצא.**

2 Background

This section reviews some theoretical and mathematical background relevant for this research, as well as medical background on the human intestines.

2.1 Gastro-Intestinal Tract

The main purpose of our digestive system is to break down food to molecules that can be absorbed in the cells [63]. The digestive system starts in the mouth and ends in the anus, forming a tubular system about 5-7 meters in length, which consists of two main parts: the gastro-intestinal tract (GI) and accessory digestive organs. The GI includes the mouth, esophagus, stomach, small intestine and large intestine, as shown schematically in Figure 2.1.

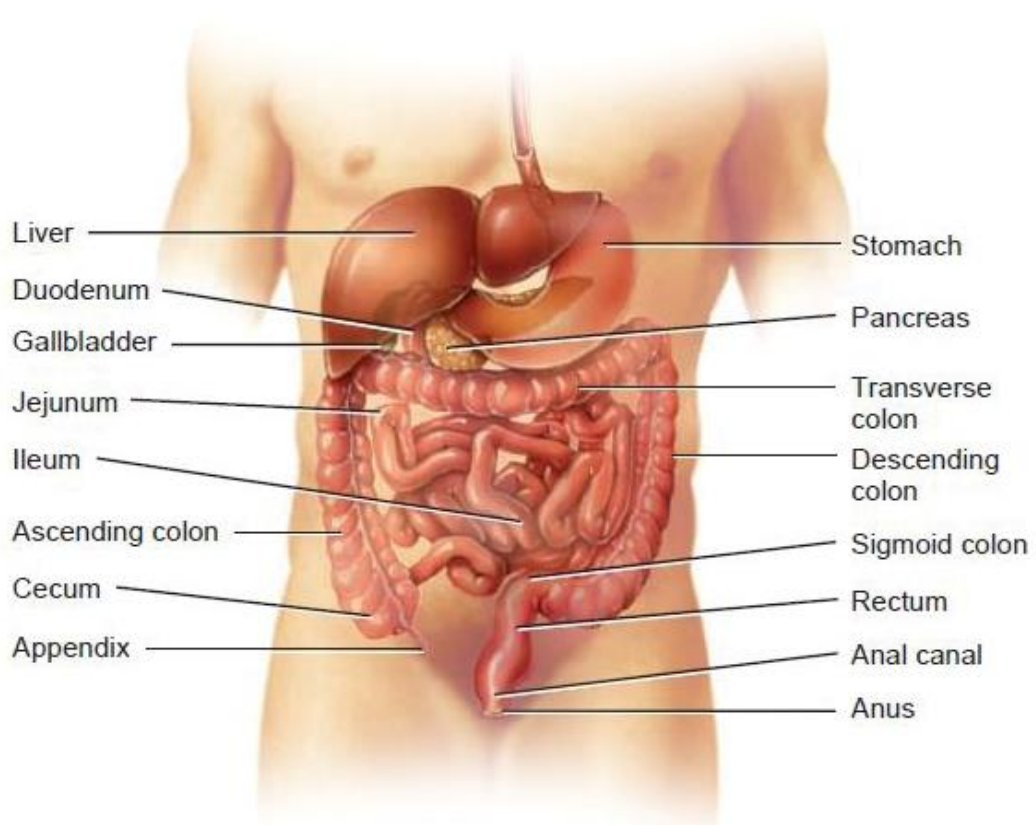


Figure 2.1: Structure of the digestive system

Among other domains, this study will explore the locomotion on various surfaces including compliant surfaces and inside the intestines, therefore the next section will elaborate on the intestines' structure and characteristics.

2.1.1 The Structure of the Human Intestines

The bowels are a viscoelastic tissue (i.e. they are very elastic, yet they possess the prominent qualities of viscous material and absorb stress) that connect directly to the stomach, starting with the small intestine (which consists of duodenum, jejunum and ileum), through the large intestine (cecum and colon) and ending in the rectum and anus.

The small intestine is about 3m in length with a diameter of 2.5cm, in which most of the digestion process takes place. This is a soft tissue that will collapse if empty, thus an additional force is required from a robot to separate the adhering of the walls sufficiently for passage. The exterior layer of the wall of the intestines, called the mucosa, is composed of an outer layer of epithelial cells, a layer of connective tissue and a layer of smooth muscles creating small folds in the intestinal wall. There are cells in the mucosa that secrete mucus and fluids to the inside of the intestine, about 1-2 liters each day.

The intestines move constantly to push the food forward. First, the intestines move to mix the food with the fluids and allow contact with the mucosa. Then peristalsis motion (contraction and relaxation of the intestine wall's muscle) cause the advance of the food along the intestines.

The large intestine is the final section of the intestines, measured 1.5m long and about 6.5cm in diameter. Its overall function is to complete absorption of the liquidated food and discharge feces from the body. The first section is the cecum, followed by the colon, both have the same layer of mucosa as the rest of the GI tract, as well as perform similar peristalsis movements.

2.1.2 Locomotion inside the intestines

As mentioned above, all the intestines tissue is viscoelastic and very flexible, thus presenting a major challenge in generating a movement of a robot inside the intestines. Furthermore, we must consider the secreted liquids and the resulting sliding that will occur inside the intestines. In fact, Kim et al. [52] tested the friction coefficient (COF) of a capsule inside pig's intestines by changing different parameters, and found that the COF changes with the change in the following parameters: the COF slightly increases with the increase of the capsule's speed; Surface area of the capsule has minimal effect on the COF; Higher weight of the capsule decreases the COF significantly. Therefore, by increasing the robot's speed and making it light weighted – the COF will increase so that the robot can move faster, since high friction of the wave with the intestines will create a larger thrust force, as will be explained later.

The calculations and analysis presented in this work consider only rigid surfaces, as a way to understand the robot's motion. This is also a preparation for further analysis of motion on different types of surfaces and in different environments, with inclusion of sliding and viscoelastic qualities of the surfaces.

2.2 Previous Models of the SAW Robot

The SAW – Single Actuator Wave robot, was first presented by Zarrouk et al. (2016) as the first robot in the world that produces a wave motion using a single actuator [25].

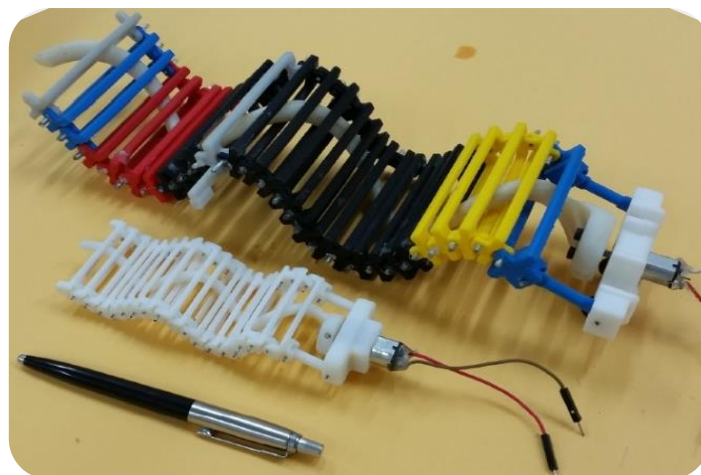


Figure 2.2: The first two models of the SAW robot as presented by Zarrouk et al. [25]

The basic mechanical design consists of a rotating helix that moves a set of links in a wave motion that advances the robot. The helix is connected to a motor that is secured in the head. The head also has a connection point to the links. In section 3.2 the robot's structure is described in detail.

There are five old models of the robot as shown in Figure 2.3.



Figure 2.3: Previous versions of the SAW robot

The first model (left in Figure 2.3) of the robot is 3D printed using mostly ABS material and is about 35cm long. All the other models were created using Polyjet 3D printing [D]. The second and third models were mostly created by Nir Dgani, built as 50% and 30% the size of the larger robot, respectively. The two models on the right, the latest models, were created by Ayelet Karp and Oshra Elcobi, and they are about 8cm long. The latest model was tested for movement between flexible surfaces and inside pig's intestines, but these experiments were only partially successful, as the robot moved relatively slowly between the flexible surfaces (maximum speed of 0.25 cm/sec) and it was not able to advance inside the intestines at all.

This research is a continuance of the past research performed in Dr. Zarrouk's lab and will focus in part on transforming the latest design and creating a smaller model of the robot that will be able to successfully and efficiently advance in pig's intestines.

2.3 Wave parameters

Considering a 3D helix function:

$$r(x) = \{x, y, z\} = \{x, A\sin(x), A\cos(x)\}, \quad (1)$$

where A is the amplitude of the helix and x is the space coordinate. The projections of this helix on the X-Y and X-Z planes are:

$$\begin{aligned} r(x)_{XY} &= \{x, A\sin(x), 0\} \\ r(x)_{XZ} &= \{x, 0, A\cos(x)\} \end{aligned} \quad (2)$$

Thus, this projection is generating a sine wave, as shown in Figure 2.4.

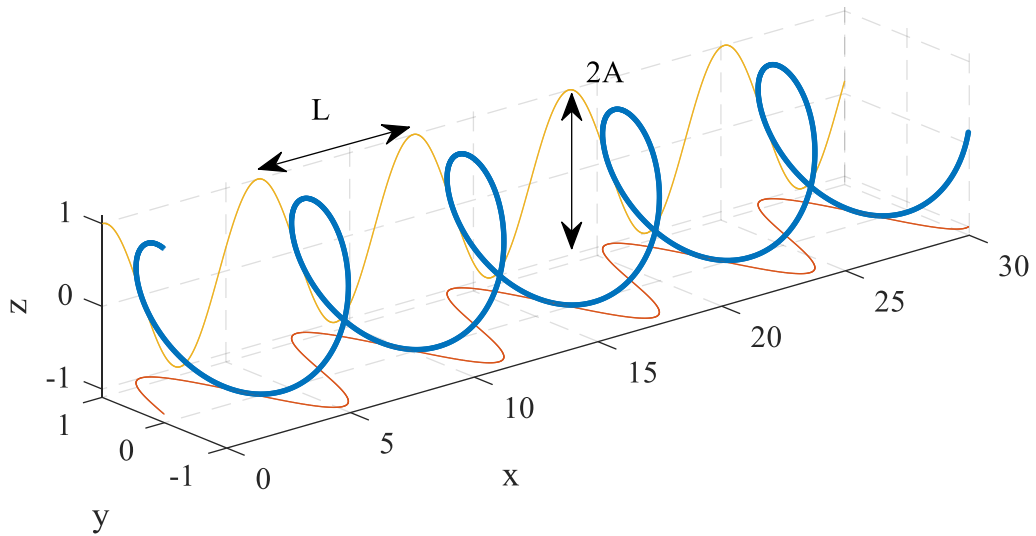


Figure 2.4: A helix function and its projection on XY, XZ planes

By using this principle, if we create a rotating helix, we can create a projection of an advancing sine wave. While considering desired wave parameters, an advancing wave could be described as:

$$y(x,t) = A \sin(kx - \omega t) = A \sin\left(2\pi \left[\frac{x}{L} - f \cdot t\right]\right), \quad (3)$$

Where ω is the angular velocity of the rotating helix, k is the wave number ($k=2\pi/L$), L is the wavelength (and the pitch of the helix), f is the rotating frequency (while $\omega=2\pi f$) and t is the time.

2.4 Kinematic Analysis

As presented by Zarrouk et al. (2016) for previous designs, this section reviews modeling of the kinematics of the robot and the links and calculation of the robot's velocity.

Where L (wavelength) denotes the advance of the wave in one rotation, the advancing speed of the wave is

$$V_{Wave} = f \cdot L . \quad (4)$$

Similarly, we specify L_c as the total advance of the robot in one rotation of the helix, since the actual speed of the robot can be adjusted by changing the robot's geometry, as will be explained later. Thus the speed of the robot is

$$V_{Robot} = f \cdot L_c . \quad (5)$$

With equations (4) and (5) we define the Advance Ratio (AR) of the robot:

$$AR = \frac{V_{Robot}}{V_{Wave}} = \frac{L_c}{L} . \quad (6)$$

In order to increase the velocity of the robot, we need to increase the advance ratio, thus causing the robot to advance faster than the speed of the wave, which is also the speed of the tip of the link that is touching the ground. With further analysis, the velocity of the tip of the link can be obtained:

$$V_{Link} \approx (2\pi)^2 \frac{A \cdot r}{L} f , \quad (7)$$

Where V_{Link} is the speed of the tip of the link touching the ground, A is the wave's amplitude and r is the link's height. See sections 3.4 and 3.5 for further explanation.

3 Mechanical Design

This section specifies the mechanical design of the robot and its main parameters, as well as the materials used for the robots and the design specifications. A full description of the design process is shown in appendix [A].

3.1 Product Design Specifications

As mentioned earlier, the design of the SAW robot is based on previous designs of the robot and required several improvements. The requirements are listed below:

- **Small dimensions:** the robot is destined to be used in medical procedures in human intestines, therefore it is required to be minimized. Current models of the robot are not compact enough for such purposes.
- **Easy to assemble:** the latest models of the robot were very difficult and intricate to assemble, so there was an eminent need to simplify the manufacturing process.
- **Mobility and speed:** By examining previous models, it was clear that the robot needs a better grip and friction with the surroundings to advance in the intestines, as well as increased velocity to obtain a reasonable procedure duration.
- **Durability:** the robot must be able to withstand reasonable forces caused by the peristaltic motion of the intestines and pressure from internal organs, as well as to apply enough force on the inner walls to help it advance on slippery surfaces.

3.2 Robot's Structure and Components

This chapter presents the general structure of the SAW robot to better understand its operation. The robot is composed of a motor housing and a wave-producing tail (Figure 3.1). A 6 mm DC motor rotates a helix. The tail is composed of several links, which are attached to each other through simple rotating joints. As the helix rotates, the links (which act like a 2D projection of the helix) produce a wave-like form of locomotion. The robot's motion direction can easily be reversed by inverting the rotation direction of the motor.

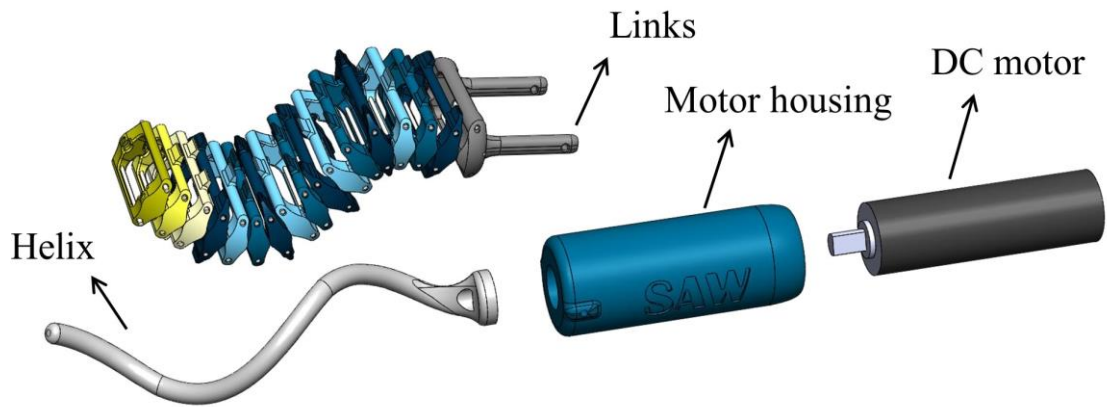


Figure 3.1: The SAW robot main components

- **Motor Housing**
The head's purpose is to contain the motor and provide a connection base for the first link. The design of the head is meant to be as short and narrow as possible, in order to minimize the interruption to the robot's movement, due to the wave solely performing all the motion.
- **Helix**
The helix creates the wave movement by rotating while attached to the motor. The helix is modeled with a specific wavelength and amplitude, while only the beginning of the helix (close to the head) has a smaller amplitude to allow free movement of the first link.
- **Links**
The links are designed to be moved by the rotating helix and advance the robot. The links have a general shape of a thin-walled rectangle that holds the helix inside, while the outer frame is built to connect the links to each other. A detailed description of the links' structure is shown in section 3.5.
- **DC motor**
The motor used for the propulsion is a 6 mm DC coreless motor (Precision Microdrives™, model 206-108 [B]), used to rotate the helix. The length of the motor is 21 mm, it has gear ratio of 699.5:1 and rated load of 10 mNm.



Figure 3.2: The latest model of the robot

- Power supply

The motor is operated using a DC power supplier or a small 3.7 V battery. The voltage that was used to power the robot with the power supplier is 4-5.5 V (higher voltage desired for faster rotation), while the operation requires 30-40 mAh, thus the assumed maximum power requirement of the robot is

$$P = V \cdot I = 5 \cdot 0.04 = 0.2W , \quad (8)$$

assuming voltage of 5 V. For an estimated procedure duration of about 30 minutes, wireless operation will require a battery of only 20 mAh. The approximated weight of the battery is then

$$W_b = \frac{20mAh}{110mAh} \cdot 3g = 0.55g , \quad (9)$$

while a 110-mAh battery weights 3 g., so the weight that will be added to the robot will be relatively small to allow the total robot's weight to be minimized.

3.3 Materials and Properties

The first models of the robot were 3D printed with Objet350 Connex3 3D printer [C] using VeroWhitePlus [D] as printing material. Figure 3.3 shows a number of printed parts that were printed in this method.

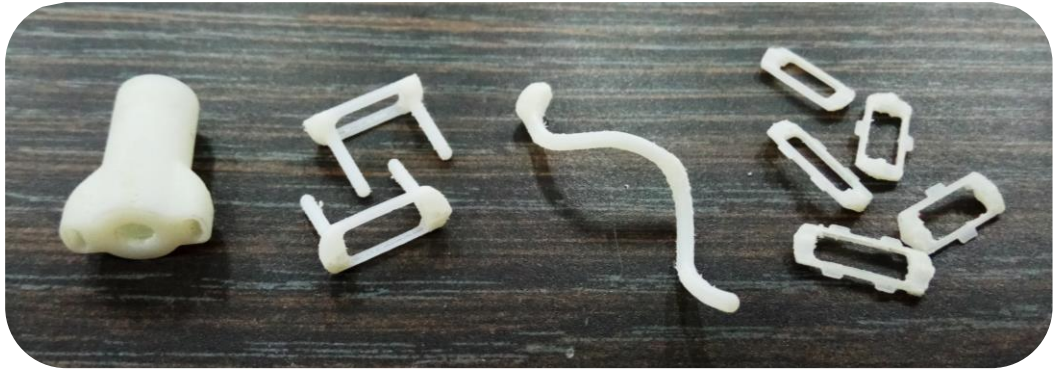


Figure 3.3: VeroWhitePlus printed parts

The latest design manufactured in Vero weighs only 3.4 g, including the motor, its length is 63 mm with width of 15 mm.

The links and helix of the newer models of the robot are manufactured in brass, to make it stronger and more durable. The brass alloy is composed of 80% copper, 15% zinc and 5% tin. Figure 3.4 shows the links and helix made of the brass alloy.



Figure 3.4: Parts of the robot manufactured in brass

For a model of the robot with Vero links and a brass helix, the robot weighs 4.6 g (will be referred to as model 7v, see Figure 3.5), with 13 links assembled. For the model of the robot with brass helix and links, the robot weighs 8.4 g (will be referred to as model 7b, see Figure 3.5), with 15 links assembled. The robot's maximum width is 15 mm, and its total length is 57 mm when composed of 13 links.

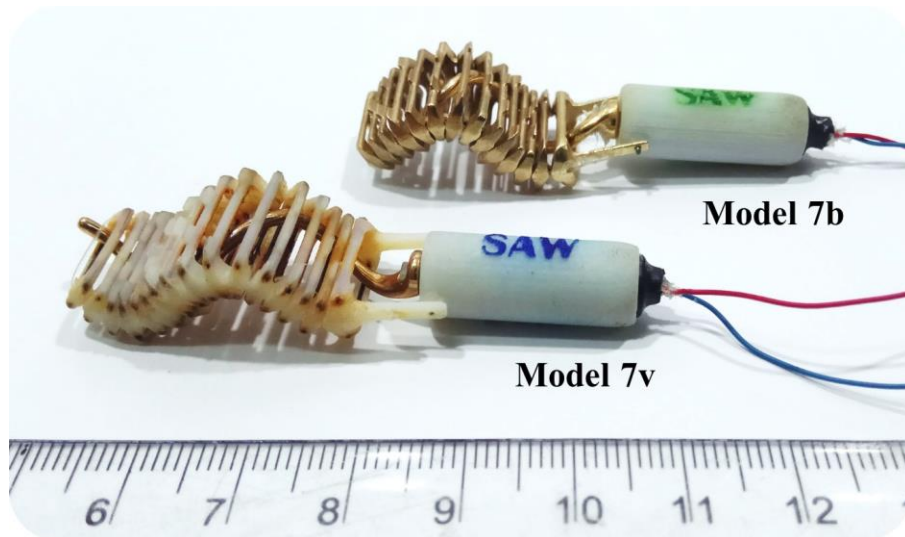


Figure 3.5: The lasted designs of the robot, brass helix and Vero links (Model 7v), and a model with brass links and helix (Model 7b).

3.4 Advancing Mechanics

As mentioned before, by increasing the speed of the tip of the links in the wave, we can increase the advancing speed of the entire robot. To better understand why, we look at the wave from the side view:

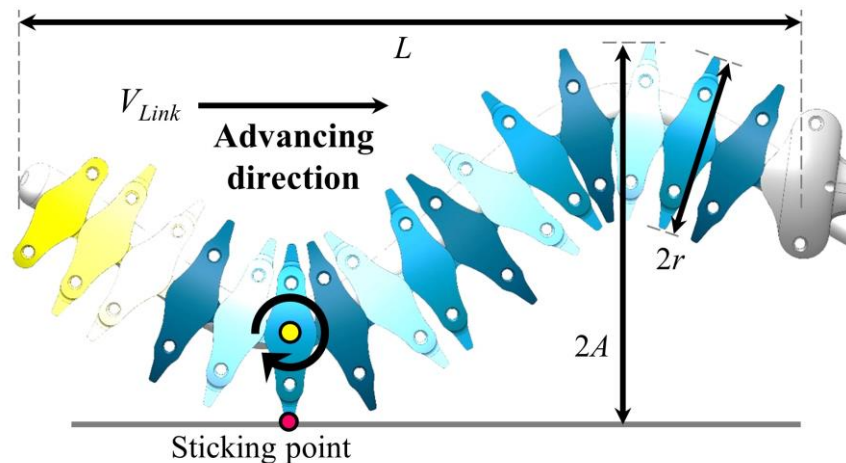


Figure 3.6: Side view of the wave. The contact point with the ground sticks to the ground and causes the robot to advance.

The links are assembled on the helix and are forced to move up and down with the helix's rotation, and thus they each rotate around their middle point when they move (yellow dot in Figure 3.6). When a link touches the ground it creates a sticking point (red dot in Figure 3.6), causing the link that is currently touching the ground to push the robot forward and advance. The velocity of this point is the velocity of the tip of the link (7), and therefore also the velocity of the robot (assuming no sliding).

According to (7), if $A \cdot r/L$ is increased it will result in higher velocity as was presented by Zarrouk et al. (2016) [25]. Respectively, if the height r is increased, the radius of the rotation around the yellow middle point will increase, and therefore increase the speed of the robot.

However, increasing this parameter could cause collision of the links, e.g. if we increased r , it will cause the top of two adjacent links to collide during motion. To overcome that we create three different models of the links to avoid collision, as will be explained in the next subsection 3.5.

3.5 Link Design

As mentioned, the links are assembled on the helix and produce the wave shape, while the basic link structure is a hollow rectangle to hold the helix. The links are then attached together to create a flat formation that is flexible enough in one direction to be modified to a sine shape and move with the rotating helix, but still rigid enough in a different direction to enable movement of the robot and maintain the wave shape. As shown in the next figure, a link has two main parameters:

- $r =$ the height of the link, from the center to the tip of the link.
- $L_{Link} =$ the width of the links, from one contact point with the previous link to the other contact point with the next link.

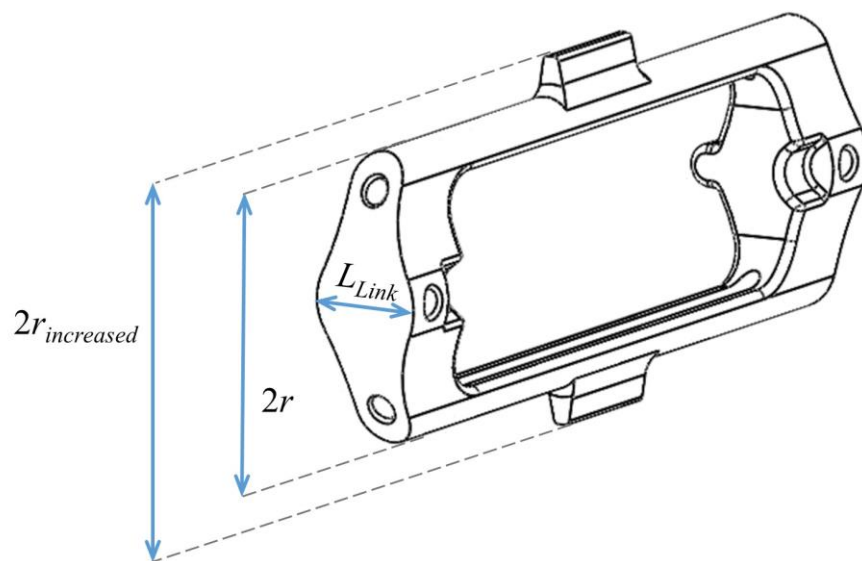
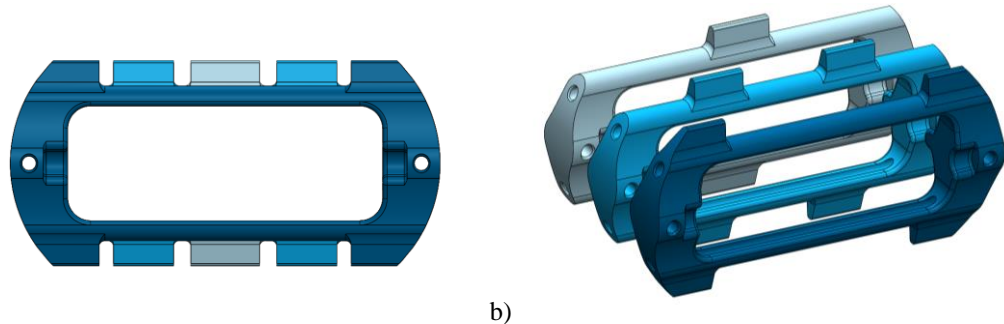


Figure 3.7: Link structure

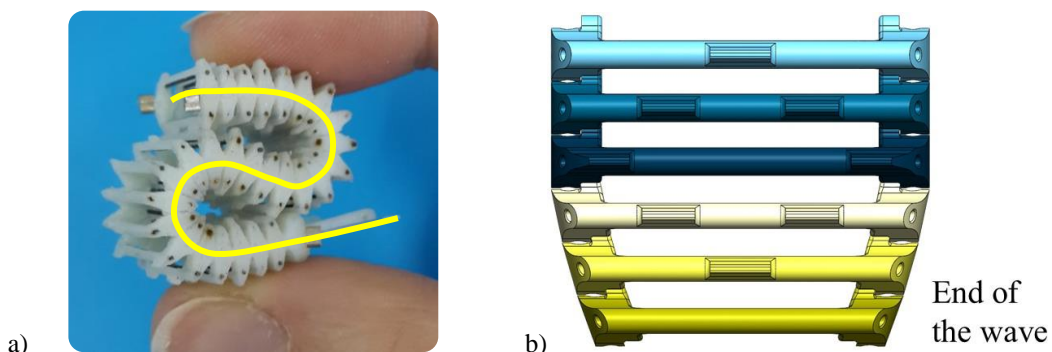
As mentioned in the last subsection, we want to increase r and therefore created spikes on top of the links ($r_{increased}$) to increase the link velocity. These spiked links were produced in three different models, allowing the spikes to integrate with each other and avoid collision (see Figure 3.8).



a) b)
Figure 3.8: Front and isometric view of the three link designs, showing the spaces between the spikes to avoid collision of the links during motion.

The links have a 0.45 mm diameter hole for the insertion of a nylon wire, used for attaching the links together. The wire goes through the entire tail from front to back and is clipped at the ends and allows flexibility of the tail (see Figure 3.9a).

They have another set of 0.45 mm holes to hold 0.4 mm pins, used to strengthen the thinnest part of the link and reduce the friction between the links and the helix (In the newest model of the robot, where the links are all 3D printed in brass, these holes are redundant on account of the brass' strength). The links also have bumps that fit together, preventing a degree of freedom of moving up and down relatively to each other, thus eliminating a twisting motion resulted by using the wire. The end of the tail is comprised of customizes links that are narrower than the entire wave, to allow a smoother motion backwards (Figure 3.9b).



a) b)
Figure 3.9: a) The flexible structure of the links joined by a nylon wire (outlined in yellow). b) Narrow end of the wave (top view) to allow smoother movement backwards.

4 Analysis and Motion Modeling

To evaluate the robot's motion in different environments and configurations, we performed analytical analysis and developed several locomotion models. This section reviews the analysis and modeling of motion in various configurations, including analysis of the center of mass (COM), modeling of the robot's motion on a single surface or between two surfaces and also between curved surfaces. The analysis is performed on rigid surfaces and sliding of the links on the surfaces is neglected.

4.1 Center of Mass

To calculate the COM of the robot we refer to the head and the wave separately. To obtain the wave's COM we calculate a 'wave segment mass', which is the mass of a segment comprised of a link, 2 pins and the mass of a segment of the helix (or without the pins for the latest model comprised of brass links):

$$m_{segment} = m_{link+2\ pins} + m_{helix_per_link} \cdot \quad (10)$$

$m_{helix_per_link}$ is calculated using the helix's material density and the volume of a segment on which there is a link assembled.

We neglect the structural difference of the first and last links and the COM varying in time. Thus, measured from the top of the head, the COM will be:

$$\bar{x}_{Robot} = \frac{\sum \bar{x}_i m_i}{\sum m_i} = \frac{(\bar{x}m)_{head} + (\bar{x}m)_{wave}}{m_{head} + m_{wave}} = \frac{(\bar{x}m)_{head} + \bar{x}_{wave} \cdot n \cdot m_{segment}}{m_{head} + m_{wave}}, \quad (11)$$

while n is the number of links assembled on the helix, m_i is the mass of part i and \bar{x}_{head} is the COM location of the head, equal to half of the head's length. \bar{x}_{wave} is the COM location of the wave, and is calculated as follows:

$$\bar{x}_{wave} = L_{head} + 0.5L_{wave} = L_{head} + 0.5 \cdot n \cdot L_{segment} \cdot \quad (12)$$

Figure 4.1 shows the parameters mentioned above and the location of the COM:

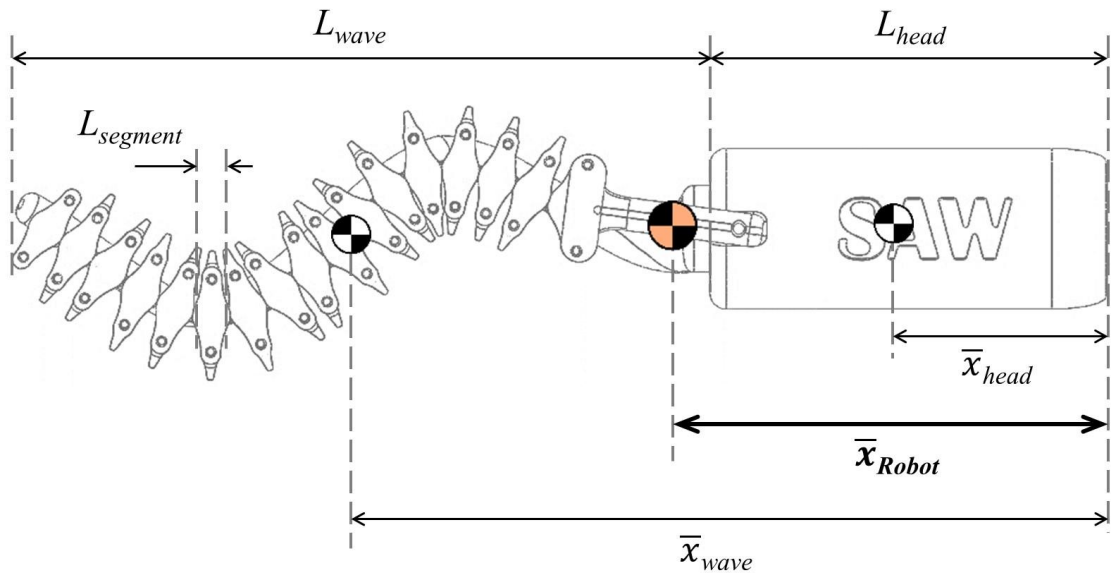


Figure 4.1: Sketch of the center of mass parameters

Using (10)-(12), we calculated the COM location of the robot. The COM location of model 7v was calculated to be 24 mm from the start of the head, while the location for model 7b was 30 mm. This is consistent with an estimation from a manual measurement of 25 and 30 mm, respectively. A detailed table of the calculations of the COM is shown in appendix [E].

4.2 Motion between Two Surfaces

When modeling the motion, we need to obtain the advancing conditions allowing the robot to push forward, to establish what drives the robot. We start our analysis with the case in which the robot is crawling under the influence of a resisting external force F_{ext} between two surfaces (see Figure 4.2). The two surfaces apply normal and friction forces on the wave and the head of the robot.

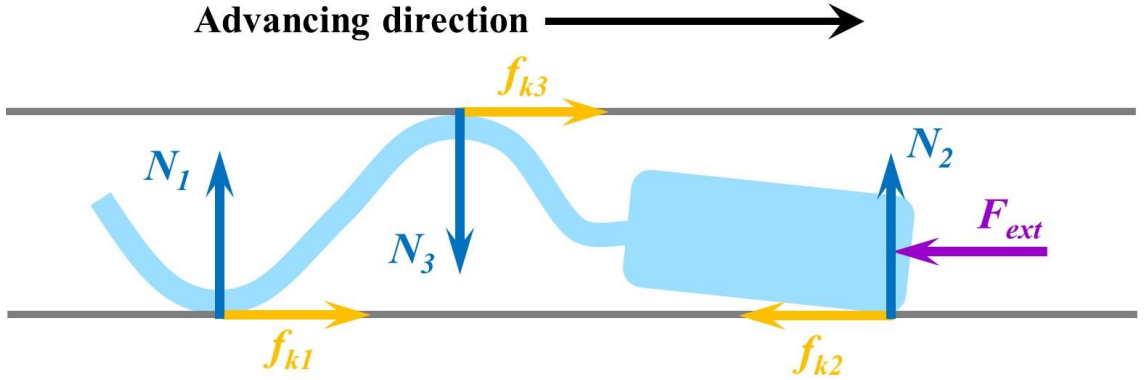


Figure 4.2: Free body diagram of the robot crawling between two surfaces. N is the normal force, f_k is the friction force at the contact points of the robot with the surfaces and F_{ext} is an assumed external force.

To simplify our analysis, we use the simple Coulomb friction model:

$$f_{k_i} \leq \mu_i N_i, \quad (13)$$

where f_{k_i} is the absolute value of the friction force acting at point i , and μ_i and N_i are respectively the coefficient of friction (COF) and the normal force acting on the surface at point i . Note that the equality of (13) only holds during sliding.

Assuming that the motor housing's diameter is smaller than the height of the wave, the robot will contact the two surfaces at three distinct points. The wave will contact the surface at points 1 and 3, providing the thrust forces (f_{k1} and f_{k3}), since the friction force of the links with the surface cause the robot to advance (see section 2.4). However, contact point 2 of the motor housing with the surface (f_{k2}) resists the motion, along with the external force. Neglecting the weight of the robot, the sum of the forces in the normal direction is:

$$\Sigma F_y = N_1 + N_2 - N_3 = 0, \quad (14)$$

where N_1 , N_2 and N_3 are the absolute values of the normal forces at the contact points 1, 2 and 3. (14) becomes:

$$N_1 + N_2 = N_3. \quad (15)$$

Assuming quasi-static locomotion; i.e., zero acceleration, the net force in the horizontal direction must fulfil

$$f_{k1} + f_{k3} > f_{k2} + F_{ext} \quad (16)$$

for the robot to advance, considering an external force F_{ext} . Assuming identical COF μ over all contact points and using (13), we obtain from this equation the condition:

$$N_1 + N_3 - N_2 > \frac{F_{ext}}{\mu}. \quad (17)$$

Inserting (15) into (17),

$$2N_1 > \frac{F_{ext}}{\mu}. \quad (18)$$

If we assume a relatively small resisting external force, Eq. (18) is always satisfied, which implies that the robot will always advance when placed between two surfaces. Experiments performed while the robot is crawling between two surfaces are presented in section 6.1.2 (also see video).

4.3 Crawling On a Single Surface

The next case we analyze is the motion on a single surface, in which, when considering the weight of the robot, the motion is affected by the robot's geometry and the position of its center of mass (COM). In this case, the wave has a single contact point with the surface (as presented in Figure 4.3). The forces acting on the robot are its own weight, the thrust force produced by the wave contacting the ground (f_{k1}), and the two resisting forces: the friction force f_{k2} and the external force F_{ext} , similarly to the previous case. Note that while contact point 2 is always at the tip of the motor housing, contact point 1 varies as a function of time. Therefore, the distance between the COM and the contact point of the head with the surface is constant, and the distance between the COM and the contact point of the wave with the surface varies with time. The maximal change in the COM location during locomotion is 1 mm and therefore it is neglected.

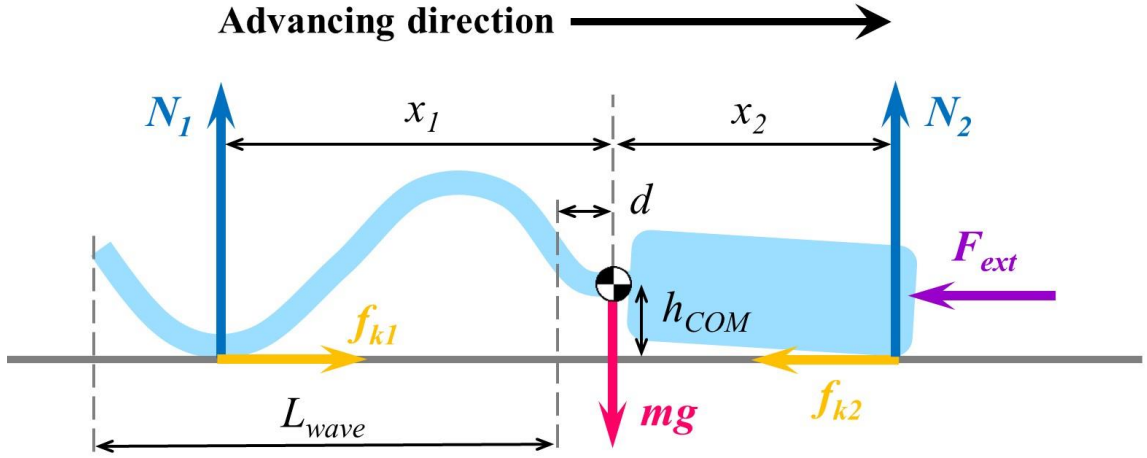


Figure 4.3: Free body diagram of the robot on a single surface, considering normal and friction forces, the weight of the robot and an external force.

As seen in Figure 4.3, N is the normal force on the surface, f_k is the friction force at the contact point with the ground and F_{ext} is an external force. Measuring from the COM location, x_2 and x_1 are the distances to the contact points of the head and the wave with the ground, respectively, and L_{wave} is the total length of the wave. The parameter d is the distance from the COM to the start of the wave, the first point of the wave that will touch the ground during the motion.

In order for the robot to advance, the forces must satisfy:

$$f_{k1} > f_{k2} + F_{ext}. \quad (19)$$

Therefore, if the friction force at contact point 1 is smaller than the external force and the friction force at point 2, the wave touching the surface will slide and the tip of the head will stick to the surface and prevent the motion.

Assuming quasi-static motion, the sum of moments relative to contact point 1 yields:

$$\Sigma M_1 = N_2(x_1 + x_2) - mg \cdot x_1 = 0, \quad (20)$$

Assuming that the external force is acting in the contact point of the head with the ground. This transforms into:

$$N_2 = mg \frac{x_1}{(x_1 + x_2)}. \quad (21)$$

Similarly, sum of moments in contact point 2 yields:

$$N_1 = mg \frac{x_2}{(x_1 + x_2)}. \quad (22)$$

Using (21) and (22), (19) becomes:

$$\mu_{wave} \cdot mg \frac{x_2}{(x_1 + x_2)} > \mu_{head} \cdot mg \frac{x_1}{(x_1 + x_2)} + F_{ext}. \quad (23)$$

If there is no external force acting on the robot, the advancing condition simplifies to:

$$x_2 \cdot \frac{\mu_{wave}}{\mu_{head}} > x_1. \quad (24)$$

As mentioned, x_2 is constant, but x_1 is not, so the value of x_1 needs to be established as a function of time. For that, we consider the representation of the wave of the robot as an advancing sine wave (3). The lowest point in the wave; i.e., the contact point with the ground, will satisfy $y = -A$, therefore:

$$A \sin(kx - \omega t) = -A. \quad (25)$$

Extracting x as a function of time will generate:

$$kx - \omega t = \frac{3\pi}{2} + 2\pi n \rightarrow x(t) = \frac{(1.5 + 2n)\pi + \omega t}{k}, \quad (26)$$

while n is the number of waves. As mentioned, the start of the sine wave is shifted from the COM location by the distance d (see Figure 4.3), therefore the length x_1 is:

$$x_1(t) = \frac{(1.5 + 2n)\pi + \omega t}{k} + d, \quad (27)$$

The motion of the robot is simulated in the next subsection (experiments are also presented in section 6).

4.4 Crawling Between Curved Surfaces

Considering that the robot can be also crawling in a non-straight environment, we want to examine the robot's behavior while crawling between curved surfaces and the effect of the robot and surfaces geometry on the motion. This chapter presents an analysis and modeling of the robot's motion between two curved surfaces, considering different geometries of the surfaces and the robot, as well as exploring different cases of orientation of the robot between the curved surfaces. We simplify the robot's geometry to be a rectangle to simplify the analysis, while the actual outline of the robot is narrower in the head area, facilitating the motion.

4.4.1 Locomotion Definition

We analyze the robot's locomotion between two surfaces, considering a case of curved surfaces with radius of curvature R and distance D between the surfaces. The robot's length is l , and its width is w (also the width of the links), as seen in Figure 4.4.

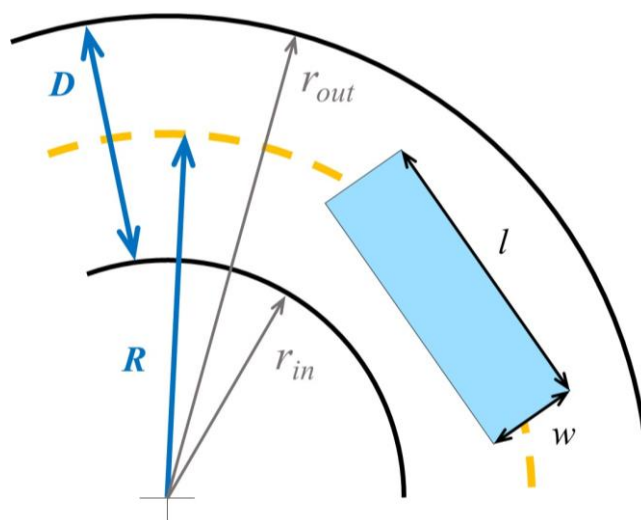


Figure 4.4: Curved surfaces with radius R , distance D between the surfaces, inner radius r_{in} and outer radius r_{out} , with the robot with length l and width w

Figure 4.4 shows a top view of the robot, i.e. the robot is crawling on the floor between the curved surfaces. The values of the outer surface radius and inner surface radius, r_{out} and r_{in} , can be formulated as:

$$r_{out,in} = R \pm 0.5D. \quad (28)$$

When placed between curved surfaces, three different cases of orientation should be considered (see Figure 4.5); In case A, the robot is short relatively to the distance between the surfaces (Figure 4.5A), and can move freely and change its position between them.

When moving between the surfaces it can touch only one surface due to its small length. In case B, the robot's length is larger than the distance between the surfaces and it can touch them with two contact points (Figure 4.5B) in two possible geometries – corners contact (B_I) and tangent contact (B_{II}). In case C, the robot's length and the curvature of the surfaces generate a state in which there are three contact points of the robot with the walls (Figure 4.5C) and no free motion of the robot between the surfaces.

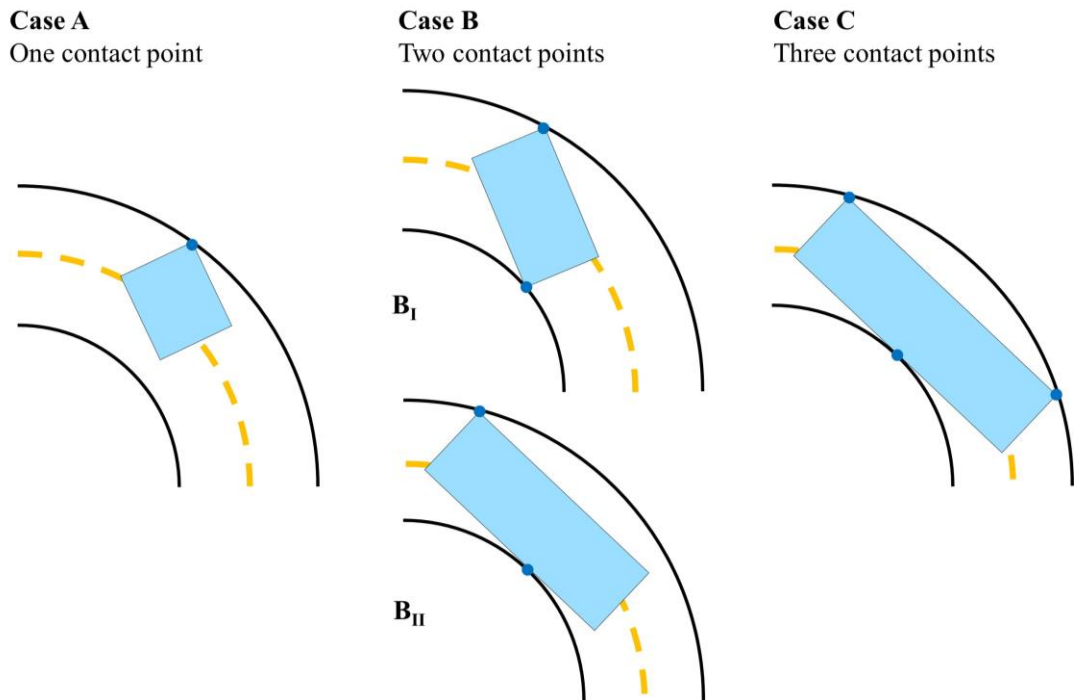


Figure 4.5: Four cases of the orientation of the robot while placed between the two curved surfaces

Next, we will discuss the threshold conditions that define the domain of each case. We will later analyze the locomotion in the different cases.

4.4.2 Geometrical Validity Conditions for the Cases

This section will review the geometrical transition conditions between the different cases, to determine the case of orientation based on given robot and surfaces parameters (i.e. when given the surfaces parameters, we can determine the case of orientation by adjusting the length of the robot). Since the robot's width is constant for every design because of the links' width, we can alter the length by adding or removing links and making the helix longer, without changing the robot or wave parameters.

Therefore, we determine the length of the robot that is limiting the different cases of orientation and determining their validity conditions.

- Case A/B_I Limits

As mentioned before, case A will be valid while the length of the robot is relatively small and can move freely between the curved surfaces. The transition to case B_I will occur when the corners of the robot will touch the curved surfaces, i.e. while the diagonal of the robot (b in Figure 4.6) will be equal to the distance between the surfaces.

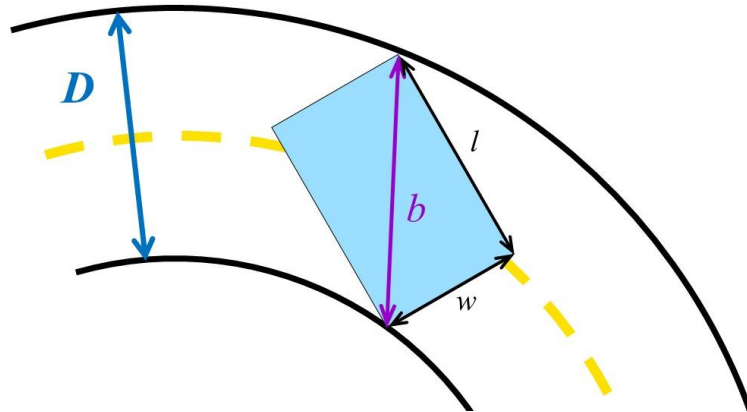


Figure 4.6: The condition for validation of case B

Specifically, the threshold length between cases A and B_I will be:

$$l_{A/B_I} = \sqrt{D^2 - w^2} . \quad (29)$$

Figure 4.7 presents the threshold length for cases A/B_I, for different geometries of the surfaces – the radius R and the distance D (as shown in Figure 4.4):

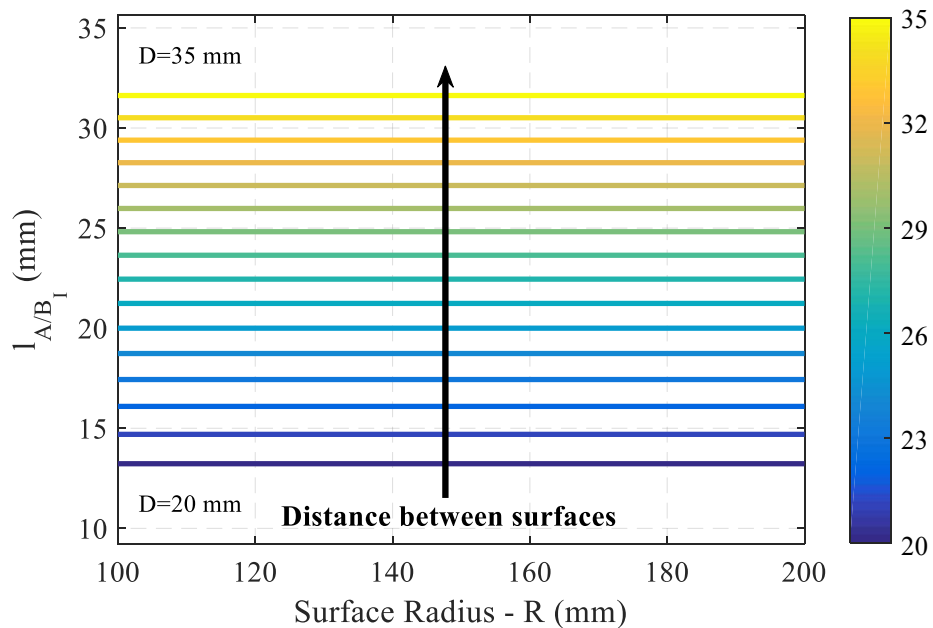


Figure 4.7: Threshold length of the robot between cases A and B_I

- Case B_I/B_{II} Limits

Next, the upper limit for case B_I and lower limit of case B_{II} will be reached when the length of the robot will be long enough to generate a tangent contact point with the inner surface, i.e. the length of the robot will be equal or larger than the length a as shown in Figure 4.8:

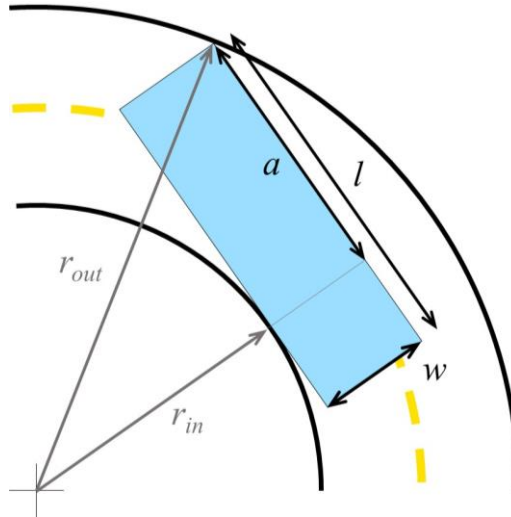


Figure 4.8: The geometry of the robot with a tangent contact point with the inner surface

Therefore, for $l \geq a$ case B_{II} will occur, and the threshold condition between cases B_I and B_{II} is

$$l_{B_I/B_{II}} = a = \sqrt{r_{out}^2 - (r_{in} + w)^2} = \sqrt{2RD + w(D - 2R) - w^2}, \quad (30)$$

using (28) and the Pythagorean theorem. Figure 4.9 shows this threshold condition.

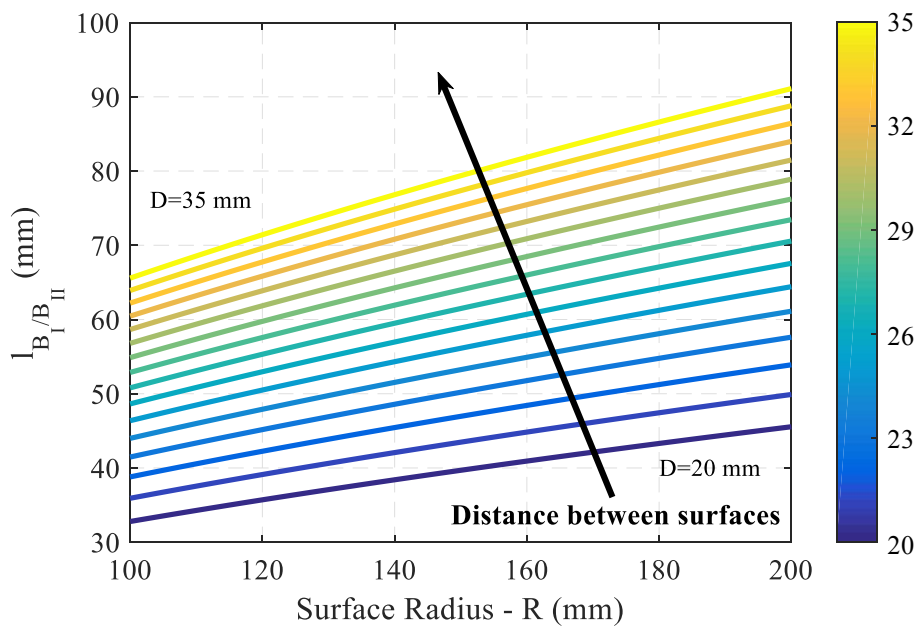


Figure 4.9: Threshold length of the robot between cases B_I and B_{II}

- Case B_{II}/C Limits

With minimum length of (30) and a contact point with the inner surface, if the robot is long enough to reach a second point on the outer surface, it will transfer to case C, as seen in Figure 4.10.

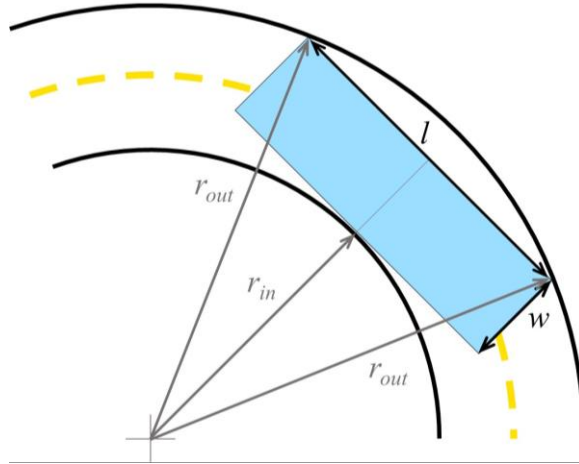


Figure 4.10: The geometry of the robot in case C between the surfaces

The length of the robot when transitioning to case C can be calculated from this position of the robot:

$$(0.5l)^2 + (r_{in} + w)^2 = r_{out}^2. \quad (31)$$

Extracting l from the equation:

$$l_{B_{II}/C} = 2\sqrt{2RD + w(D - 2R) - w^2}, \quad (32)$$

which is exactly (30) times two, as can be deduced by considering the similarity to case B_{II}, and considering the length of the robot in case C to be equal to $2a$.

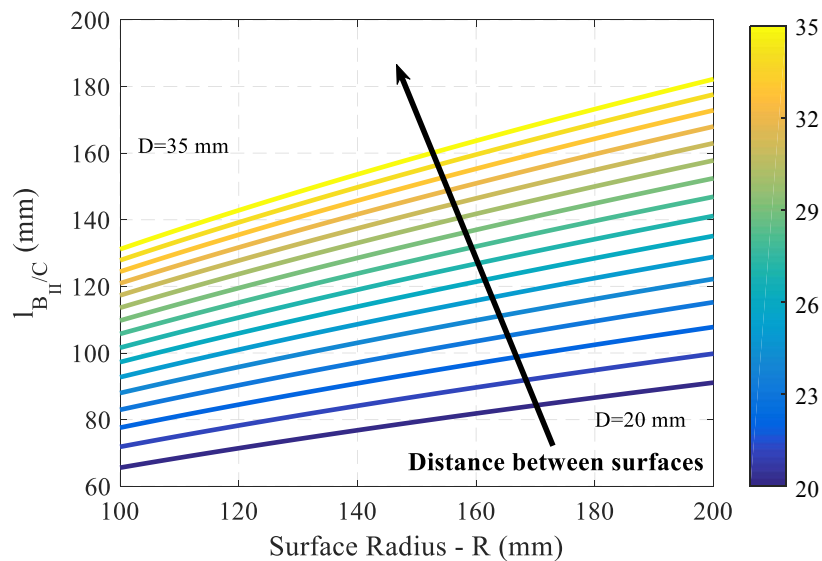


Figure 4.11: Threshold length of the robot between cases B_{II} and C

- Summary of cases of orientation validity conditions

Figure 4.12 concludes the threshold length conditions between all of the cases of orientation, as a function of the width of the robot and the surfaces parameters.

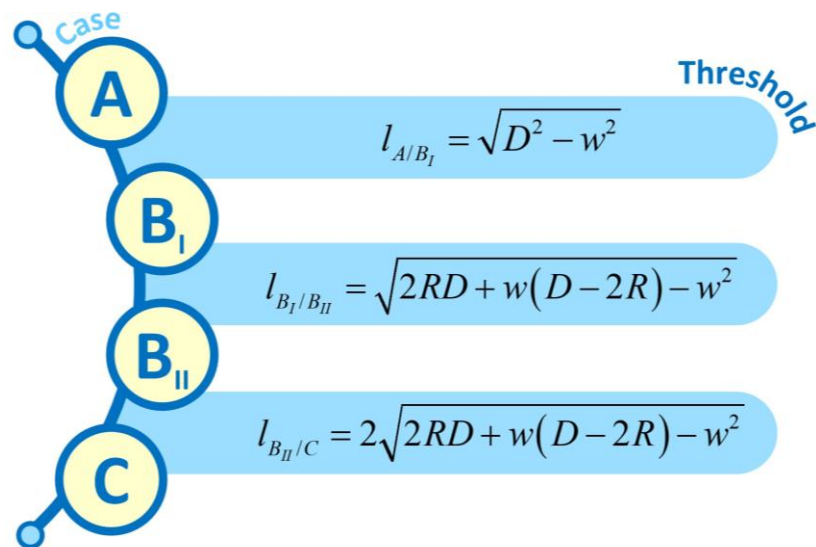


Figure 4.12: Diagram of length threshold conditions between the cases of orientation

Next, we will present the motion analysis of the robot in each case of orientation. The analysis is simplified and a few elements are neglected: the weight of the robot, the thrust force location, the center of mass location. Therefore, the analysis will not provide exact result, but allow us to understand the motion and roughly examine the different locomotion cases.

4.4.3 Case A of Orientation

The robot, when driven by a thrust force F_{th} and crawling forward between the curved surfaces (Figure 4.13a), will crawl freely until contacting the outer surface wall in a single corner (Figure 4.13b).

Next, there are two options for motion: One, the touching corner of the robot with the outer surface will slide on the surface and the robot will keep advancing forward while touching the wall, and slowly rotate outwards to the outer wall (see Figure 4.13c).

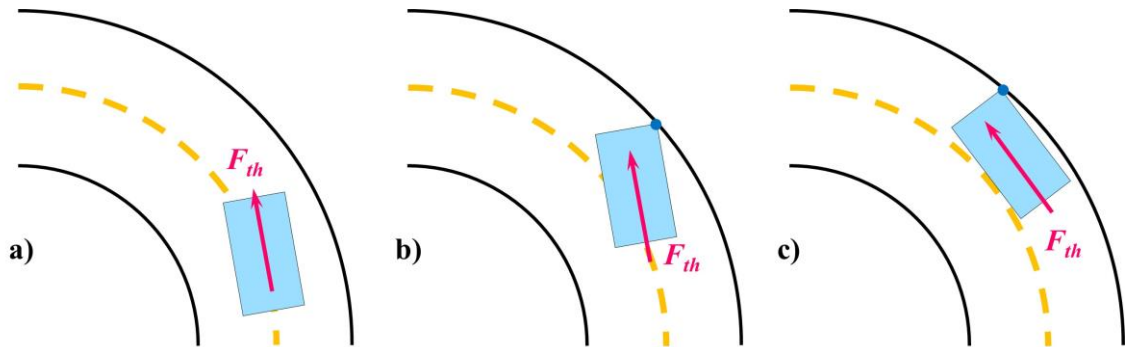


Figure 4.13: Case A of crawling between curved surfaces, contacting the outer wall, rotating outward and advancing

Two, the robot will push towards the outer wall, the contact point will remain stationary and the robot will rotate inwards around the point and face the outer wall, and therefore will get stuck (Figure 4.14).

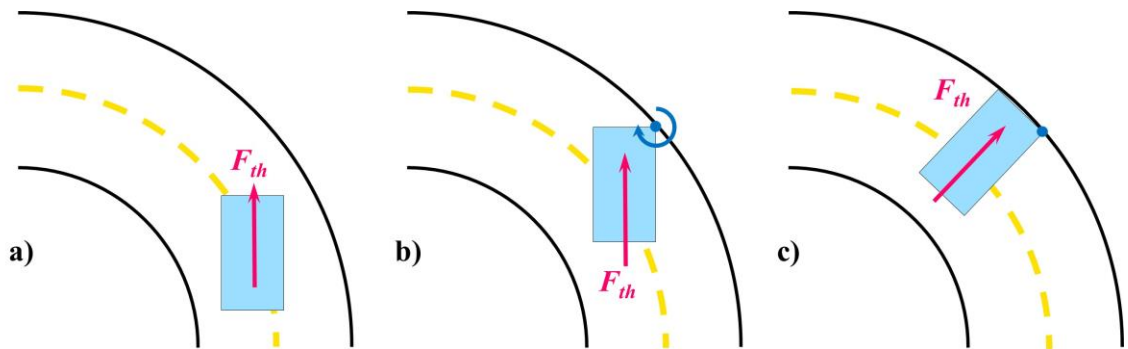


Figure 4.14: Case A of crawling between curved surfaces, contacting the outer wall, rotating inward and stopping

In this analysis, the motion option the robot will take depends on the angle ρ in which the robot approaches the outer wall, as shown in Figure 4.15. Considering the forces acting on the robot in the x direction, i.e. tangent to the outer surface in the contact point, the point in which the robot contacts the wall will slide on the wall and allow the robot to advance when:

$$\Sigma F_x > 0 \rightarrow F_{th} \cos \rho - f_k > 0. \quad (33)$$

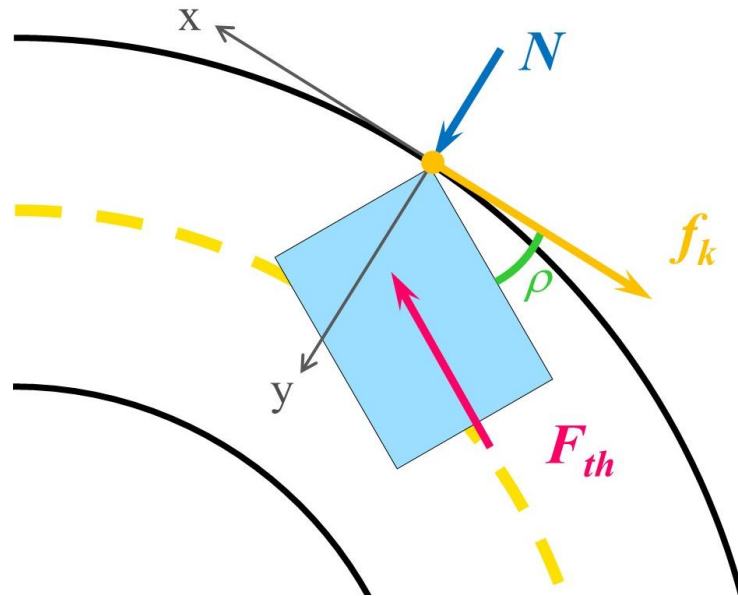


Figure 4.15: Case A, the robot touching the outer surface

In the y direction, the forces generate:

$$N - F_{th} \sin \rho = 0. \quad (34)$$

Using the Coulomb friction model to simplify the analysis,

$$f_k = \mu N, \quad (35)$$

when substituting (34), (33) becomes:

$$F_{th} \cos \rho - \mu F_{th} \sin \rho > 0. \quad (36)$$

This reduces to the angle condition:

$$\rho < \arctan(\mu^{-1}). \quad (37)$$

When the angle ρ satisfies the condition above, the robot will advance with outward rotation (Figure 4.13), and when the angle is larger, the robot will rotate inwards (Figure 4.14).

However, this model is very simplified and does not describe the motion very accurately, since it doesn't consider the advancing mechanism of the robot, the location from which the wave is pushing the robot (i.e. front-wheel drive vs. rear-wheel drive) and the curve of the surfaces. The model could fit a condition in which the robot's width is very small and close to zero, but the correct angle for a realistic condition can be calculated precisely by using a numeric simulation, as will be presented later.

4.4.4 Case B_I of Orientation

Like in the previous case, when the robot is crawling between curved surfaces driven by a thrust force, it will contact the outer surface and rotate. The rotation options presented for case A are valid also for this case. When rotating outward, the robot will stick to the outer radius and the contact point will slide on the surface. However, when rotating inwards in this case, the rotation will cause the robot to stick to the inner surface and generate two contact points with the corners of the robot (see Figure 4.16). In this case, even if the robot follows the inward rotation and touches the inner surface, it will still be able to advance under certain conditions.

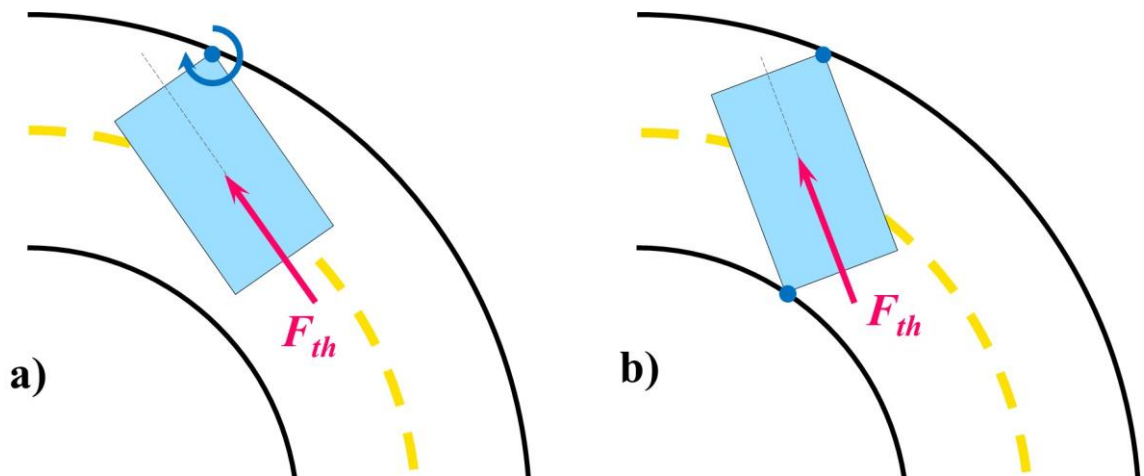


Figure 4.16: The robot crawling between curved surfaces in Case B_I, (a) crawling freely between the surfaces and contacting the surface in a single corner, (b) rotating inwards around the corner and generating two contact points in the corners of the robot

Since the corners of the robot touch the inner and outer surfaces, the angle φ is one of the angles in the triangle formed by the curve radii and the robot's diagonal (see Figure 4.17). Therefore, φ can be calculated using the law of cosines, considering the robot and the curve parameters:

$$b^2 = r_{out}^2 + r_{in}^2 - 2r_{out}r_{in} \cos \varphi, \quad (38)$$

and explicitly:

$$\varphi = \arccos \left[\frac{2R^2 + 0.5D^2 - b^2}{2R^2 - 0.5D^2} \right]. \quad (39)$$

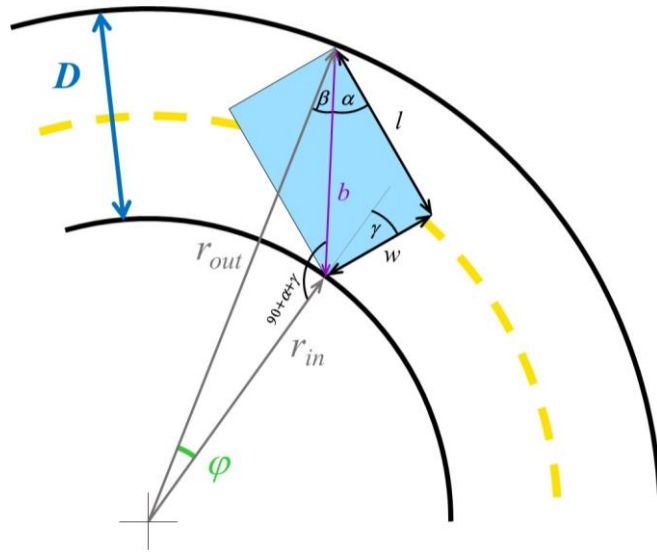


Figure 4.17: The robot between the surfaces in Case B₁ after inward rotation, with touching corners. The radii of the surfaces and the robot's diagonal create a triangle

In addition to the angle α defined by the robot's geometry (formed between the robot's outline and the diagonal, see Figure 4.18), the contact of the robot with the surfaces will generate two more angles: β and γ . The angle α can be calculated by:

$$\alpha = \arctan \left(\frac{w}{l} \right). \quad (40)$$

The angle β is the angle between the outer radius and the diagonal, and can be calculated with the law of sines:

$$\frac{b}{\sin \varphi} = \frac{r_{in}}{\sin \beta}, \quad (41)$$

and explicitly from (41), using (28):

$$\beta = \arcsin \left(\frac{(R - 0.5D) \sin \varphi}{b} \right). \quad (42)$$

Similarly, the angle γ will be formulated as:

$$\gamma = \arcsin\left(\frac{(R+0.5D)\sin\varphi}{b}\right) - \alpha - 90. \quad (43)$$

While crawling between the surfaces, the robot will push and drive forward and generate a normal force N_i and a friction force f_{ki} in contact point i . The distance of the contact points with the outer and inner surfaces from the center of the radii are r_{out} and r_{in} vectors, respectively (see Figure 4.18).

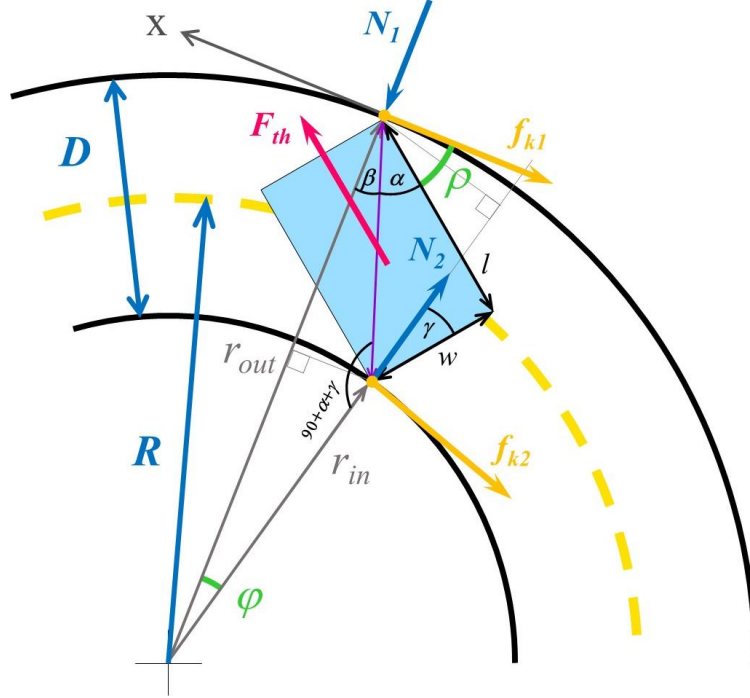


Figure 4.18: The robot crawling between the surfaces in Case B_I, with the corners of the robot contacting the tube walls

Assuming quasi-static locomotion, i.e. zero acceleration, to find the normal forces and the thrust force propelling the robot, we determine the sum of moments, in point 1:

$$\Sigma M_{(1)} = N_2 \cdot r_{out} \sin\varphi - f_{k2}(r_{out} \cos\varphi - r_{in}) - F_{th} \cdot 0.5w = 0, \quad (44)$$

when φ is the angle between the vectors of r_{out} and r_{in} . In point 2:

$$\Sigma M_{(2)} = N_1 \cdot r_{in} \sin\varphi - f_{k1}(r_{out} - r_{in} \cos\varphi) + F_{th} \cdot 0.5w. \quad (45)$$

From these equations, we can extract the normal forces, N_1 and N_2 . For N_1 , when (45) equals zero in quasi-static motion, the equation simplifies to:

$$\mu N_1(r_{out} - r_{in} \cos\varphi) - N_1 r_{in} \sin\varphi = 0.5w F_{th}. \quad (46)$$

When isolating N_I we get:

$$N_I = \frac{0.5wF_{th}}{\mu(r_{out} - r_{in} \cos \varphi) - r_{in} \sin \varphi}, \quad (47)$$

which can be reformulated as:

$$N_I = \frac{0.5wF_{th}}{\mu \left[r_{out} - \left(\frac{r_{out}^2 + r_{in}^2 - b^2}{2r_{out}} \right) \right] - r_{in} \sqrt{1 - \left(\frac{r_{out}^2 + r_{in}^2 - b^2}{2r_{out}r_{in}} \right)^2}}. \quad (48)$$

This allows us to determine the critical point from which the motion will occur, by looking at the denominator of N_I , when equals zero:

$$\mu(r_{out} - r_{in} \cos \varphi) - r_{in} \sin \varphi = 0. \quad (49)$$

With (49) we can find the critical value of μ that will enable the motion:

$$\mu_{crit} = \frac{r_{in} \sin \varphi}{r_{out} - r_{in} \cos \varphi}. \quad (50)$$

A lower value will make N_I negative and therefore allow the robot to slide on the surface and rotate outward, and a higher value will cause the robot to rotate inwards and stick to the inner surface. However, the robot will still be able to advance while in this position. The critical μ values are shown in Figure 4.19. The results were calculated for a specific geometry of the robot (length l and width w) with various values of radii R and distances D .

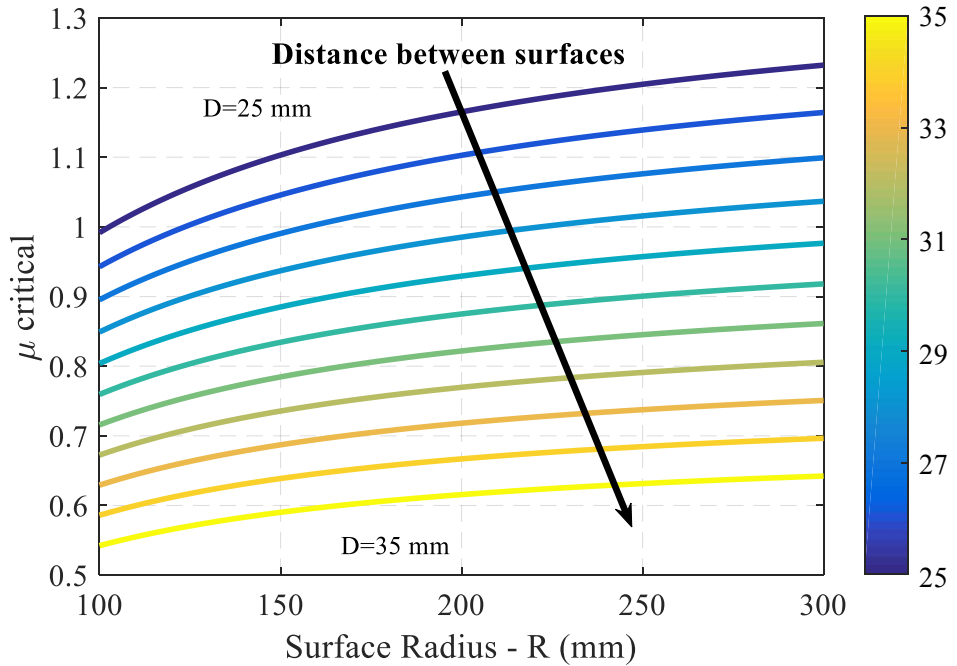


Figure 4.19: Critical μ values for case B_I

4.4.5 Case B_{II} of Orientation

The locomotion mechanism in this case is similar to case B_I. The only difference is in the geometry created when the robot is rotating inwards and sticks to the inner surface, as shown in Figure 4.20.

Unlike Case B_I, the angle formed between the r_{out} , r_{in} vectors is part of a right triangle (see θ in Figure 4.20), and can be formulated as:

$$\cos \theta = \frac{r_{in} + w}{r_{out}}. \quad (51)$$

By isolating θ and using (28):

$$\theta = \arccos\left(\frac{r_{in} + w}{r_{out}}\right) = \arccos\left(\frac{R - 0.5D + w}{R + 0.5D}\right). \quad (52)$$

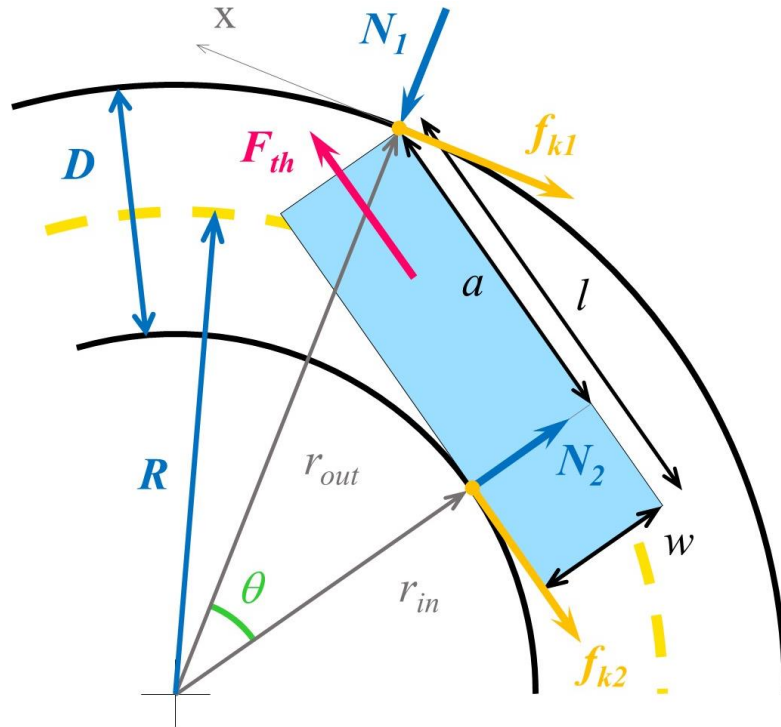


Figure 4.20: The robot crawling between the surfaces with two contact points with the outer and inner surfaces (case B_{II})

Like in the previous case, to find the dependence of the normal forces and the thrust force propelling the robot, we determine the sum of moments, in point 1:

$$\Sigma M_{(1)} = f_{k2} \cdot w + N_2 \cdot a - F_{th} \cdot 0.5w, \quad (53)$$

and in point 2:

$$\Sigma M_{(2)} = -f_{k1} (r_{out} - r_{in} \cos \theta) + F_{th} \cdot 0.5w + N_1 r_{in} \sin \theta. \quad (54)$$

From these equations, we can extract the normal forces, N_1 and N_2 . For N_1 , when (54) equals zero in quasi-static motion, the equation simplifies to:

$$N_1 r_{in} \sin \theta + \mu N_1 (r_{in} \cos \theta - r_{out}) = F_{th} \cdot 0.5w. \quad (55)$$

When isolating N_1 we get:

$$N_1 = \frac{0.5wF_{th}}{\mu(r_{out} - r_{in} \cos \theta) - r_{in} \sin \theta}, \quad (56)$$

which can be formulated as:

$$N_1 = \frac{0.5wF_{th}}{\mu \left[r_{out} - r_{in} \left(\frac{r_{in} + w}{r_{out}} \right) \right] - r_{in} \sqrt{1 - \left(\frac{r_{in} + w}{r_{out}} \right)^2}}. \quad (57)$$

Again, for the critical values of the friction coefficient, with (50) for θ we obtain the critical values as shown in Figure 4.21, for various values of radii R and distances D (with constant l and w of the robot).

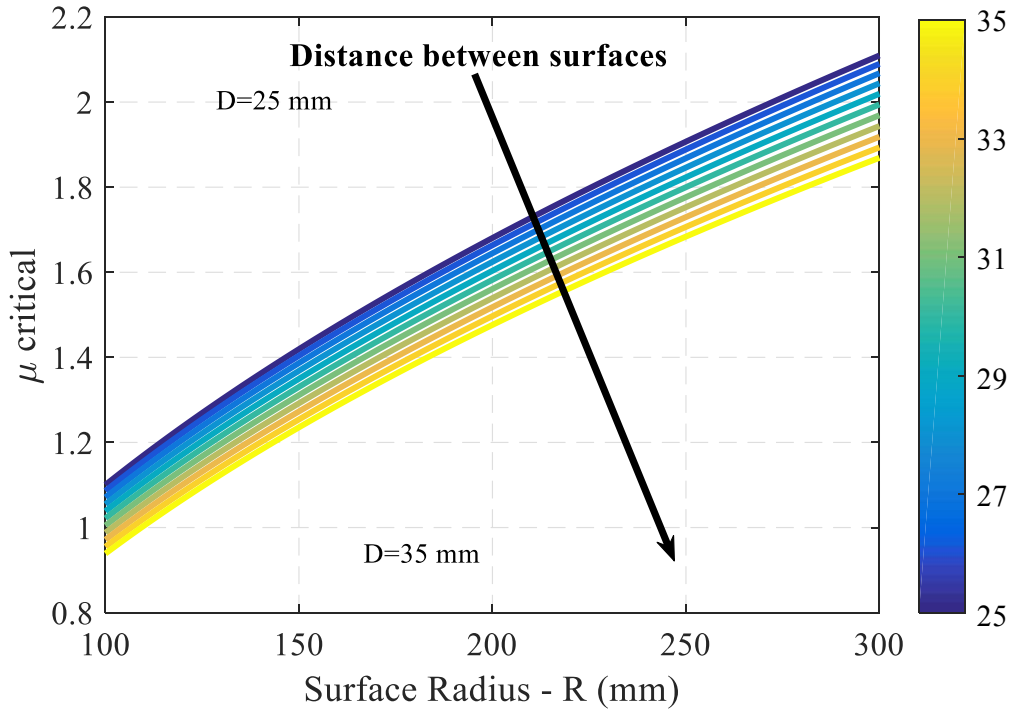


Figure 4.21: Critical μ values for case B_{II}

From (59) using (35), we can extract the normal force N_1 :

$$N_1 = \frac{N_2 (r_{out} \sin \theta - \mu w) + 0.5wF_{th}}{r_{out} [\sin 2\theta - \mu(1 - \cos 2\theta)]}, \quad (60)$$

and similarly, for N_3 :

$$N_3 = \frac{N_2 (r_{out} \sin \theta + \mu w) - 0.5wF_{th}}{r_{out} [\sin 2\theta + \mu(1 - \cos 2\theta)]}. \quad (61)$$

In this case, for a certain l and w , there will be only very specific cases of the surface parameters that will generate this case of orientation. For example, for width w of 15 mm and length l of 80 mm, case C will occur for radius R of 125 mm and D of 21 mm. The critical value for μ , derived from the denominator of (60) similar to (50), is calculated with:

$$\mu_{crit} = \frac{\sin 2\theta}{1 - \cos 2\theta}, \quad (62)$$

and equals 3.25 in this specific case.

5 Motion Simulations

This section presents a couple of motion simulations that were created using the MATLAB[®] software, to evaluate the equations and modeling that were previously developed and to allow us to test various cases of motion.

5.1 Crawling On a Single Surface

To evaluate the robot's motion on a single surface and examine the advancing/sliding motion, we developed a numerical simulation. The simulation is based on the analysis presented in section 4.3 and the stick-slip condition (24) (code attached in appendix [F]).

The simulation shows the motion of the robot as a function of the angular velocity of the wave, the COM location, the robot's size and the wave parameters. The simulation plots the sine wave of the robot and moves the robot forward or backwards, depending on the angular velocity value. The wave is plotted according to the sine wave equation (3). Figure 5.1 shows the pseudocode of the simulation.

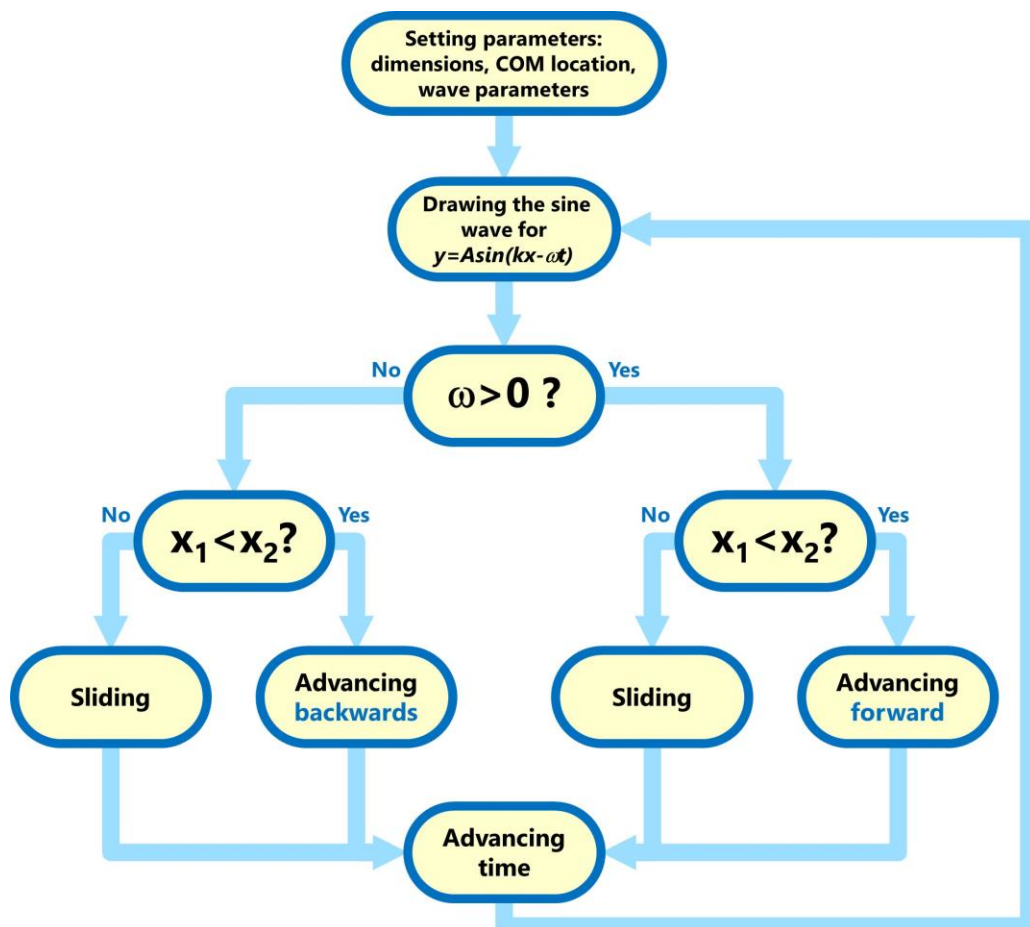


Figure 5.1: Pseudocode of the motion simulation on a single surface. x_2 is constant and equals the distance between the COM and the contact point of the head with the ground. x_1 is the distance between the COM and the contact point of the wave with the ground, which is varying with time.

As shown in Figure 5.1, we first enter the required values of different parameters. Then, after the simulation considers the sign and value of the angular velocity ω , it determines the existence of the advancing condition and moves (or does not move) the robot in the simulation accordingly. The robot will advance forward or backwards according to the velocity of the link (7), which will be the velocity of the robot while there is no sliding. The list of parameters used in the simulation and their value are shown in Table 5.1.

Table 5.1: Parameters considered in the single surface simulation

Parameter	Meaning
f	Frequency of the helix's rotation = $1/T$
k	Wave number = $2\pi/L$
L	Length of the wave (pitch of the helix)
$number_of_waves$	Number of sine waves comprising the wave of the robot
r	Height of a link
T	Period of the sine wave
x_2	Distance between the COM and the contact point of the head with the ground
$\mu_{w/h}$	Ratio between the friction coefficients of the wave and the head with the ground
ω	Angular velocity = $2\pi f$

Selected screenshots from the simulation are shown in Figure 5.2 (also see video). It shows the robot partly advancing and partly sliding, for one cycle of the motion, i.e. for one period of the sine wave. In this simulation, the angular velocity is negative and therefore the robot is moving forward. It can be easily reversed by changing the input value of ω . As mentioned, the contact point (marked by the small triangle) of the wave with the ground vary as a function of the sine wave, i.e. the lowest point of the wave, as calculated in (27). The robot advances in the simulation only when condition (24) is met.

Motion Direction

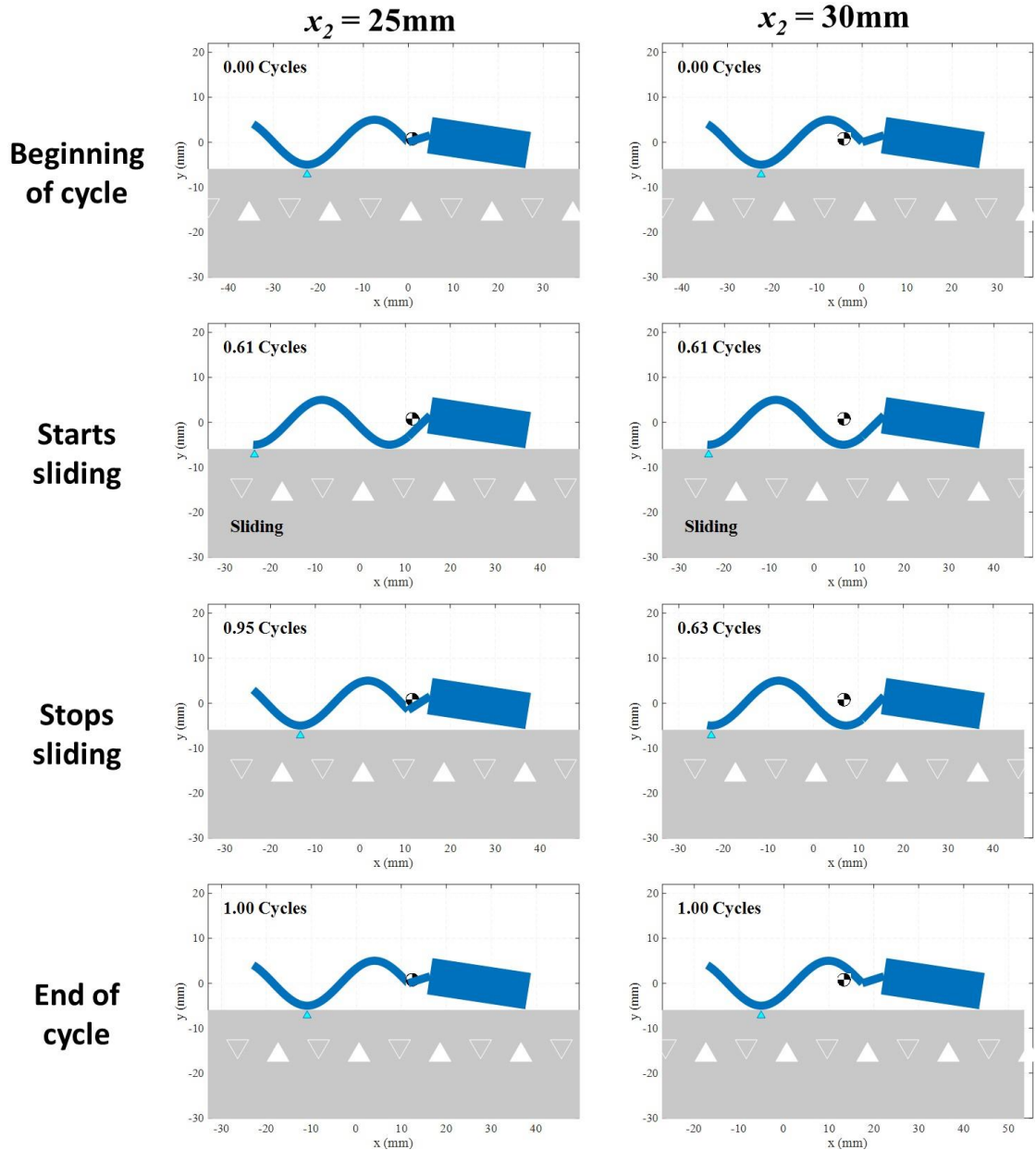


Figure 5.2: Simulation of the robot's movement on a rigid surface (also see video). Left – COM location closer to the head (sliding time of 0.34 cycle, right – COM location closer to the wave. The sliding time

These screenshots show two cases of two different location of the COM, i.e. different values of x_2 : 25 mm and 30 mm. As seen in the figure, the slipping duration when the COM is closer to the wave (right) is shorter than when it is closer to the wave (left), 34% and 2% of the cycle, respectively. This occurs because of (24): when x_l is larger for a longer period of time, the robot will advance more.

Using the simulation, we calculated an Advance Time Ratio (ATR), which is defined as the time during which the robot advances divided by the total time of motion (in which the robot is either advancing or sliding without advancing):

$$ATR = \frac{\text{Advancing time}}{\text{Total time of motion}} \% . \quad (63)$$

Since the value of x_1 (27) is a function of the distance d between the COM and the start of the wave (see Figure 4.3), a change in the value of d will also affect the ATR (which depends on the stick-slip condition (24)). Therefore, The ATR was calculated for different values of d , as well as for different ratios of the COF of the head divided by the COF of the wave- $\mu_{\text{head}}/\mu_{\text{wave}}$. Figure 5.3 shows the results of the ATR calculations.

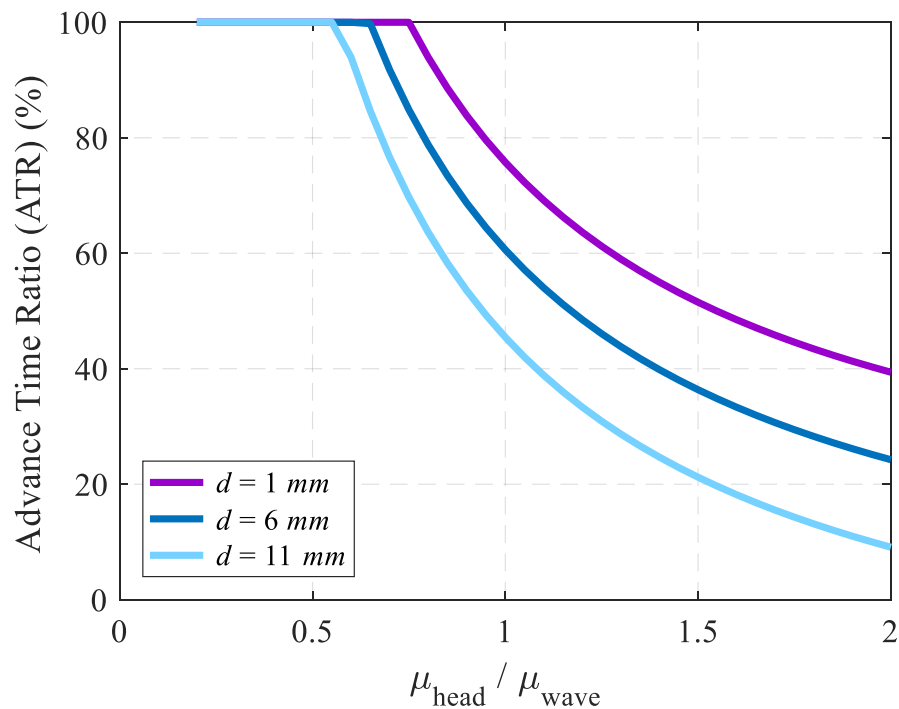


Figure 5.3: The advance time ratio (ATR) of the robot in the simulation with different ratios of the head and wave COFs.

As shown in the results, the simulation considers three different values of d : the current value in our design ($d=6$ mm), 5 mm smaller ($d=1$ mm), and 5 mm larger ($d=11$ mm). Additionally, it calculates the ATR for COF ratios of 0 to 2 (from zero friction of the head with the surface, to a case where μ_{head} is twice the μ_{wave}).

As predicted, the simulation showed an increase of the ATR when the head's COF with the ground was smaller than the wave's COF with the ground, since a head that creates no friction will not resist the motion. In addition, the ATR increased as the value of d decreased. This is consistent with our predictions, because when d decreases the wave will have more range of contact with the surface and therefore will advance the robot forward for a longer time.

By considering the parameters of our robot and assuming the same COF for the head and the wave, the ATR was 60%, compared to 57% measured in the experiment (see section 6.1.3).

5.2 Crawling Between Two Curved Surfaces

To examine the different cases of orientation and evaluate the robot's motion between curved surfaces, we created a second numerical simulation, partly based on the analyses in section 4.4.

The simulation takes the geometry of the robot and the surfaces and generates calculation of the motion of the robot and the contact with the walls, for every case of locomotion. The simulation considers the robot's geometry, the radii of the surfaces, initial orientation state, COM location, self-thrust velocity and its location on the robot, stiffness and coefficient of restitution of the surfaces, friction coefficient with the surfaces and added thrust force from the back of the robot. Figure 5.4 shows the pseudocode of the simulation.

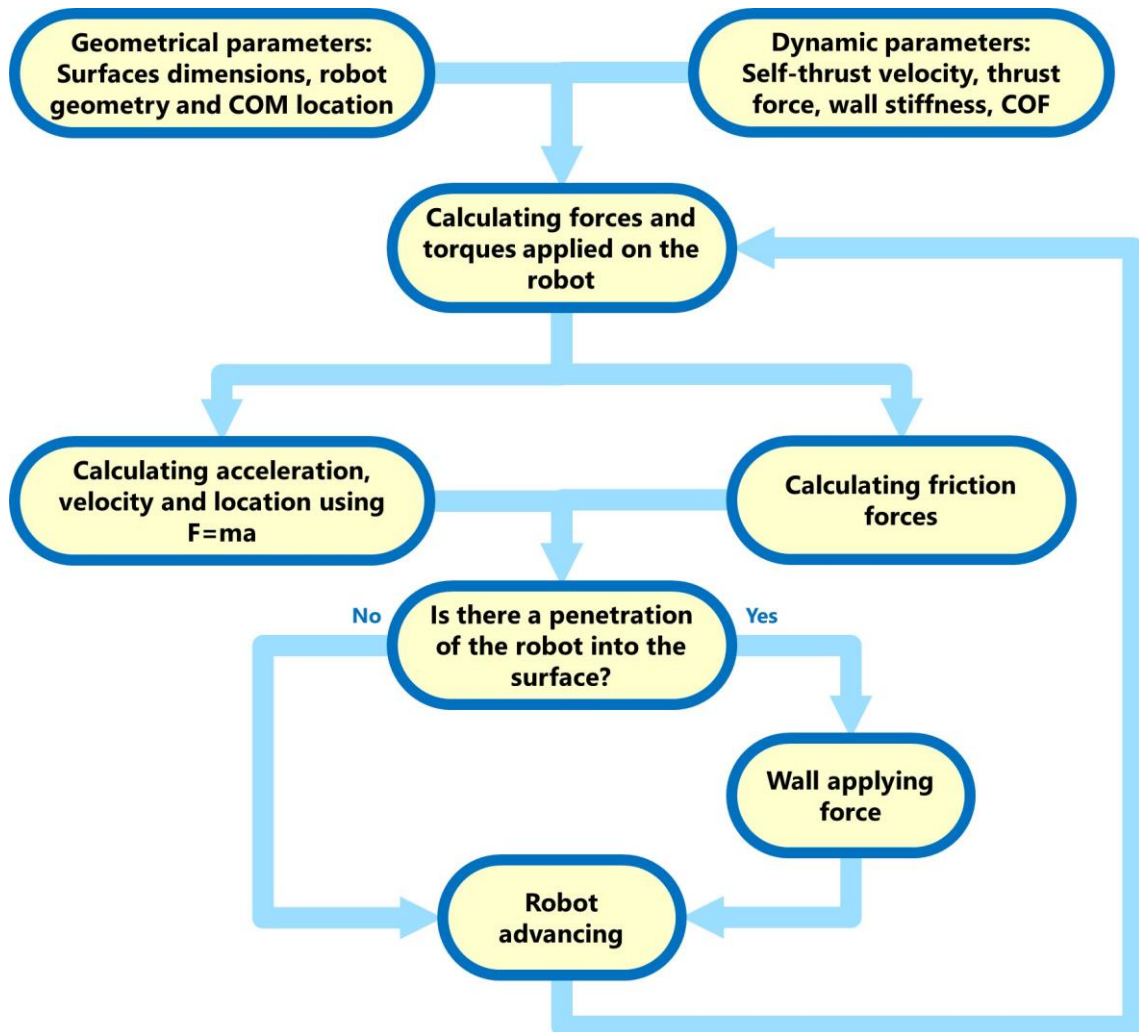


Figure 5.4: Pseudocode of the motion simulation between curved surfaces.

As shown in Figure 5.4, we first define various surface and robot parameters in the simulation. Then, it calculates the forces and torques applied on the four corners of the robot considering the input added thrust force, the friction forces with the ground and the forces from the walls (if contacting). Next, the simulation calculates the acceleration, velocity and location of the COM of the robot and of the four corners, followed by a calculation of penetration of the robot to one of the surfaces and implementation of corresponding forces. A further explanation of the algorithm and the Matlab code are attached in appendix [G].

The list of parameters used in the simulation and their value are shown in

Table 5.2: Parameters considered in the curved surfaces simulation

Parameter	Meaning
R	Surfaces radius
D	Distance between the surfaces
w	Width of the robot
l	Length of the robot
COM	COM location on the robot
$Theta_{V0}$	Initial orientation of the robot
$Cthrust$	Self-thrust point location on the robot
m	Mass of the robot
Vin	Input velocity of the added thrust
$Kwall$	Stiffness of the walls/surfaces
COR	Coefficient of restitution
μ_{in}	COF of the inner surface
μ_{out}	COF of the outer surface
μ_{ground}	COF of the robot with the ground
μ_{thrust}	COF of the self-thrust points with the ground
Fin	Added thrust force

Selected screenshots from the simulation are shown in Figure 5.5 (also see video). As seen in the screenshots, the simulation considers the four different cases individually and sets the geometrical parameters to match each case. For case A the simulation also calculates the impact angle ρ as mentioned in Figure 4.15.

In the current simulation we adjusted the parameters to agree with the analytical model, by reducing the mass of the robot, neutralizing the self-thrust of the robot and enabling motion with the added thrust force from the back. With these parameters we were able to calculate the critical friction coefficients for every case, using the expressions for μ_{crit} obtained from the analysis as presented in chapter 4.4, and reach an accuracy of 0.0001 in the simulation.

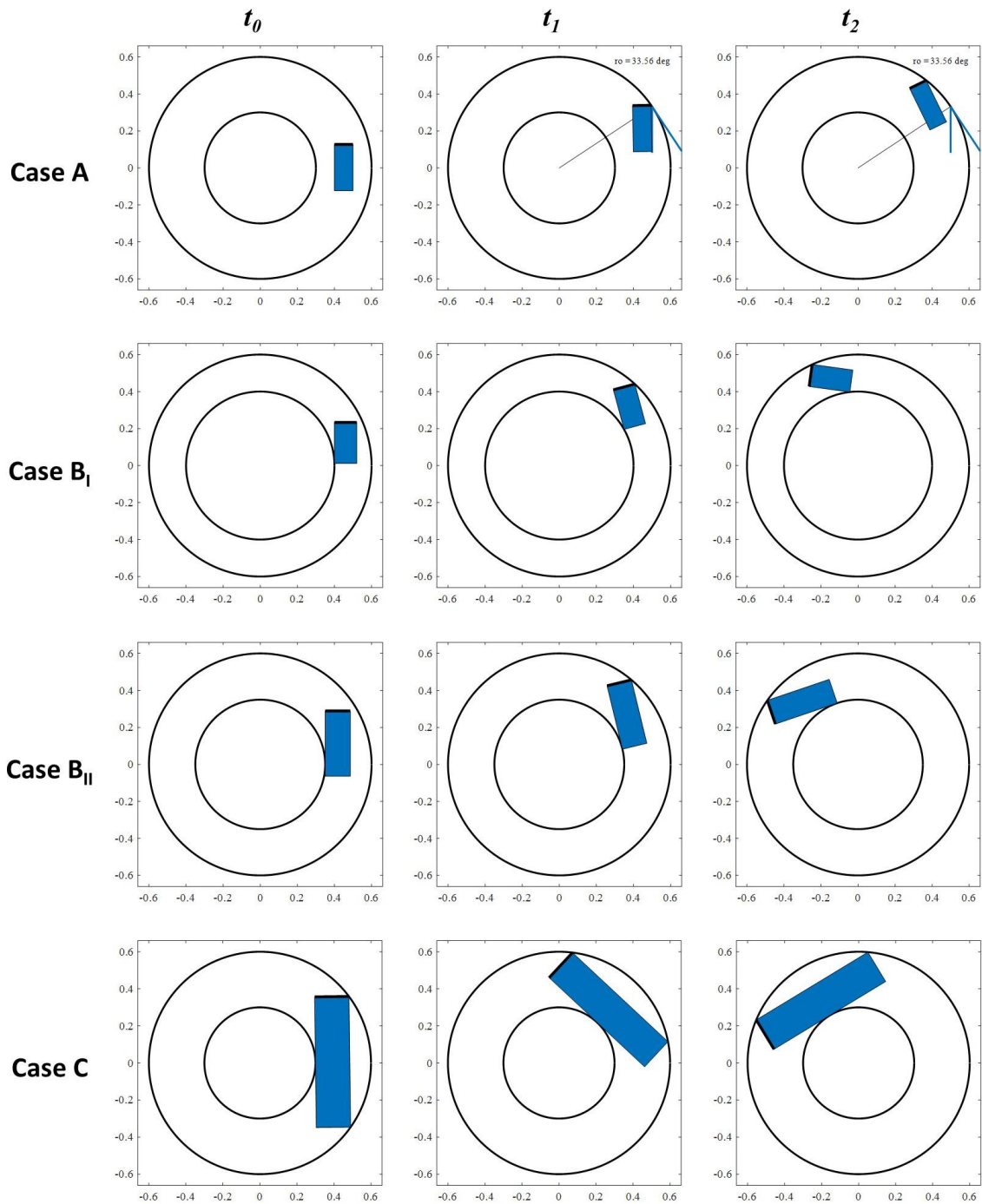


Figure 5.5: Screenshots from the curved surfaces simulation. From top to bottom: case A, case B_I, case B_{II}, case C. Three different frames for each case – time advancing in the frames from left to right.

6 Experiments

This section reviews the multiple experimental systems that were created to test the robot's motion in different environments, as well as the experiments performed with different models of the robot.

6.1 Motion Experiments in 2D

This section presents the experiments performed between two surfaces and on a single surface, as well as the flexible surfaces used for conducting the experiments.

6.1.1 Experiment System: Flexible Surfaces

To test the robot's advancement over flexible surfaces, we used two layers of flexible surfaces created previously in the lab: hollow mesh-like surface, shown in Figure 6.1.

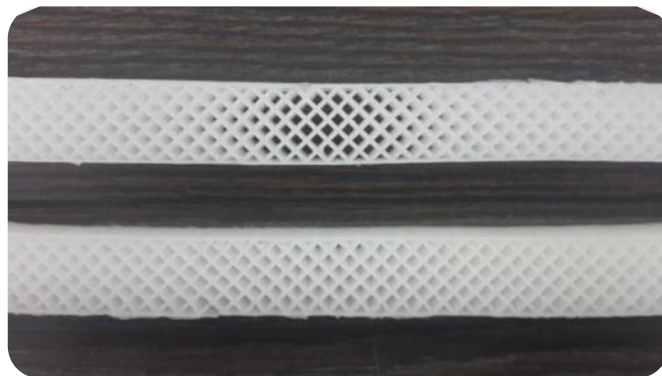


Figure 6.1: Flexible surfaces with a mesh structure

6.1.2 Experiments between Two Compliant Surfaces

The flexible surfaces used in the experiment allow us to apply relatively low pressure on the robot to ensure contact without damaging its parts. They also decrease slipping of the wave on the surface. Figure 6.2 depicts experiments that were performed using the flexible surfaces to test the robot's motion between two surfaces (also shown in the attached video). We tested different models of the robot, applying 4-5 V to the motor via a power supplier. The robot was placed between straight surfaces (Figure 6.2 left) and between curved surfaces (Figure 6.2 right).

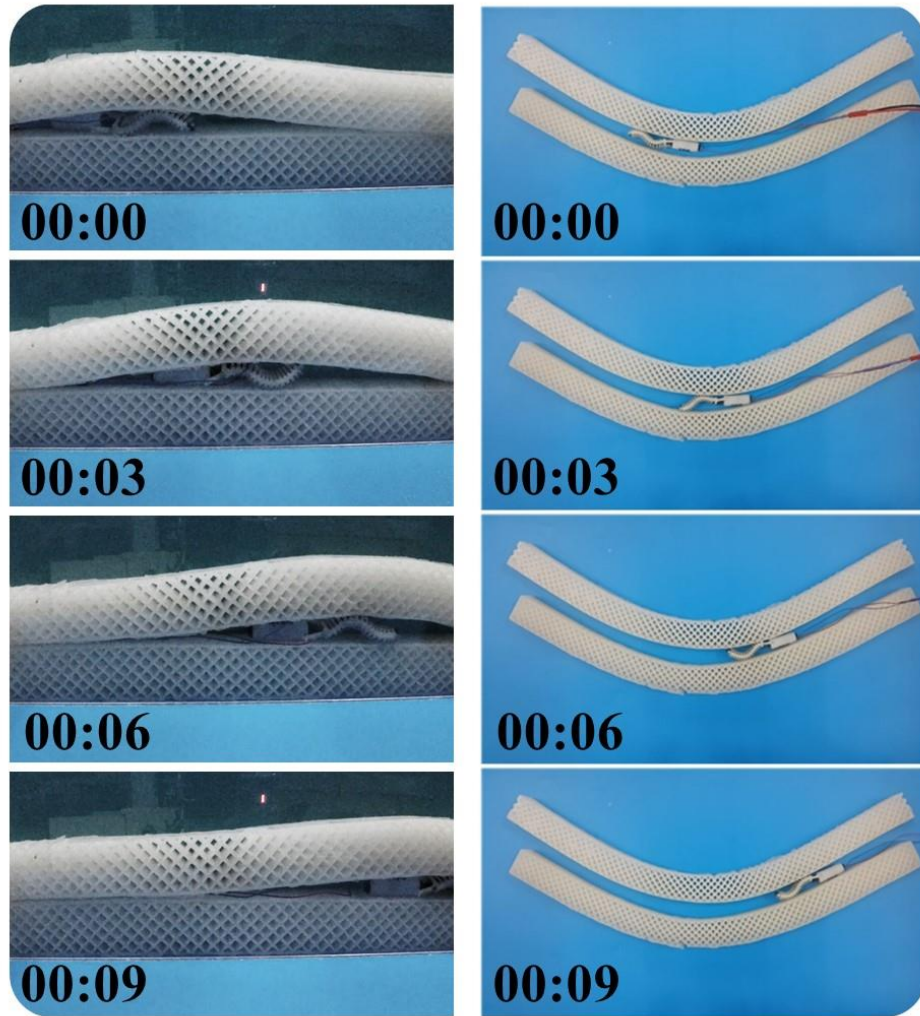


Figure 6.2: The robot moving between two flexible surfaces (left) and curved surfaces (right).

As expected from our analysis (section 4.2), the experiments shows that the locomotion of the robot was continuous. Using frame analysis of the 120-fps video, we calculated the robot's ATR (63) for advancing between two surfaces, by counting the frames where the robot advanced and the total number of frames. Dividing the numbers will provide the ATR value of the motion.

The robot's ATR was found to be 89%. Although our analysis expected a 100% ATR, we believe that the difference between the result and the theory was due to some sliding because the wires may have applied considerable friction and there may have been movement between the links and the helix due to the structure of the links. When crawling between two surfaces, the robot reached a maximum speed of 28.2 mm/sec (AVG = 25.0 mm/s, STD = 3.4 mm/s).

6.1.3 Experiment of Motion on a Single Surface

The robot was run over a flat surface. The stick and slip motion described in section 4.3 is clearly visible (see video). Figure 6.3 shows the robot's movement in the experiment, which consisted of partly sliding and partly advancing as was predicted in the motion simulation. When analyzing the video as explained before, the Advance Time Ratio was 57%. This is consistent with the ATR calculated from the simulation result of 60%, shown in Figure 5.3 (for $d=6$ mm and the same COF for the head and the wave).

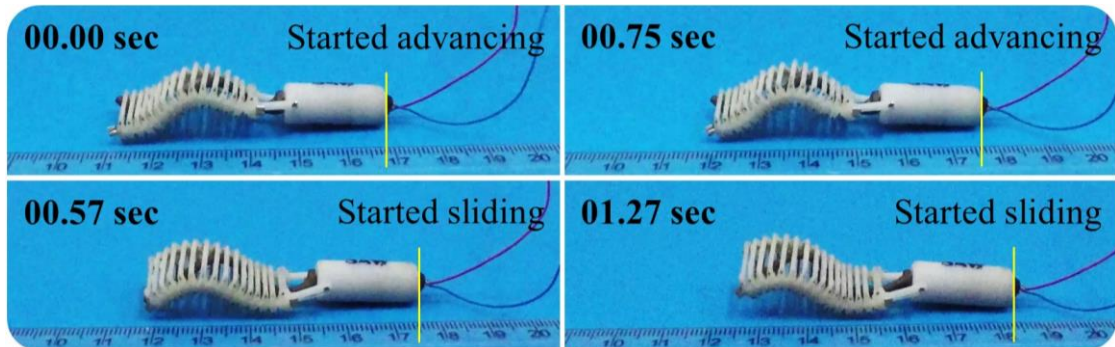


Figure 6.3: The robot moving on a rigid surface. The robot is partly moving and partly sliding, as predicted in the simulation.

6.2 Forces Measuring in Tubes

To evaluate the robot's motion inside tube, we conducted a series of experiments on the robot to determine the conditions in which it can crawl inside a compliant tube. First, we analyzed different cases of the robot's placement in a tube and measured the resulted forces acting on the wave.

6.2.1 Propulsion and Resisting Forces

When the robot is placed inside a tube, we considered three distinct cases of the robot's placement as illustrated in Figure 6.4:

(a) Collapsed tube-like surfaces, where the tube collapses on the robot and creates contact in the top and bottom of the link.

(b) Corner contact points, where the tube maintains its round shape and only the corners of the links touch the tube, and

(c) A tightly inserted robot, where the outer perimeter of the robot is larger than the tube's and the tube is stretched when the robot is placed inside it.

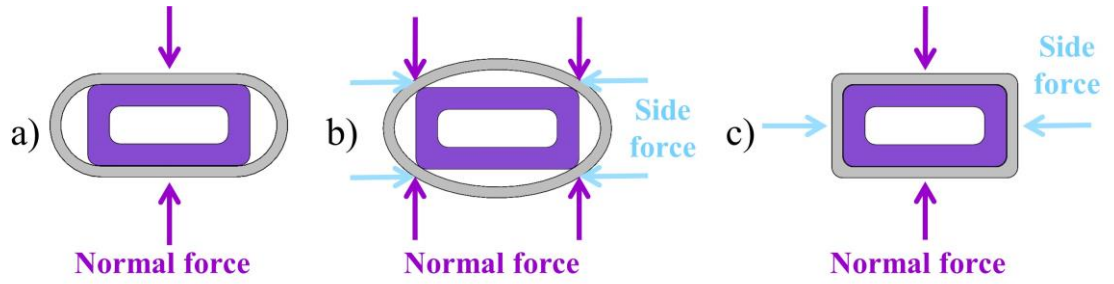


Figure 6.4: Cross-section of the links inside a tube in three different cases of contact between the robot and the tube: (a) collapsed tube-like surfaces, (b) corner contact points and (c) tightly inserted.

Figure 6.4 shows a cross-section of the links placed inside a tube. In case (a), the robot is always likely to advance because the vertical surfaces acting from both top and bottom generate sufficient traction to advance (similar to the motion between two surfaces), and the thrust force on the robot is:

$$F_{thrust}^{(a)} = 2\mu \cdot F_{normal} \cdot \quad (64)$$

Case (b) also enables the advancement of the robot, since the tips of the links corners also produce propulsion, and thus:

$$F_{thrust}^{(b)} = 4\mu \sqrt{F_{normal}^2 + F_{side}^2} \cdot \quad (65)$$

However, in case (c), the side forces resist the motion and the robot can only advance if:

$$F_{thrust}^{(c)} = 2\mu (F_{normal} - F_{side}) > 0. \quad (66)$$

In other words, the robot will advance if the thrust forces from the vertical surfaces are larger than the friction forces acting over the sides of the robot. Note that locomotion may still occur even if the side forces are larger than the normal forces since the links produce a slight propulsion at the side of their tips. To determine the normal and side forces, we carried out mechanical experiments in the next subsection 6.2.2.

6.2.2 Experiment System: Forces Measurement Device for Flexible Tubes

To evaluate the forces acting on the robot inside a compliant tube such as in cases (b) and (c), we developed an experimental force-measuring device. The device, which holds 3D printed wave-like parts, is used to increase the distance between the wave parts while measuring the forces acting on one of the corners using a force sensor (see Figure 6.5).

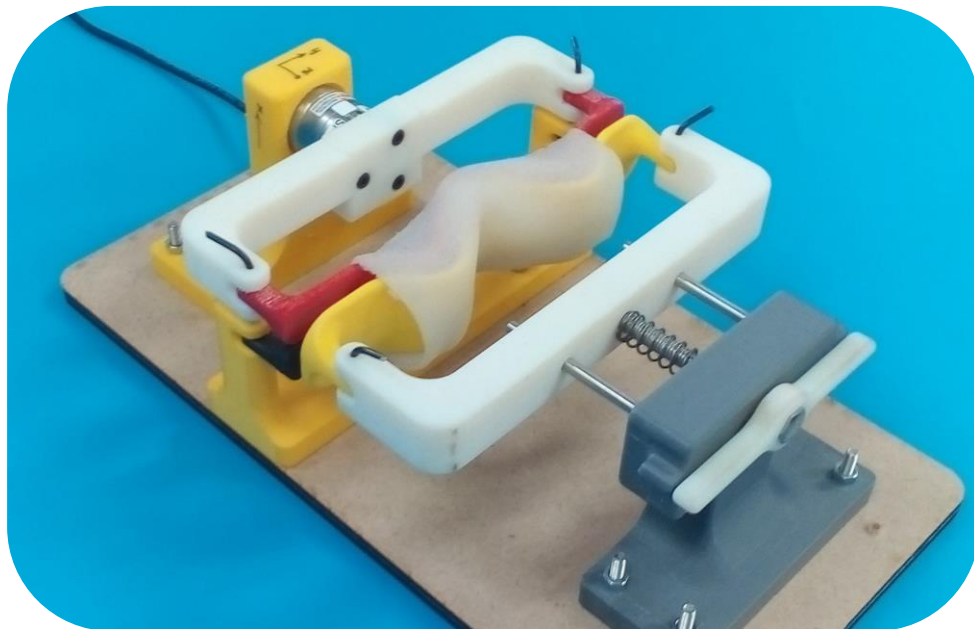
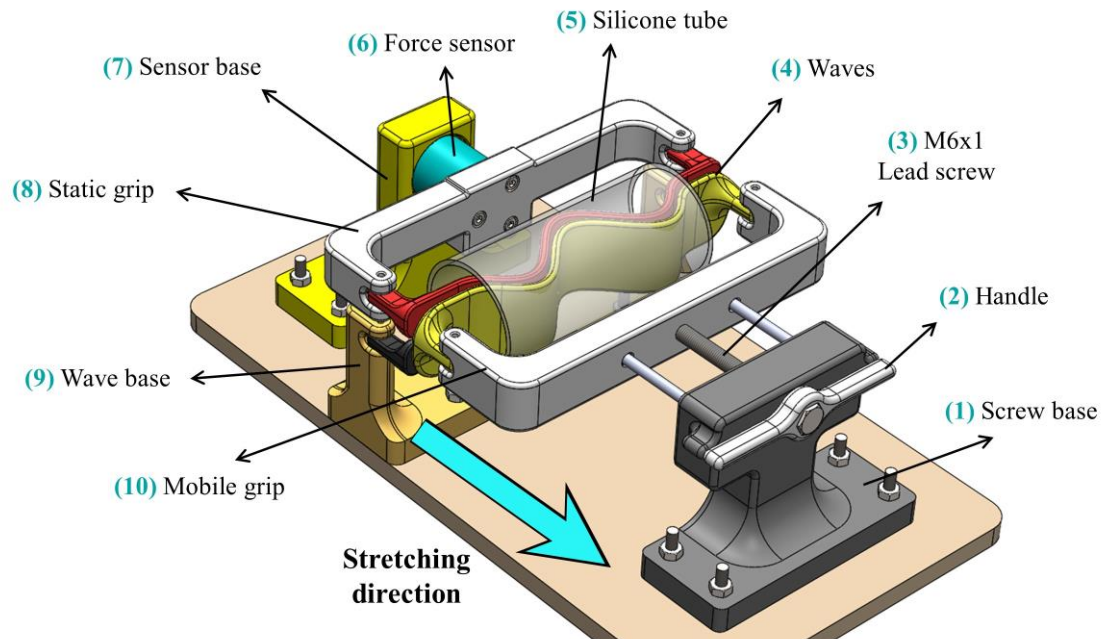


Figure 6.5: The force measurement experimental system that enables stretching the silicone tube and measure the forces acting on the waves, CAD model and the built system.

There are three waves (4 in Figure 6.5) that together simulate the outer shape of the wave of the robot, magnified twice and placed inside a 30 mm diameter silicone tube (5). The device increases the distance between the waves and as a result stretches the silicone tube to simulate the wave of the robot pressing against the tube wall. The handle (2), connected to a M6 (1 mm pitch) lead screw (3) placed on the screw base (1), is used to increase the distance between the waves, by pulling the yellow wave held by the mobile grip (10).

The bottom black wave is placed with a small distance from and underneath the red wave and is fixed to the ground with the wave base (9). The yellow wave is stretched away from the red wave, while the latter is fixed to the static grip (8) connected to the force sensor (6). Therefore, during the stretching the red wave and the force sensor measure the forces along two axes: normal force and side force, as shown in Figure 6.6.

We used an ATI Inc. Nano25 F/T sensor which has a resolution of 1/48 N and 1/16 N on the F_x , F_y and F_z axes, respectively. The sampling rate of the system is 4000Hz, and we smoothed the data by averaging 200 neighboring data points.

There are two models of the 3-piece waves:

- Normal stretching waves - Figure 6.6, top: The distance between the waves is increasing the amplitude of the wave (stretching in the normal direction to the waves). In this configuration, the normal force is in the stretching direction and the side force is perpendicular.
- Sideways stretching waves - Figure 6.6, bottom: The distance between the waves is increasing the width of the wave, while the amplitude remains constant (stretching sideways). In this configuration, the side force is in the stretching direction and the normal force is perpendicular.

When placed in the device, each wave model simulates the stretching of the tube in a different direction. By measuring the forces along the two axes while distancing the waves, we can determine the forces acting on the robot in the normal direction and from the side, and thus calculate which force is larger in cases (b) and (c). Multiplying the forces by the surface COF yields the thrusting and resisting forces acting on the robot during motion.

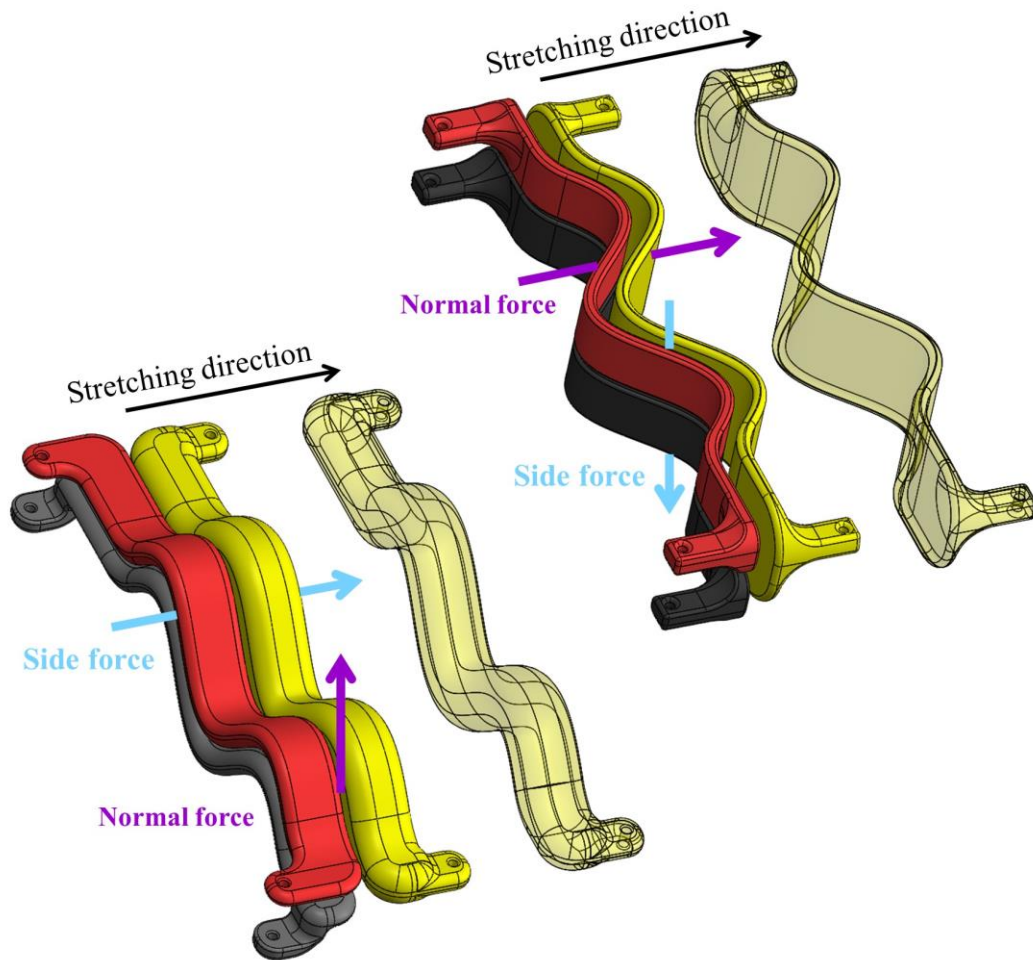


Figure 6.6: Three-piece wave models that demonstrate the robot's wave. The transparent parts show the location of the yellow wave after stretching. Top: Normal stretching waves. Bottom: Sideways stretching waves.

6.2.3 The Experiments of Forces Measurement

The waves were placed inside the device, and we measured the forces applied on the red piece of the wave while increasing the distance between the waves in 1 mm intervals, by rotating the screw 1 rotation at a time (6 mm lead screw with 1 mm pitch). We used Lithium Grease in the experiment to guarantee equal stretching of the tube and eliminate the effects of the stretching direction. Then we measured the force in the release of the waves, i.e. when reducing back the distance between the waves.

We performed the same experiment for both models of the waves. Figure 6.7 shows both models of the waves (a – normal waves, b – side waves) in the initial position (left) and in the stretched position (right).

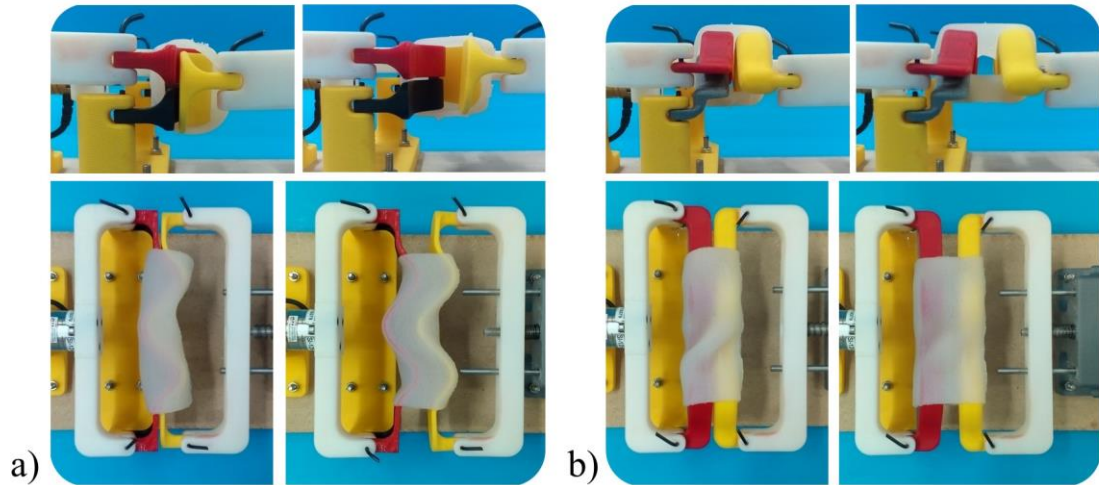


Figure 6.7: Experiment with a 2mm-wall-thick tube. Front view (up) and top view (down) showing the tube in the starting position and in the stretched position. a) Normal stretching waves. b) Side stretching waves.

We describe the wave parameters during the stretching by the ratio of A (the amplitude of the outline of the three waves together) to w (width of the waves together). When separating the normal waves (Figure 6.7a), the amplitude of the waves was increased and thus A/w increases. However, when separating the side waves (Figure 6.7b), we increase the width of the waves and thus the ratio A/w decreases. The starting ratio A/w was $1/3$, when the amplitude of both models of the waves was $A_0=10$ mm, and the width was $w_0=30$ mm. The ratio A/w ranged from 0.22 to 0.93 during the experiment, reduced to minimum of 0.22 when stretching the side waves, and maximized to 0.93 when stretching the normal waves.

The results for the normal forces as a function of the side forces are presented in Figure 6.8, left for the normal waves, and right for the side waves. The solid line represents the state where the normal and side forces are equal. For both models of the wave, the normal forces are larger than the side force, located above the solid line.

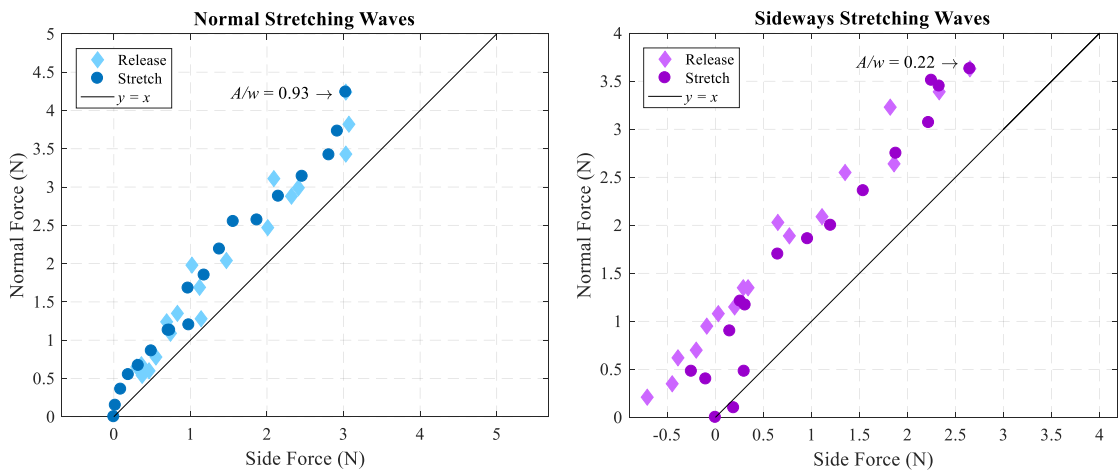


Figure 6.8: Results of the force measured in the experiment, for the normal waves (left) and the side waves (right)

The forces for both models of the waves are shown in Figure 6.9. The solid line is similar to the previous figures, whereas the dashed lines present the linear fit of the results, showing that the normal forces were larger than the side forces by 50% and 36% for the normal and side waves, respectively. These results suggest that the robot is likely to generate propulsion and advance inside flexible tubes (see our experiment in subsection 6.3.2).

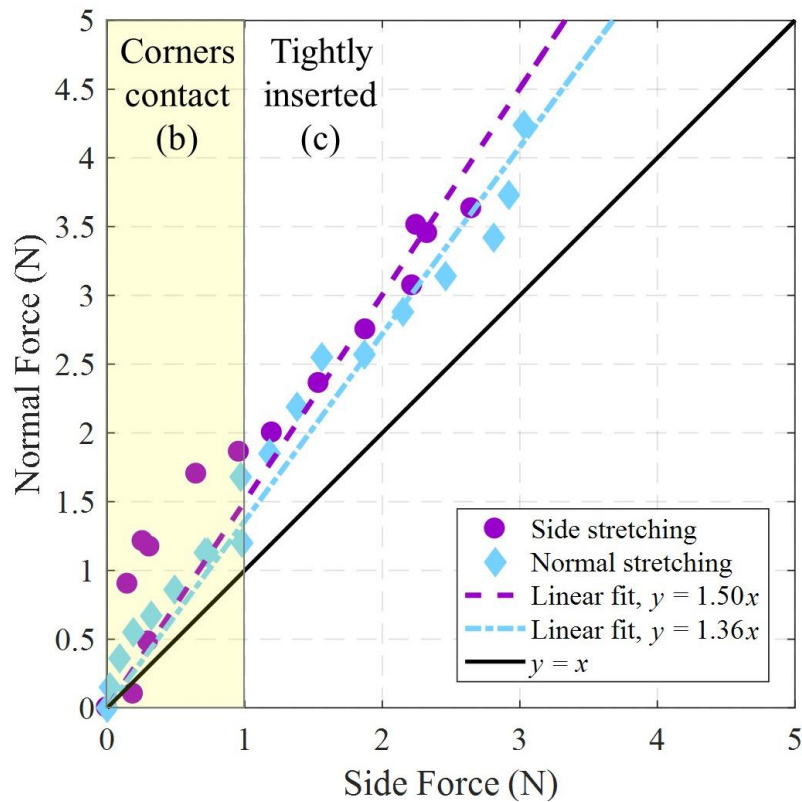


Figure 6.9: Forces measured in the experiment in the normal direction vs. sideways. The solid line corresponds to $F_{normal}/F_{side}=1$, showing that the normal forces are always larger than the side forces.

Given that the internal perimeter of the tube is 94 mm (internal diameter of 30 mm), our experiments started with the corners contacting case (b) and ended at the tightly inserted case (c) (see Figure 6.9). For normal stretching, the external perimeter of the waves ranged from 80 mm to 116 mm, resulting in 23% strain of the tube, whereas in the side stretching waves, the range was from 80 mm to 112 mm, resulting in 19% strain.

Using (66), we evaluated the thrust forces by subtracting the side forces from the normal forces and multiplying them by the COF. Note that in our experiments we measured a single corner of the wave (i.e., we measured the forces on the red piece of the wave in Figure 6.6). Therefore, the total normal and side forces are four times larger. For example, using Figure 6.9, if the side and normal forces are respectively 2 and 3 Newtons, the total side force is 8 Newtons and the total normal force is 12 Newtons. Assuming a COF of 0.2 [52], the thrust force would be at least 0.8 Newtons.

6.3 Motion Experiments in Tubes

This section presents the experiments performed inside flexible tubes, as well as the design and manufacturing of the tubes.

6.3.1 Experiment System: Flexible Tubes

To simulate movement inside intestines, we designed and 3D printed a mold that was used to cast flexible tubes made from Dragon Skin silicone. We created two 5-piece molds that were printed in VeroWhitePlus, to cast tubes that are 15 mm in diameter, 150 mm long, with wall thickness of 1 mm and 2 mm (Figure 6.10).

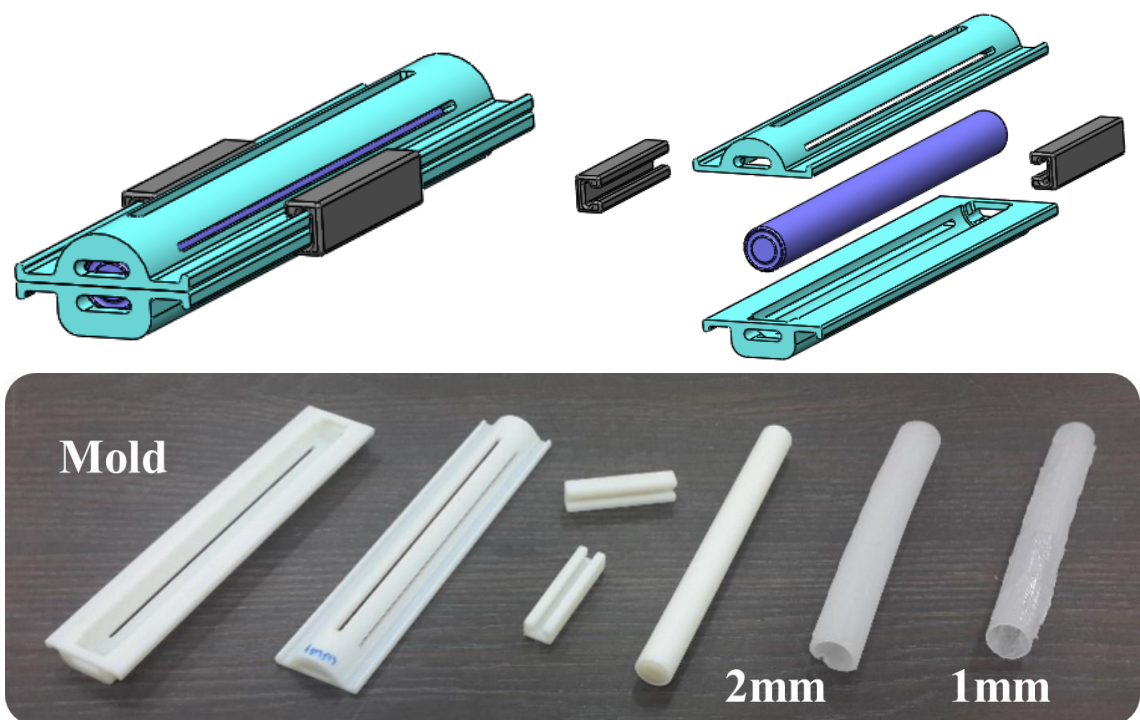


Figure 6.10: Top - 3D model of the molds. Bottom – a mold and the flexible tubes

6.3.2 Experiments of Motion inside Compliant Tubes

We ran the robot inside the tubes, as shown in Figure 6.11 (also see video). The tube was pinned to the table in both ends to keep it from moving during the robot's motion.

The robot reached a maximum speed of 19.8 mm/sec inside the tubes (AVG = 18.3 mm/s, STD = 0.9 mm/s). The robot's motion was also examined inside a curved tube. The experiment showed that the robot can crawl and advance inside the curved tube (see Figure 6.11, right).

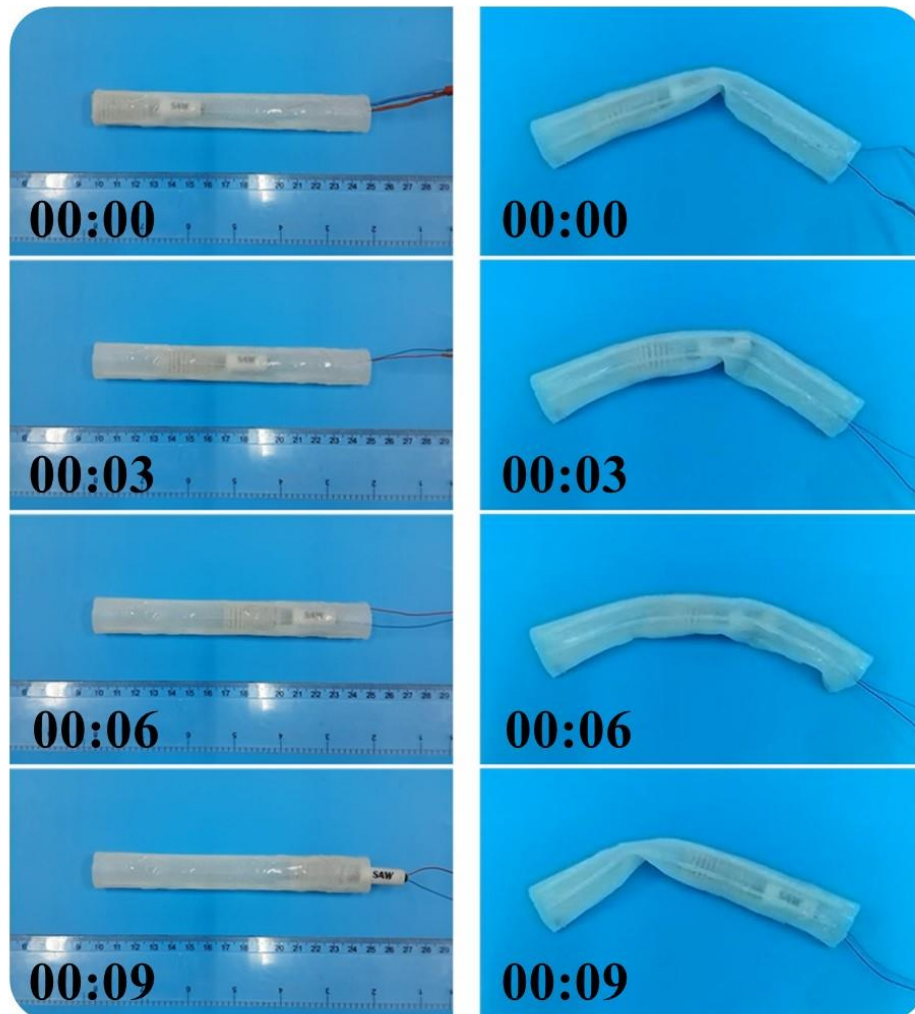


Figure 6.11: The robot moving inside a 1 mm thick tube (left) and in a curved 1 mm thick tube (right)

6.4 Motion Experiments in Pig's Intestines

We tested the robot's locomotion inside pig's intestines (ex-vivo). We performed the experiment twice with different models of the robot: the first experiment was with model 5 and the second experiment was with model 7 (improved by narrowing the head and the end of the wave. see models and designs in appendix [A]), after drawing conclusions from the first experiment and improving the design of the robot.

Screenshots from the first experiment are shown in Figure 6.12. First, we placed the robot between two flexible surfaces, coated with slices of the small intestine from both sides (Figure 6.12 right). The robot crawled backwards and forward, and was able to advance between the intestines surfaces successfully, and overcame the low COF of the intestines. The robot reached a velocity of 11 mm/s.

Next, we placed the robot inside a tube part of the large intestine (Figure 6.12 left). This experiment was mostly successful, as the robot was able to advance with the entire wave until the head entered the bowel. Moreover, the robot was able to advance despite the low COF, because of the bowels' walls that apply a slight radial force on the robot and help it advance. However, the head interrupted the motion and prevented the robot from fully entering the intestine in backwards motion (wave first), and the advance rate of the robot was much lower compared to previous experiments due to the low COF and the fluids secreted from the intestinal walls. In forward motion (head first) the robot was able to exit the intestines even when starting the motion when the head was inside the intestine (as shown in the screenshots).

Nevertheless, compared to the past models of the robot previously created in the lab, this experiment shows a major improvement of the robot advancing inside the intestines while the previous models could not. The robot reached a velocity of 3.4 mm/sec.

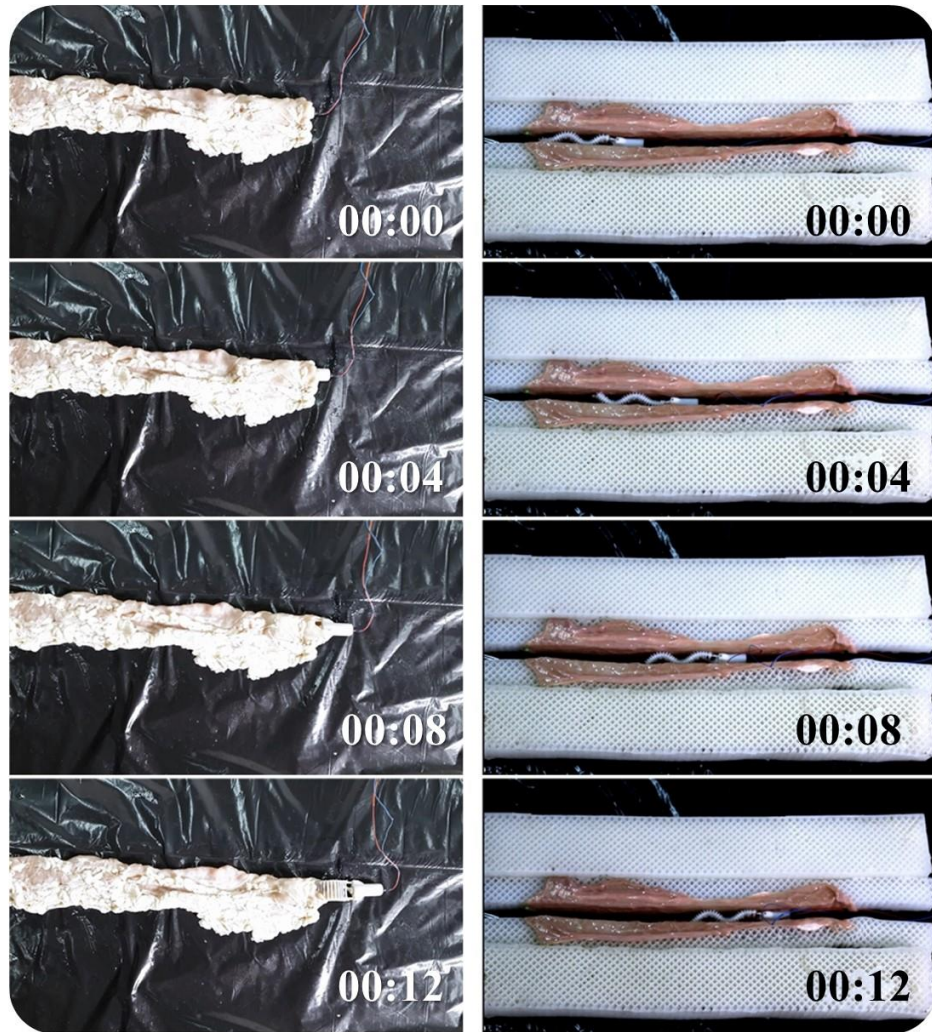


Figure 6.12: First experiment in pig's intestines, model 5.

The second experiment was performed with an improved model of the robot, as mentioned. This time we placed the robot inside the small intestine in three different shapes, while pressing lightly on the robot with this plastic to simulate the pressure of internal organs on the intestines inside a human body. First, the intestine was placed straight on a table, as shown in Figure 6.13. The robot reached a velocity of 10.3 mm/sec, which is three times higher than the experiment conducted with the earlier model.

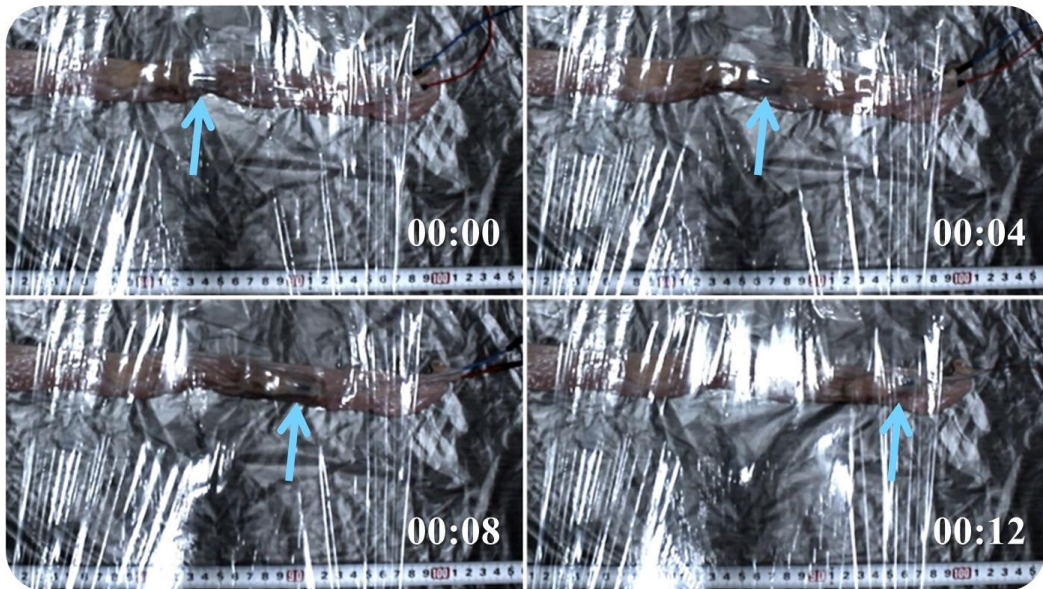


Figure 6.13: Second experiment in pig's intestines, straight shape with model 7b

Next, we placed the intestines in two curved shapes, to test the robot's ability to overcome curves in the tube. The screenshots from the videos are shown in Figure 6.14.

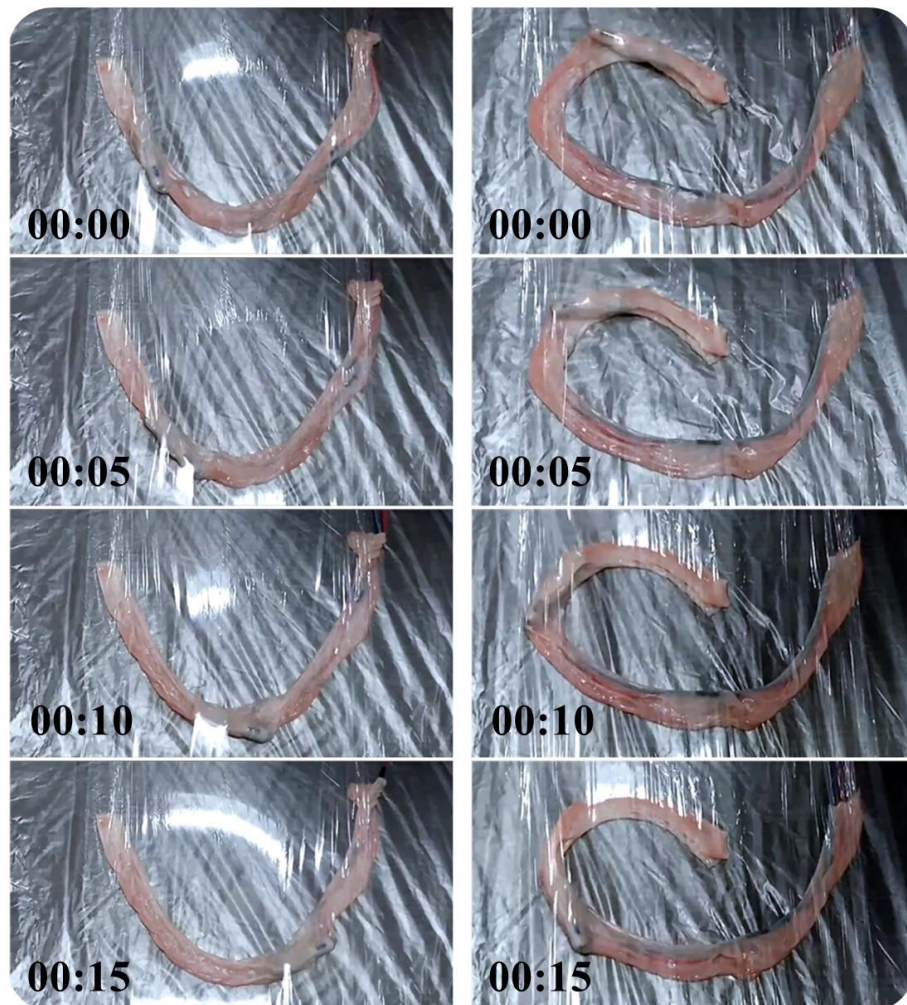


Figure 6.14: Second experiment in pig's intestines, model 7v

The second experiment in the bowels was a success. We were able to place the robot in various shapes of the tube and see that it can crawl even when there are curves in the tube. However, we noticed that the robot's advancing rate in backwards motion was much lower than the motion forward. Crawling backwards the robot was able to crawl only in specific conditions and very slowly. We noticed that this happens because of a distance between the head and the first link, "accumulating" intestinal tissue in the gap. This should be corrected in future models to optimize motion inside the intestines moving backwards.

7 Conclusions

This thesis reviews the locomotion analysis, simulations and experiments of our newly designed miniature wave-like robot, which was prompted by possible future medical applications, where the robot will need to crawl inside biological vessels such as the intestines.

We showed the general design concept and the motion principle. We then began our dynamic analysis with the general formulation of the locomotion physics for wave robots over a rigid surface and obtained analytical models of locomotion. We found that due to the friction of the head with the surface, the robot might partly advance and partly slide without advancing. This result was validated numerically in a simulation and experimentally using a model of our wave robot.

When crawling between two surfaces, the robot is likely to advance under almost all conditions because of the thrust generated when creating contact of the top and bottom of the links with the surfaces. A similar result is likely obtained if the robot is moving inside a flexible tube, given that the pressure applied on the robot is low.

In the case of crawling between curved surfaces, we developed an analytical model of the motion and showed that the robot can stick to the inner wall or to the outer wall, depending on the friction coefficient of the surface. This critical COF was calculated using a numerical simulation with accuracy of 0.0001.

Considering crawling inside a tube with high pressure from the tube on the robot, when the shape of the tube is deformed and the robot is tightly inserted, we experimentally determined the normal (which produce the thrust) and side (resisting) pressure forces acting on the robot. We found that for a much larger interval, the normal forces were larger than the side forces, which is a sufficient condition for advancement inside tubes.

Finally, the miniature 3D printed models of the robot we developed were used to experimentally validate our analyses and simulations. The results of the experiments were highly consistent with our expectations since the robot was able to crawl over the different surfaces as predicted by our analyses. The robot crawled in a continuous motion between two straight surfaces, and moved in the advancing-sliding motion on a single surface, as was predicted in the simulation. Moreover, the robot succeeded in crawling inside pig's intestines placed in a curved shape.

8 References

- [1] P. Dario, P. Ciarletta, A. Menciassi, and B. Kim, "Modeling and experimental validation of the locomotion of endoscopic robots in the colon," *International Journal of Robotics Research*, vol. 23, no. 4-5, pp. 549-556, 2004.
- [2] I. Kassim, L. Phee, W. S. Ng, G. Feng, P. Dario and C.A. Mosse, "Locomotion techniques for robotic colonoscopy," *IEEE Engineering in Medicine and Biology Magazine*, vol. 25, no. 3, pp. 49-56, 2006.
- [3] L. Phee, D. Accoto, A. Menciassi, C. Stefanini, M.C. Carrozza and P. Dario, "Analysis and development of locomotion devices for the gastrointestinal tract," *IEEE Transactions on Biomedical Engineering*, vol. 49, no. 6, pp. 613-616, 2002.
- [4] L. Phee, A. Menciassi, D. Accoto, C. Stefanini, and P. Dario, "Analysis of robotic locomotion devices for the gastrointestinal tract," *Robotics Research, STAR 6*, pp. 467-483, 2003.
- [5] A. Menciassi, D. Accoto, S. Gorini, and P. Dario, "Development of a biomimetic miniature robotic crawler," *Autonomous Robots*, vol. 21, no.2, pp. 155-163, 2006.
- [6] A. Menciassi, S. Gorini, G. Pernorio, and P. Dario, "A SMA actuated artificial earthworm," *Proceedings IEEE International Conference on Robotics and Automation*, pp. 3282-3287, 2004.
- [7] B. Kim, S. Lee and J. Park, "Design and fabrication of a locomotive mechanism for capsule-type endoscopes using shape memory alloys (SMAs)," *IEEE/ASME Transactions on Mechatronics*, vol. 10, no.1, pp. 77-86, 2005.
- [8] B. Kim, H.Y. Lim and J. H. Park. "Inchworm like colonoscopic robot with hollow body and steering device," *JSME International Journal, Series C*, vol. 49, no. 1, pp. 205-212, 2006.
- [9] J. Lim, H. Park, J. An, Y.S. Hong, B. Kim, B.J. Yi, "One pneumatic line based inchworm-like micro robot for half-inch pipe inspection," *Mechatronics*, vol. 18, pp. 315-322, 2008.
- [10] J. Li, R. Sedaghati, J. Dargahi and D. Waechter, "Design and development of a new piezoelectric linear Inchworm Actuator," *Mechatronics*, vol. 15, pp. 651-681, 2005.
- [11] V.K. Asari, S. K. Irwan and M. Kassim, "A fully autonomous microrobotic endoscopy system," *Journal of Intelligent and Robotic Systems*, vol. 28, pp. 325-341, 2000.
- [12] A. Brett Slatkin, J. Burdick and W. Grundfest, "The Development of a Robotic Endoscope", *Experimental Robotics IV*. vol. 223, pp. 162-171, 1995.
- [13] B. Kim, M.G. Lee, Y.P. Lee, Y. Kim, and G. Lee, "An earthworm-like micro robot using shape memory alloy actuator," *Sensors and Actuators, A: Physical*, vol. 125, no. 2, pp. 429-437, 2006.
- [14] D. Chi and G. Yan. "From wired to wireless: a miniature robot for intestinal inspection," *Journal of Medical Engineering & Technology*, vol. 27, no.2, pp. 71-76, 2003.
- [15] K. Wang, G. Yan, P. Jiang and D. Ye, "A wireless robotic endoscope for gastrointestinal," *IEEE Transactions on Robotics*, vol. 24, no.1, pp. 206-210, 2008.
- [16] K. Wang, G. Yan, G. Ma and D. Ye, "An earthworm-like robotic endoscope system for human intestine: Design, analysis, and experiment," *Annals of Biomedical Engineering*, vol. 37, no. 1, pp. 210-221, 2009.
- [17] N. Saga, T. Seto, H. Takanashi and N. Saito. "Development of a peristaltic crawling robot using planar link mechanisms," *IEEJ Transactions on Electrical and Electronic Engineering*, vol. 3 no.1, pp. 72-78, 2008.
- [18] D. Glozman, N. Hassidov, M. Senesh, and M. Shoham, "A self-propelled inflatable earthworm-like endoscope actuated by single supply line," *IEEE Transactions on Biomedical Engineering*, vol. 57, no. 6, pp. 1264-1272, 2010.
- [19] D. Zarrouk, I. Sharf, and M. Shoham, "Conditions for worm-robot locomotion in a flexible environment: theory and experiments," *IEEE Transaction on Biomedical Engineering*, vol. 59, no. 4, pp. 1057-1067, 2012.
- [20] D. Zarrouk, I. Sharf, and M. Shoham, "Analysis and design of one degree of freedom worm robots for locomotion on rigid and compliant terrain", *ASME, Journal of Mechanical Design*, vol. 134, no. 2, 2012.
- [21] D. Zarrouk, I. Sharf, and M. Shoham, "Analysis of Wormlike robotic locomotion on compliant surfaces," *IEEE Transactions on Biomedical Engineering*, vol. 58, no. 2. pp. 301-309, 2011.

- [22] T. Manwell, T. Vitek, T. Ranzani, A. Menciassi, K. Althoefer, and H. Liu, "Elastic mesh braided worm robot for locomotive endoscopy," *Annual International Conference of the IEEE Engineering in Medicine and Biology Society.*, vol. 2014. pp. 848–851, 2014.
- [23] J. Y. Gao, G. Z. Yan, Y. B. Shi, H. L. Cao, K. Huang, and J. Liu, "Optimization design of extensor for improving locomotion efficiency of inchworm-like capsule robot," *Sci. China Technol. Sci.*, 2019.
- [24] F. Liu, K.M. Lee, and C.J. Yang, "Hydrodynamics of an Undulating Fin for a Wave-Like Locomotion System Design" *IEEE/ASME Transactions on Mechatronics*, vol. 17, no. 3, pp. 554-562, 2012.
- [25] D. Zarrouk, M. Mann, N. Degani, T. Yehuda, N. Jarbi, and A. Hess, "Single actuator wave-like robot (SAW): Design, modeling, and experiments," *Bioinspiration and Biomimetics*, vol. 11, no. 4. 2016.
- [26] H. Kimura, K. Shimizu, and Shigeo Hirose, "Development of Gmbu: Active-Wheel Passive-Joint Snake-Like Mobile Robot". *Journal of Robotics and Mechatronics*, Vol. 16, No. 3, 2004.
- [27] W. Hu, G. Z. Lum, M. Mastrangeli, and M. Sitti, "Small-scale soft-bodied robot with multimodal locomotion," *Nature*, vol. 554, no. 7690, pp. 81–85, 2018.
- [28] J. Ostrowski, J. Burdick, "Gait kinematics for a Serpentine Robot", *Proceedings of the IEEE International Conference on Robotics and Automation*, 1996.
- [29] M. Mori, S. Hirose, "Locomotion of 3D Snake-Like robots – Shifting and rolling Control of Active Cord Mechanism ACM-R3". *Journal of Robotics and Mechatronics*. vol. 18, no. 5. 2006.
- [30] G. Chirikjian, J.W. Burdick, "The Kinematics of Hyper-Redundant Robot Locomotion", *IEEE Trans. On Robotics and Automation*, vol. 11, no. 6, 1995.
- [31] J.W. Burdick, J. Radford, and G.S. Chirikjian, "Sidewinding Locomotion Gait for Hyper redundant robots". *Advanced Robotics*, vol. 9, no. 3, pp 195-216, 1995.
- [32] Z. Lu, S. Ma, B. Li and Y. Wang, "3D Locomotion of a Snake-Like Robot Controlled by Cyclic Inhibitory CPG Model". *Proceedings of the International Conference on Intelligent Robots and Systems*, 2006.
- [33] S. Hirose, E.F. Fukushima, "Snakes and Strings: New Robotics Components for Rescue Operations". *International Journal of Robotics Research*, vol. 23, pp. 341-349, 2004.
- [34] A. Wolf, H. Choset, HB Brown, R Casciola, "Design and Control of a Mobile Hyper-Redundant Urban Search and Rescue Robot", *International Journal of Advanced Robotics*, vol. 19 (8) pp.221-248, 2005.
- [35] PhD thesis. G.J. Goldman, "Design space and motion development for a pole climbing serpentine robot featuring actuated universal joints", PhD thesis, *Virginia Polytechnic Institute and State University*, 2009.
- [36] G. Taylor, "Analysis of the swimming of microscopic organisms." *Proceedings of the Royal Society of London A: Mathematical, Physical and Engineering Sciences*. Vol. 209, No. 1099, pp. 447-461, 1951.
- [37] G. Taylor, "The action of waving cylindrical tails in propelling microscopic organisms." *Proceedings of the Royal Society of London. Series A, Mathematical and Physical Sciences*, pp. 225-239, 1952.
- [38] T. Hu, L. Shen, L. Lin and H. Xu, "Biological inspirations, kinematics modeling, mechanism design and experiments on a undulating robotic fin inspired by *Gymnarchus niloticus*", *Mechanisms and Machine Theory*, vol. 44, pp. 633-645, 2009.
- [39] A. S. Boxerbaum, K. M. Shaw, H. J. Chiel, and R. D. Quinn, "Continuous wave peristaltic motion in a Robot", *The International Journal of Robotics Research*, vol. 31, no. 3, pp. 302–318, 2012.
- [40] L. Chen, S. Ma, Y. Wang, B. Li, and D. Duan, "Design and modelling of a snake robot in traveling wave locomotion," *Mechanism and Machine Theory*, vol. 42, no. 12. pp. 1632–1642, 2007.
- [41] K.A. Daltorio, A. S. Boxerbaum, A. D. Horchler, K. M. Shaw, H. J. Chiel, and R. D. Quinn "Efficient worm-like locomotion: slip and control of soft-bodied peristaltic robots", *Bioinspiration and Biomimetics*. Vol. 8, doi:10.1088/1748-3182/8/3/035003, 2013.
- [42] A. D. Horchler et al., "Peristaltic Locomotion of a Modular Mesh-Based Worm Robot: Precision, Compliance, and Friction," *Soft Robot*. vol. 2, no. 4, pp. 135–145, 2015.
- [43] A. D. Horchler et al., "Worm-like robotic locomotion with a compliant modular mesh," *Lecture Notes in Computer Science (including subseries Lecture Notes in Artificial Intelligence and Lecture Notes in Bioinformatics)*, vol. 9222. pp. 26–37, 2015.
- [44] J. Chan, F. T. Pan, and Z. Li, "Design and Motion Control of Biomimetic Soft Crawling Robot for GI Tract Inspection," *Proc. World Congr. Intell. Control Autom.*, vol. 2018-July, pp. 1366–1369, 2019.

- [45] C. D. Onal, R. J. Wood, and D. Rus, "An origami-inspired approach to worm robots," *IEEE/ASME Transactions on Mechatronics*, vol. 18, no. 2. pp. 430–438, 2013.
- [46] K. Zhang, C. Qiu, and J. S. Dai, "Helical Kirigami-Enabled Centimeter-Scale Worm Robot With Shape-Memory-Alloy Linear Actuators," *Journal of Mechanisms and Robotics*, vol. 7, no. 2. p. 021014, 2015.
- [47] S. Miyashita, S. Guitron, K. Yoshida, S. Li, D. D. Damian, and D. Rus, "Ingestible, controllable, and degradable origami robot for patching stomach wounds," in *Proceedings - IEEE International Conference on Robotics and Automation*, 2016, vol. 2016-June, pp. 909–916.
- [48] N.K. Baek, I.H. Sung and D.E. Kim, "Frictional resistance characteristics of a capsule inside the intestine for microendoscope design," *Proc. Instn. Mech. Engrs*, vol. 218 Part H: Journal of Engineering in Medicine.
- [49] X. Wang and M.Q.-H. Meng, "Study of frictional properties of the small intestine for design of active capsule endoscope," *2006 1st IEEE RAS & EMBS International Conference on Biomedical Robotics and Biomechatronics*, 6 pp., 2006.
- [50] K.D.Wang and G.Z.Yan, "Research on measurement and modeling of the gastro intestine's frictional characteristics," *Measurement Science & Technology*, vol. 20, no. 1, 015803 (pp. 6), 2009.
- [51] Y.C. Fung. "Biomechanics, Mechanical Properties of Living Tissues". *Springer-Verlag*, New York, Inc. 1993.
- [52] J. S. Kim, I. H. Sung, Y. T. Kim, E. Y. Kwon, D. E. Kim, and Y. H. Jang, "Experimental investigation of frictional and viscoelastic properties of intestine for microendoscope application," *Tribology Letters*, vol. 22, no. 2. pp. 143–149, 2006.
- [53] B. Guo, Y. Liu, and S. Prasad, "Modelling of capsule–intestine contact for a self-propelled capsule robot via experimental and numerical investigation," *Nonlinear Dyn.*, no. i, 2019.
- [54] S. Guo, Q. Yang, L. Bai, and Y. Zhao, "Development of multiple capsule robots in pipe," *Micromachines*, vol. 9, no. 6, 2018.
- [55] M. E. Karagozler, E. Cheung, J. Kwon, and M. Sitti, "Miniature endoscopic capsule robot using biomimetic micro-patterned adhesives," *Proceedings of the First IEEE/RAS-EMBS International Conference on Biomedical Robotics and Biomechatronics*, 2006, BioRob 2006, vol. 2006. pp. 105–111, 2006.
- [56] M. Beccani, C. Di Natali, G. Aiello, C. Benjamin, E. Susilo, and P. Valdastri, "A Magnetic drug delivery Capsule based on a coil actuation mechanism," *Procedia Eng.*, vol. 120, pp. 53–56, 2015.
- [57] R. Eliakim, K. Yassin, I. Shlomi, A. Suissa, and G. M. Eisen, "A novel diagnostic tool for detecting oesophageal pathology: The PillCam oesophageal video capsule," *Aliment. Pharmacol. Ther.*, vol. 20, no. 10, pp. 1083–1089, 2004.
- [58] M. Wang, Q. Shi, S. Song, C. Hu, and M. Q.-H. Meng, "A Novel Relative Position Estimation Method for Capsule Robot Moving in Gastrointestinal Tract," *Sensors*, vol. 19, no. 12, p. 2746, 2019.
- [59] X. Zhao *et al.*, "Endoscopic Robot-assisted Simple Enucleation Versus Laparoscopic Simple Enucleation With Single-layer Renorrhaphy in Localized Renal Tumors: A Propensity Score-matched Analysis From a High-volume Centre," *Urology*, vol. 121, pp. 97–103, 2018.
- [60] H. L. Lee, "Endoscopic Submucosal Dissection Using Endoscopic Robot: Endoscopist's Future Destination," *Gut and Liver*, vol. 13, no. 4, pp. 381–382, 2019.
- [61] H. L. Kaan and K. Y. Ho, "Robot-Assisted Endoscopic Resection: Current Status and Future Directions," *Gut and Liver*, pp. 4–6, 2019.
- [62] F. Munoz, G. Alici, and W. Li, "A review of drug delivery systems for capsule endoscopy," *Adv. Drug Deliv. Rev.*, vol. 71, pp. 77–85, 2014.
- [63] L. Drory and D. Zarrouk, "Locomotion Dynamics of a Miniature Wave-Like Robot, Modeling and Experiments," *2019 International Conference on Robotics and Automation (ICRA)*, Montreal, QC, Canada, 2019, pp. 8422-8428. doi: 10.1109/ICRA.2019.8794015
- [64] G. J. Tortora and B. Derrickson, *Principles of Anatomy and Physiology*, 12th ed. John Wiley & Sons, Inc., 2009.
- [65] Engineering ToolBox, "Metals and Alloys - Densities," 2004. [Online]. Available: https://www.engineeringtoolbox.com/metal-alloys-densities-d_50.html.

9 Appendices

[A] Design Process and Model Evolution

This chapter will review the improvements made in the models throughout the design process and the solutions applied for the required modifications.

- Design Challenges and Solutions

The design challenges we encountered are presented in two sections: first, the challenges and improvements of previous models and based on past experiences. Second, challenges that were discovered during the work in the current research.

Table 9.1: Design challenges and the solutions suggested

#	Challenge	Solution
Past work improvements		
1	High friction of the robot moving inside pig's intestines.	Creating a more rounded shape for the links and adding fillets considering the motion direction and touching surfaces (Figure 9.2).
2	Difficulties in assembling the robot due to the size of the parts and multiple pins needed for the assembly.	Replacing the small pin connecting between adjacent links with the use of a nylon wire, thus decreasing the number of pins needed (Figure 9.3). Moreover, the previously two-piece links were merged to one piece, eliminating the need for pins. The latest model is comprised of brass links, thus eliminating the need for metal pins whatsoever.
3	Link size limitation due to 3 pins needed in each link and the diameter of the pins.	Purchasing a set of special pins with a diameter of 0.4 mm, allowing the design of the links to be more compact. Furthermore, the previous solution helped as well.
4	Minor advance of the robot between surfaces and difficulty to advance in pig's intestines due to the robot's low speed.	Increasing the Ar/L of the helix and adding spikes to the links to increase the robot's speed (Figure 9.6).
5	High friction between the parts of the robot, especially between the helix and the links – increasing load on the engine.	Creating a hole in the links and inserting a pin that will touch the helix during the motion, thus reducing the friction while maintaining a solid one-piece link.

Current design development	
6	<p>Twisting of the links connected with the nylon wire.</p> <p>Creating a bump in the links preventing the links from moving vertically from each other (Figure 9.5). Merging the two parts of the first link of the robot together.</p>
7	<p>The helix was very weak and broke easily due to the increase of the amplitude.</p> <p>Increasing the helix's wire diameter, resulting in the need to adjust the amplitude and the wavelength of the robot to maintain the AR. Additionally, a custom-made 3D printed bronze-steel helix was fabricated to increase the strength of the helix.</p> <p>The latest model is equipped with a brass helix (smoother and thus reduces friction).</p>
8	<p>The head of the robot interrupting the motion inside a tube.</p> <p>Re-design of the head to make it as narrow and short as possible, as well as the first link to narrower (Figure 9.8).</p>
9	<p>The robot having trouble to pass in tubes because of the wave's shape.</p> <p>Creating a round end to the wave by changing the shape of the last links, thus creating a narrower end to the tail.</p>

- Design Evolution and latest design

First, the previous smallest model of the robot was evaluated. The design is shown in Figure 9.1:

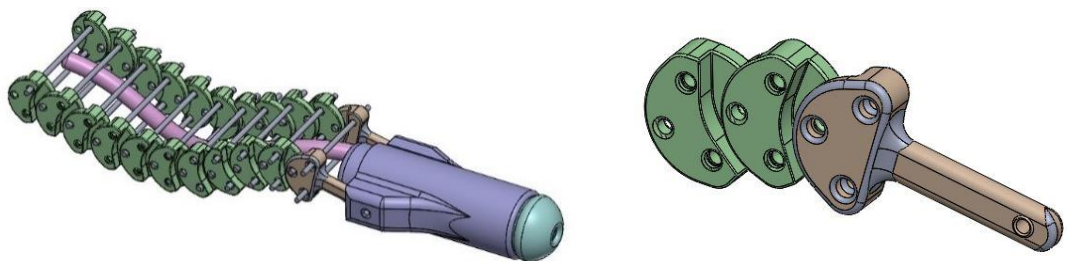


Figure 9.1: The latest design of the robot prior to this project

The first objective was to reduce friction to help the robot advance in the intestines. We refined the parts design and added fillets to smooth the outlines of the robot.

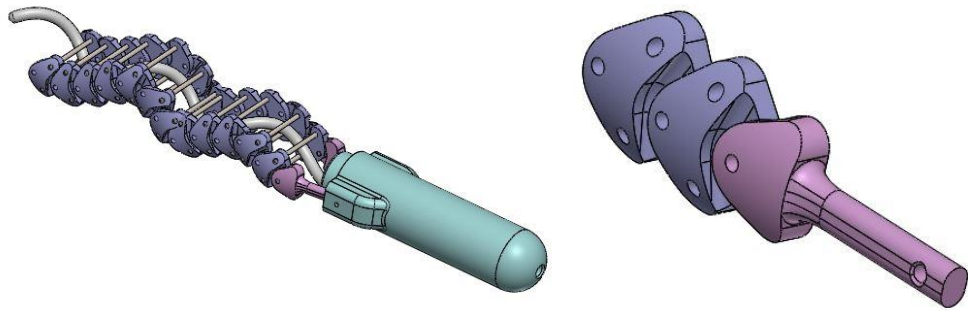


Figure 9.2: The first improvement made in the robot - round links (model 1)

Additionally, there was a need to improve the manufacturing method and make the assembly simpler, as the previous design was complicated and included inserting many metal pins that were hard to assemble. Then we came up with a new concept of connecting the links, using a 0.3-0.4 mm nylon wire along the wave:

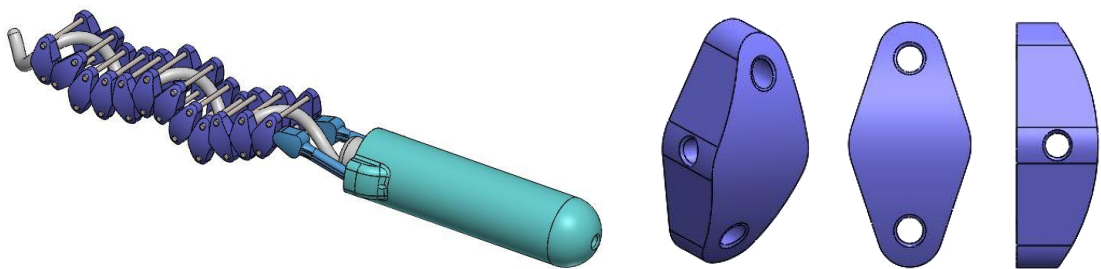


Figure 9.3: Design with the concept of using a nylon wire to connect the links (model 2)

The new concept had some advantages and some disadvantages. It was clear that the use of the wire saves space and allows the design to be more compact, in addition to a much easier assembly. However, the robot could not obtain a wave motion with this design. The tangent touching links and flexibility of the wire added to the links a degree of freedom in the z axis, thus enabling the links to create a twisting motion while the helix is rotating, as shown in Figure 9.4.

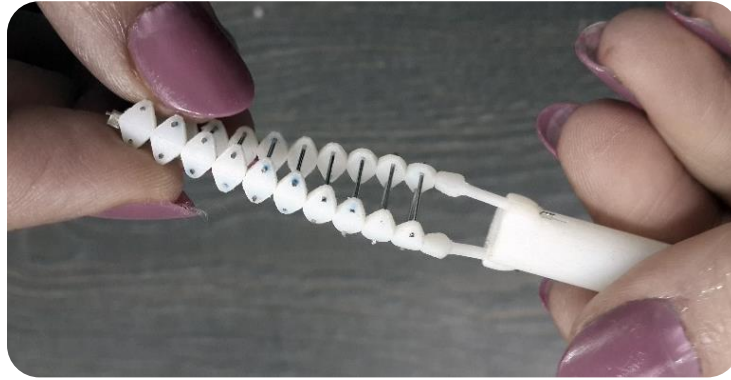


Figure 9.4: Demonstration of the twisting movement

To solve this issue, a bump was added to the links (Figure 9.5). By adding this bump and fitting the links together, it eliminated the degree of freedom mentioned above.

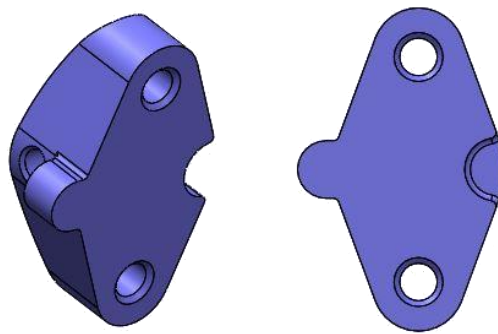


Figure 9.5: Added bumps to eliminate the twisting motion (model 3)

Next, to enable an easier assembly and strengthen the links, the two separate parts for each link were merged into one piece.

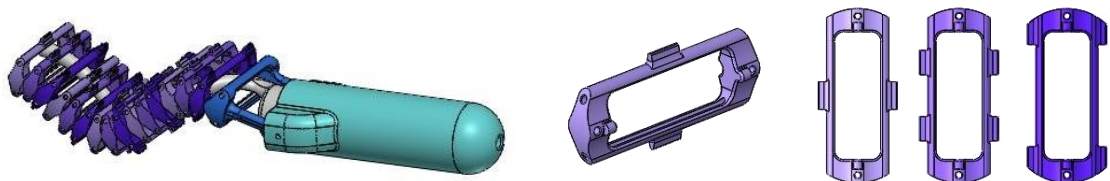


Figure 9.6: Creating one-piece links (model 4) and adding spikes to increase the robot's velocity (model 5)

Furthermore, spikes were added on top of the links to increase r , as explained in chapter 2.4 and 3.4, to increase the robot's velocity. The three different designs of the links allow the increase of r without collision of the links, as shown below.

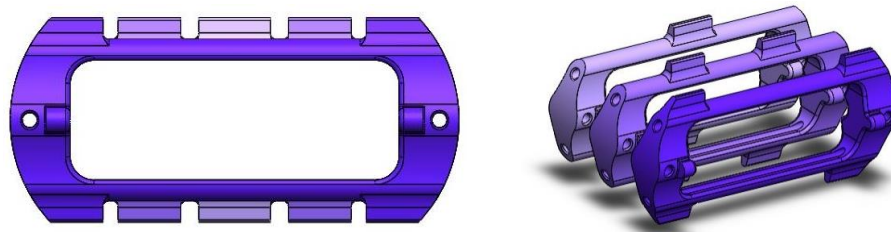


Figure 9.7: Front and isometric view of the three link designs, showing the spaces between the spikes to avoid collision of the links during motion

The next design of the robot had a shorter wave to make it more compact, in addition to a narrower head that will minimize the head's interruption to the robot's motion, because we noticed in the intestines experiment that the head slows down the robot.



Figure 9.8: Model 6 of the robot, improved by narrowing the head and adding fillets

In addition, we custom made a metal helix that is 3D printed in bronze steel (Figure 9.9). The helix must withstand pressure from intestinal walls and internal organs, and therefore we looked for a way to create a more durable helix. The disadvantage is that the robot is consequently a little heavier, but it also shifts the COM of the robot backwards, which is beneficial because the head and the motor are heavier than the wave. Furthermore, the metal helix decreases the COF of the helix with the links, allowing a smoother movement and reduction in energy consumption due to friction.

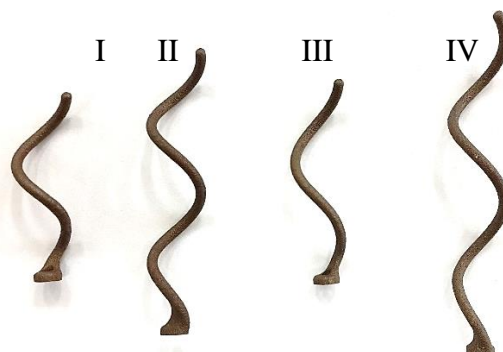


Figure 9.9: Metal helixes with different parameters

The helixes differ in two parameters: A/L ratio (see chapter 2.4): 0.15 in I+II, 0.2 in III+IV; and the length of the helix: one wave in I+III, two waves in II+IV.

The latest design of the robot (Figure 9.11) includes another improvement of the wave, by rounding the end links to create a curved end of the wave:

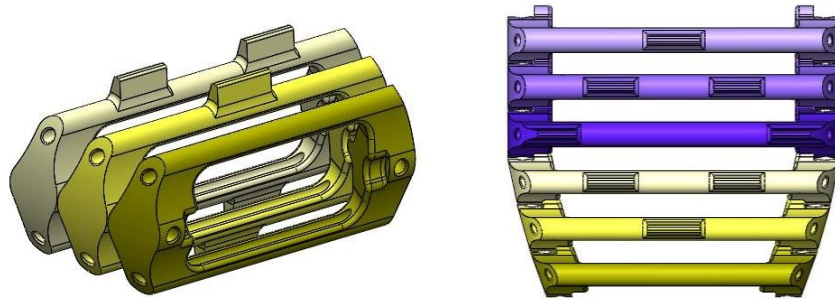


Figure 9.10: Left: Three models of the end links, Right: Top view of the end of the wave

These links will allow the robot a smoother movement while moving backwards, decreasing the interruption to the motion. To use these links we have adjusted the helix so that the amplitude at the end of the wave is slightly reduced.



Figure 9.11: Left – CAD model of the robot with narrow tail (model 7), Right – the assembled robot with the added special links in the end of the wave

The final model was manufactured in brass, both the links and the helix, to improve durability and strength (see Figure 9.12).

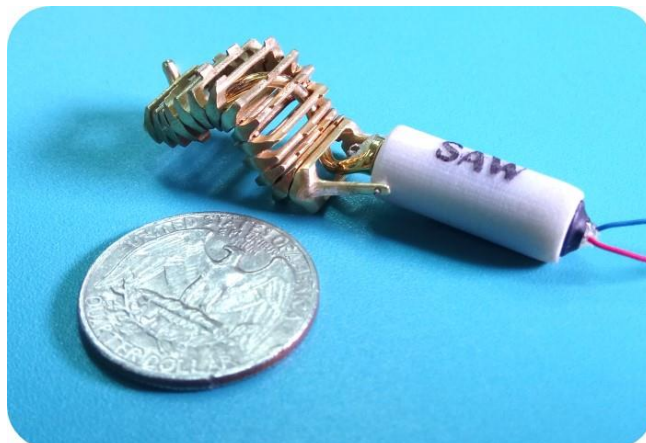
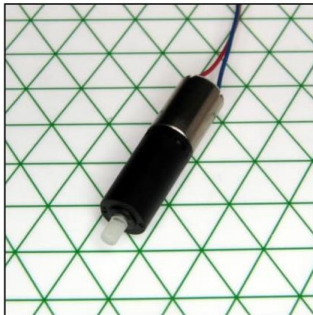


Figure 9.12: The final model of the robot, with brass helix and links

- Equipment and Materials

[B] DC Motor

<https://www.precisionmicrodrives.com/product/206-108-6mm-dc-gearmotor-21mm-type>



6mm DC Gearmotor - 21mm Type
Shown on 6mm Isometric Grid



**PRECISION™
MICRODRIVES**

**Product Data Sheet
Nano Planetary™
6mm DC Gearmotor - 21mm Type**

Model: 206-108

Ordering Information

The model number 206-108 fully defines the model, variant and additional features of the product. Please quote this number when ordering.
For stocked types, testing and evaluation samples can be ordered directly through our online store.

Datasheet Versions

It is our intention to provide our customers with the best information available to ensure the successful integration between our products and your application. Therefore, our publications will be updated and enhanced as improvements to the data and product updates are introduced.

To obtain the most up-to-date version of this datasheet, please visit our website at: www.precisionmicrodrives.com

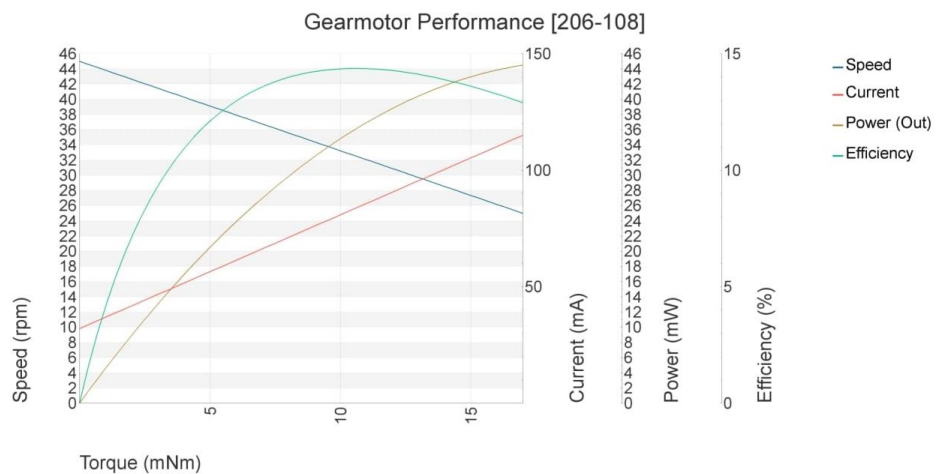
The version number of this datasheet can be found on the bottom left hand corner of any page of the datasheet and is referenced with an ascending R-number (e.g. R002 is newer than R001). Please contact us if you require a copy of the engineering change notice between revisions.

If you have any questions, suggestions or comments regarding this publication or need technical assistance, please contact us via email at: enquiries@precisionmicrodrives.com or call us on +44 (0) 1932 252 482

Key Features

Body Diameter:	6 mm [+/- 0.1]
Body Length:	20.8 mm [+/- 0.2]
Shaft Orientation:	Inline
Gear Ratio:	699.5 :1
Gearhead Type:	Planetary
Rated Operating Voltage:	3 V
Rated Load:	10 mNm
Rated Load Speed:	28 rpm
Typical Max. Output Power:	45 mW

Typical DC Gearmotor Performance Characteristics



[C] Objet Connex3 3D Printer

<http://www.stratasys.com/3d-printers/objet-350-500-connex3>



Objet350 and Objet500 Connex3



Driven by powerful PolyJet™ technology

Proven PolyJet 3D Printing is famous for smooth surfaces, fine precision and diverse material properties. It works a bit like inkjet document printing, but instead of jetting drops of ink onto paper, the print head jets microscopic layers of liquid photopolymer onto a build tray and instantly cures them with UV light. The fine layers build up to create a prototype or production part.

Along with the selected model material, the 3D printer features two support material options: SUP705, removed with a WaterJet; and SUP706, which is easily removed and soluble for automated post-processing and increased geometric freedom to print complex and delicate features and small cavities.

With its astonishingly realistic aesthetics and ability to deliver special properties such as transparency, flexibility and even bio-compatibility, PolyJet 3D Printing offers a competitive edge in consumer products prototyping, precision tooling and specialized production parts.

System Specifications	
Model Materials	Rigid Opaque: VeroPureWhite™, VeroWhitePlus™, VeroBlackPlus™, VeroGray™, Vero-Blue™, VeroCyan™, VeroMagenta™, VeroYellow™ Rubber-like: TangoPlus™, TangoBlackPlus™, TangoBlack™, TangoGray™ Transparent: VeroClear™ and RGD720 Simulated Polypropylene: Rigur™ and Durus™ High Temperature Bio-compatible
Digital Materials	Digital ABS™ and Digital ABS2™ in ivory and green Hundreds of vibrant, repeatable colors in opaque and translucent Rubber-like blends in a range of Shore A values and color Simulated polypropylene materials with improved heat resistance
Material Options	Over 1,000
Maximum Materials per Part	82
Support Material	SUP705 (WaterJet removable) SUP706 (soluble)
Maximum Build Size (XYZ)	Objet350: 342 x 342 x 200 mm (13.4 x 13.4 x 7.9 in.) Objet500: 490 x 390 x 200 mm (19.3 x 15.4 x 7.9 in.)
System Size and Weight	1400 x 1260 x 1100 mm (55.1 x 49.6 x 43.4 in.); 430 kg (948 lbs.) Material Cabinet: 330 x 1170 x 640 mm (13 x 46.1 x 26.2 in.); 76 kg (168 lbs.)
Resolution	X-axis: 600 dpi; Y-axis: 600 dpi; Z-axis: 1600 dpi
Accuracy	20-85 microns for features below 50 mm; up to 200 microns for full model size
Minimum Layer Thickness	Horizontal build layers as fine as 16 microns (.0006 in.)
Build Modes	Digital Material: 30-micron (.001 in.) resolution High Quality: 16-micron (.0006 in.) resolution High Speed: 30-micron (.001 in.) resolution
Software	Objet Studio intuitive 3D printing software
Workstation Compatibility	Windows 7/ Windows 8
Network Connectivity	LAN - TCP/IP
Operating Conditions	Temperature 18-25°C (64-77°F); relative humidity 30-70% (non-condensing)
Power Requirements	110-240 VAC 50/60Hz; 1.5 kW single phase
Regulatory Compliance	CE, FCC

[D] Printing material – VeroWhitePlus

<https://store.stratasys.com/stratasysstorefront/stratasys/en/Materials-%26-Service-Consumables/NA/Flavors/VeroWhitePlus%2C-RGD835/p/P034>

POLYJET MATERIALS DATASHEET

RIGID OPAQUE MATERIALS					
VERO PUREWHITE RGD837, VEROGRAY RGD850, VEROBLACKPLUS RGD875, VEROWHITEPLUS RGD835, VEROYELLOW RGD836, VEROCYAN RGD841, VEROMAGENTA RGD851					
	ASTM	UNITS	METRIC	UNITS	IMPERIAL
Tensile strength	D-638-03	MPa	50-65	psi	7250-9450
Elongation at break	D-638-05	%	10-25	%	10-25
Modulus of elasticity	D-638-04	MPa	2000-3000	psi	290,000-435,000
Flexural Strength	D-790-03	MPa	75-110	psi	11000-16000
Flexural Modulus	D-790-04	MPa	2200-3200	psi	320,000-465,000
HDT, °C @ 0.45MPa	D-648-06	°C	45-50	°F	113-122
HDT, °C @ 1.82MPa	D-648-07	°C	45-50	°F	113-122
Izod Notched Impact	D-256-06	J/m	20-30	ft lb/inch	0.375-0.562
Water Absorption	D-570-98 24hr	%	1.1-1.5	%	1.1-1.5
Tg	DMA, E=	°C	52-54	°F	126-129
Shore Hardness (D)	Scale D	Scale D	83-86	Scale D	83-86
Rockwell Hardness	Scale M	Scale M	73-76	Scale M	73-76
Polymerized density	D792	g/cm3	1.17-1.18		
Ash content VeroGray, VeroWhitePlus	USP281	%	0.23-0.26	%	0.23-0.26
Ash content VeroBlackPlus	USP281	%	0.01-0.02	%	0.01-0.02

[E] COM detailed values and calculations

The next table presents the calculations of the COM locations according to the equation mentioned before. Some of the values are measured manually, and some was calculated using the CAD model and the material densities (1.17 gr/cm³ for VeroWhitePlus [D], 8.586 gr/cm³ for Brass [65]).

Table 9.2: Detailed mass and length values and the COM calculations

Length	Mass	Density	Volume	Volume per link	Length per link	Mass per link	No. of links	COM
--------	------	---------	--------	-----------------	-----------------	---------------	--------------	-----

	mm	gr	gr/mm ³	mm ³	mm ³	mm	gr	mm
Head + Motor	23	2.1						
Vero Helix			0.0012		5.93	1.6235	0.0069	
Brass helix		1	0.0086		5.93	1.6235	0.0509	
1st Link Vero	3	0.12						
1st Link brass	3	0.75						
Vero link	2.1	0.04		41.19				
Pin	2.1	0.0175						
Link + 2Pins		0.0750						
Brass link	2.1	0.398	0.0086	46.32				
Vero Helix + Links		1.3					15	38.2
Brass Helix + Vero links		2.0					15	38.2
Brass Helix + Links		6.6					13	36.6
Head + Motor		2.2						11.5
Total Vero		3.5						21.8
Total Vero + Brass		4.2						24.4
Total Brass		8.7						30.4

[F] Simulation of crawling on a single surface

```

close all, clear F
set(0,'DefaultfigureColor',[1 1 1]) % White background color for graphs

%% Parameters %%
muW_H = 1; % mu wave / mu head
L = 30; % In mm, the wave length = pitch
k = 2*pi/L; % Wave number
num_of_waves = 1.15; % Tail length - number of waves in
the helix
x = 0:0.05:L*num_of_waves; % In mm, x coordinate
r = 2.7; % In mm, the height of the links
T = 1; % period
f = 1/T; % frequency
w = -2*pi*f; % In rad/sec, the angular frequency
A = 5; % In mm, the wave amplitude
x_2 = 30; h_com = -A+5.7; % In mm, distance of COM from start
of the head / floor
v_link = abs(((2*pi)^2)*A*f*r/L); % Velocity of the tip of the link
touching the floor.
line = 15; % Line width of the wave&head
head_ang = 0.15; % Tilt angle of the rectangle head
n = 0; % Int counter for the wave
advance_t = 0; % counter for the duration the robot
moves
dt = 0.025;
ii = 0;
COM_img = imread('COM sign.png');

%% Plot loop %%
end_time = 5;
start_pause = 0;
figure('units','normalized','outerposition',[0.1 0.1 0.55 0.7]), hold on
for t = 0:dt:end_time
    %% Wave
    hold off
    pause(dt)
    y = A*sin(k*x-w*t); % Wave shape
    plot(-x,y, 'linewidth',line, 'color', [0 0.447 0.741]), xlabel('x
(mm)'), ylabel('y (mm)'), hold on; % Plot of the wave
    set(gca,'units','normalized','position',[0.09 0.07 0.88 0.96]), hold
on
    axis equal, set(gca, 'gridlinestyle','--', 'xlim', [-max(x)-10 -
x(1)+40], 'ylim', [-30 22], 'FontName', 'Times New Roman',
'FontSize',22), grid on;
    %% text, floor
    text_pos_x = get(gca,'xlim'); text_pos_y = get(gca,'ylim');
    % Location for text on plot
    % text(text_pos_x(2)-20,text_pos_y(2)-5,['t = '
num2str(floor(2*t)/2,'%1f') ' sec'],'FontName', 'Times New Roman',
'FontSize',32); % write t = x sec
    text(text_pos_x(1)+3.5,text_pos_y(2)-5,[num2str(t/(2*T),'%1f') '
Cycles'],'FontName', 'Times New Roman', 'FontSize',32, 'FontWeight',
'Bold'); % write x.x cycle
    patch([-min(x)+40 -min(x)-50 -min(x)-50 -min(x)+40], [min(y)-1
min(y)-1] text_pos_y(1) text_pos_y(1)], [0.7843 0.7843 0.7843],
'EdgeColor', [0.7843 0.7843 0.7843]); % Floor plot
    %% COM
    image('CData',COM_img,'XData',-[min(x)-28+x_2-1.5 min(x)-
28+x_2+1.5],'YData',[h_com-1.5 h_com+1.5])

```

```

%% Head
x_head = [min(x)-27 min(x)-27+22*cos(head_ang) min(x)-
27+22*cos(head_ang)-8*sin(head_ang)...
min(x)-27-8*sin(head_ang) min(x)-27];
% x coordinates for rect head, starting in the touching point
y_head = [min(y)-0.7 min(y)-0.7+22*sin(head_ang) min(y)-
0.7+22*sin(head_ang)+8*cos(head_ang)...
min(y)-0.7+8*cos(head_ang) min(y)-0.3];
% y coordinates for rect head
patch(-x_head, y_head, [0 0.447 0.741], 'EdgeColor', [0 0.447
0.741]); % Plot of the head
%% First link
plot(-[min(x) (x_head(2)+x_head(3))/2], [y(1)
(y_head(2)+y_head(3))/2], 'linewidth',line, 'color',[0 0.447 0.741]); %
First link plot, from the head to start of the wave
%% Contact point
x_contact = ((1.5+2*n)*pi + w*t)/k-2;
plot(-x_contact-2,-A-2.2, '^', 'color',[0 0.447 0.741],
'MarkerSize',13, 'MarkerFaceColor','c')
%% Triangles
gap = 18; % gap between
triangles
triangle_range = 50 + abs(w)*12*end_time; % range for
plotting triangles
triangles_x = -triangle_range:gap:triangle_range; % x vector for
triangles
triangles_y = ones(1,length(triangles_x))*(-A-9);
plot(triangles_x,triangles_y-2, '^', 'MarkerSize',35, 'color', [1 1
1], 'MarkerFaceColor', [1 1 1])
plot(triangles_x+gap/2,triangles_y, 'v', 'color', [1 1 1],
'MarkerSize',35)
%% Advancing condition
x_w = abs(min(x)-x_contact)+27-x_2; % Distance between
COM and contact point
if w<0
if x_w <= x_2*muW_H
x = x - v_link*dt; % Advancing the
robot if x1<x_com
advance_t = advance_t + dt; % Counting the
advancing time
else
text(text_pos_x(1)+5,text_pos_y(1)+7,'Sliding','FontName',
'Times New Roman', 'FontSize', 34, 'FontWeight', 'Bold', 'color', 'k');
% write Sliding
pause(3*dt)
ii = ii+1;
F(ii) = getframe(gcf);
end
if x_contact-3 <= min(x) % going back to the
start of the wave - counting n
n = n+1;
end
else
if x_w <= x_2*muW_H
x = x + v_link*dt; % Advancing the
robot if x1<x_com
advance_t = advance_t + dt; % Counting the
advancing time
else
text(text_pos_x(1)+5,text_pos_y(1)+7,'Sliding','FontName',
'Times New Roman', 'FontSize', 40, 'FontWeight', 'Bold', 'color', 'k');
% write Sliding
pause(3*dt)
ii = ii+1;

```

```

        F(ii) = getframe(gcf);
    end
    if x_contact+3 >= max(x)           % going back to the
start of the wave - counting n
        n = n-1;
    end
end
ii = ii+1;
F(ii) = getframe(gcf);

% Pause in the beginning
if start_pause==0           % pausing the start
of the video in 1 sec
    pause(1)
end
start_pause=start_pause+1;

%% Changing motion direction
%   if t==2           % changing the
motion direction
%       w=-w;
%   end
end

% Video
video = VideoWriter('SAW Simulation.avi','Uncompressed AVI');
open(video)
writeVideo(video,F)
close(video)

```

[G] Simulation of crawling between curved surfaces

As shown in section 5.2, the Matlab simulation considers surface and robot parameters to simulate the motion of the robot between surfaces. First the simulation calculates the sum of all the forces applied on the robot, considering friction forces, self-thrust force and added thrust force. Using the forces and torques, the simulation calculates the acceleration of the COM with:

$$\Sigma F = ma, \quad (67)$$

While the forces and the mass is known. With the acceleration it calculates the velocity:

$$V_i = a_i \cdot dt + V_{i-1}, \quad (68)$$

While V_i is the calculated velocity of iteration i , a_i is the acceleration from (67), dt is the time increment and V_{i-1} is the velocity from the last iteration. Similarly, the location is calculated by:

$$X_i = V_i \cdot dt + X_{i-1}. \quad (69)$$

These acceleration, velocity and location calculation is performed for both x and y direction, while for θ axis we use

$$\Sigma M = I\ddot{\theta}. \quad (70)$$

(70) is used to create a rotation matrix and establish the final location of the four corners of the robot. Now the simulation will examine the penetration of each of the corners of the robot into the wall, by evaluating whether or not

$$X_i > r_{out}, \quad (71)$$

when X_i is the distance of point i from the center of the radius, and therefore if exists it indicates that there is penetration of point i into the outer surface. If penetration was found, the simulation adds applied force from the wall by

$$F_{wall} = k_w x_{pen}, \quad (72)$$

while k_w is the wall stiffness and x_{pen} is the size of penetration to the wall. The force is then split into two – normal force in the direction of the normal to the surface, and tangent friction force that equals

$$f_k = \mu \cdot F_{wall} \cdot \hat{t} \quad (73)$$

while t is the vector tangent to wall in the contact point.

Eventually, after the simulation calculates all of the forces and locations, it draws the robot advancing between two circle-shaped surfaces.

```

close all;
clear all

%% Surfaces parameters %%
rin = 0.4; rout = 0.6; % Internal and external radius of the curve
% Circles data
alpha = 0:0.02:2*pi; xcircle = cos(alpha); ycircle = sin(alpha);

%% Geometrical robot parameters %%
phi = pi/10; % angle in case Bi
W = 0.12; % Width
diag = sqrt(rout^2+rin^2-2*rout*rin*cos(phi)); % diagonal b of the robot
L = sqrt(diag^2-W^2); % Length
mu_limit = rin*sin(phi)/(rout-rin*cos(phi));
COM = 0.5; % COM location (presentage) from the front of the robot
% Initial coordinates of the 4 points of the robot
X_A0 = [-W/2 +COM*L]; X_B0 = [+W/2 +COM*L];
X_C0 = [+W/2 -(1-COM)*L]; X_D0 = [-W/2 -(1-COM)*L];
% Initial COM position
X_COM0 = (rin+W/2); Y_COM0 = 0+L/2;
% Initial orientation of the robot (angle in deg)
Theta_V0 = 0;
% Thrust points location
Cthrust = 0.2; % Location of the thrust point from the
front of the robot
X_Thrust_Left0 = X_A0 - [0 Cthrust*L];
X_Thrust_Right0 = X_B0 - [0 Cthrust*L];

%% Mass, speed and forces %%
% Mass and inertia moment
m = 0.0002; Ip = m*(L^2+W^2)/12;
% Speed of the thrust points
Vin = 0.2;
% Contact properties
Kwall = 200*5*5;
COR = 0.0; % Coefficient of restitution
mu_out = mu_limit*(1+.0001); % mu of the outer radius
mu_in = mu_out; % mu of inner radius
mu_ground = 0.2*0;
mu_thrust = mu_ground*3;
Fin = 0.0002; % in Newton, Input force - pushing force from the back

%% Time %%
dt = 0.0001/5; tend = 15; N = round(tend/dt)+3;

%% Building matrices %%
R = [1,0; 0,1];
XCOM_V = zeros(1,N); XCOM_V(1) = X_COM0;
YCOM_V = zeros(1,N); YCOM_V(1) = Y_COM0;
D_XCOM_V = zeros(1,N); D_YCOM_V = zeros(1,N);
DD_XCOM_V = zeros(1,N); DD_YCOM_V = zeros(1,N);
DD_Theta_V = zeros(1,N); D_Theta_V = zeros(1,N);
Theta_V = zeros(1,N); Theta_V(1) = Theta_V0*pi/180;
penetrationA_V = zeros(1,N); penetrationB_V = zeros(1,N);
penetrationC_V = zeros(1,N); penetrationD_V = zeros(1,N);
penetrationCont_V = zeros(1,N);
XA_M = zeros(2,N); XB_M = zeros(2,N);
XC_M = zeros(2,N); XD_M = zeros(2,N);
X_Thrust_L_M = zeros(2,N); X_Thrust_R_M = zeros(2,N);
XCont_M = zeros(2,N);
F_M = zeros(2,N);
FoutA_N_M = zeros(2,N); FoutA_T_M = zeros(2,N); FoutA_M = zeros(2,N);
FoutB_N_M = zeros(2,N); FoutB_T_M = zeros(2,N); FoutB_M = zeros(2,N);

```

```

FC_M = zeros(2,N); FoutC_N_M = zeros(2,N); FoutC_T_M = zeros(2,N);
FoutC_M = zeros(2,N); FD_M = zeros(2,N); FoutD_N_M = zeros(2,N);
FoutD_T_M = zeros(2,N); FoutD_M = zeros(2,N);
FoutCont_N_M = zeros(2,N); FoutCont_T_M = zeros(2,N);
FoutCont_M = zeros(2,N);
FrictionA_M = zeros(2,N); FrictionB_M = zeros(2,N);
FrictionC_M = zeros(2,N); FrictionD_M = zeros(2,N);
FrictionThrustL_M = zeros(2,N); FrictionThrustR_M = zeros(2,N);
FA_M = zeros(2,N); FB_M = zeros(2,N);
FC_M = zeros(2,N); FD_M = zeros(2,N);

%% Plot %%
figure(1); %clear figure(1);
% Plot circles
plot(rin*xcircle, rin*ycircle, 'k', 'linewidth', 2); hold on;
plot(rout*xcircle, rout*ycircle, 'k', 'linewidth', 2)
i=1; j=1; dtl=0; ii=1; count=0;

for t = 0:dt:tend
    i = i+1;
    % Calculating thrust forces in x,y from Fin (pushing from the back);
    Fx = Fin*(-sin(Theta_V(i-1)));
    Fy = Fin*cos(Theta_V(i-1));
    % Calculating torques
    FA_M(:,i-1) = FoutA_M(:,i-1) + FrictionA_M(:,i-1);
    FB_M(:,i-1) = FoutB_M(:,i-1) + FrictionB_M(:,i-1);
    FC_M(:,i-1) = FoutC_M(:,i-1);
    FD_M(:,i-1) = FoutD_M(:,i-1);
    F_M(:,i) = [Fx;Fy]+FA_M(:,i-1)+FB_M(:,i-1)+FC_M(:,i-1)+FD_M(:,i-1)+FrictionThrustL_M(:,i-1)+FrictionThrustR_M(:,i-1)+FoutCont_M(:,i-1);
    MA_V = cross([R*X_A0';0],[FA_M(:,i-1);0]);
    MB_V = cross([R*X_B0';0],[FB_M(:,i-1);0]);
    MC_V = cross([R*X_C0';0],[FC_M(:,i-1);0]);
    MD_V = cross([R*X_D0';0],[FD_M(:,i-1);0]);
    M_Thrust_L_V = cross([R*X_Thrust_Left0';0],[FrictionThrustL_M(:,i-1);0]);
    M_Thrust_R_V = cross([R*X_Thrust_Right0';0],[FrictionThrustR_M(:,i-1);0]);
    M_Cont_V = cross([XCont_M(:,i)-[XCOM_V(i)
    YCOM_V(i)]';0],[FoutCont_M(:,i-1);0]);
    M_M(i) =
    MA_V(3)+MB_V(3)+MC_V(3)+MD_V(3)+M_Thrust_L_V(3)+M_Thrust_R_V(3)+M_Cont_V
    (3);
    % Acceleration, speed and location in x direction of the COM
    DD_XCOM_V(i) = F_M(1,i)/m; % Acceleration
    D_XCOM_V(i) = DD_XCOM_V(i)*dt + D_XCOM_V(i-1); % Speed
    XCOM_V(i) = D_XCOM_V(i)*dt + XCOM_V(i-1); % Location
    % Acceleration, speed and location in y direction
    DD_YCOM_V(i) = F_M(2,i)/m;
    D_YCOM_V(i) = DD_YCOM_V(i)*dt + D_YCOM_V(i-1);
    YCOM_V(i) = D_YCOM_V(i)*dt + YCOM_V(i-1);
    % Acceleration, speed and location in Theta direction
    DD_Theta_V(i) = M_M(i)/Ip;
    D_Theta_V(i) = DD_Theta_V(i)*dt + D_Theta_V(i-1);
    Theta_V(i) = D_Theta_V(i)*dt + Theta_V(i-1);
    % Calculating the position of the points ABCD and thrust points
    R = [cos(Theta_V(i)) -sin(Theta_V(i)); sin(Theta_V(i))
    cos(Theta_V(i))];
    XY = R*[X_A0; X_B0; X_C0; X_D0; X_Thrust_Left0; X_Thrust_Right0]' +
    [XCOM_V(i); YCOM_V(i)]; %xy locations of all the points and the thrust
    XA_M(:,i) = XY(:,1); XB_M(:,i) = XY(:,2);
    XC_M(:,i) = XY(:,3); XD_M(:,i) = XY(:,4);
    X_Thrust_L_M(:,i) = XY(:,5); X_Thrust_R_M(:,i) = XY(:,6);
    X = XY(1,:); Y = XY(2,:);

```

```

if i>2
    % ABCD corners velocity
    V_A = (XA_M(:,i)-XA_M(:,i-1))/dt;
    V_B = (XB_M(:,i)-XB_M(:,i-1))/dt;
    V_C = (XC_M(:,i)-XC_M(:,i-1))/dt;
    V_D = (XD_M(:,i)-XD_M(:,i-1))/dt;
    % Thrust points velocity
    V_Thrust_L = (X_Thrust_L_M(:,i)-X_Thrust_L_M(:,i-1))/dt;
    V_Thrust_R = (X_Thrust_R_M(:,i)-X_Thrust_R_M(:,i-1))/dt;
else
    V_A=[0 ; 0]; V_B=[0 ; 0]; V_C=[0 ; 0]; V_D=[0 ; 0];
V_Thrust_L=[0 ; 0]; V_Thrust_R=[0 ; 0];
end
Vthrust = [sin(Theta_V(i-1)); -cos(Theta_V(i-1))]*Vin ; % velocity
from pushing from the back
FrictionA_M(:,i) = -V_A/(norm(V_A)+0.001)*m/.4*mu_ground; %m/4 is
the quarter of the weight in Newton
FrictionB_M(:,i) = -V_B/(norm(V_B)+0.001)*m/.4*mu_ground;
FrictionThrustL_M(:,i)=-
(V_Thrust_L+Vthrust)/(norm(V_Thrust_L+Vthrust)+0.001*Vin)*m/.4*mu_thrust
;
FrictionThrustR_M(:,i)=-
(V_Thrust_R+Vthrust)/(norm(V_Thrust_R+Vthrust)+0.001*Vin)*m/.4*mu_thrust
;

% Calculating penetration forces from external wall
% Point A
if norm(XA_M(:,i))>rout
    penetrationA_V(i) = norm(XA_M(:,i))-rout; % size of
penetration of corner A = location relative to the center - outer radius
    FoutA_V(i) = penetrationA_V(i)*Kwall; % force on point A =
penetration * K
    if penetrationA_V(i) < penetrationA_V(i-1) % if the penetration
is getting smaller - reduce the force by restitution coefficient
        FoutA_V(i) = FoutA_V(i)*COR;
    end;
    % Normal force
    FoutA_N_M(:,i) = -FoutA_V(i)*XA_M(:,i)/norm(XA_M(:,i)); % size
of the force * x_A direction = force in point A normal to point A
    % Tangent friction force
    FoutA_T_M(:,i) = mu_out*FoutA_V(i)*[XA_M(2,i); -
XA_M(1,i)]/norm(XA_M(:,i))*sign(-dot([XA_M(2,i); -XA_M(1,i)],V_A));
    % Total force by adding vectors of forces
    FoutA_M(:,i) = FoutA_N_M(:,i)+FoutA_T_M(:,i);
end
% Point B
if norm(XB_M(:,i))>rout
    if count == 0 count = i; end
    penetrationB_V(i) = norm(XB_M(:,i))-rout;
    FoutB_V(i) = penetrationB_V(i)*Kwall;
    if penetrationB_V(i)<penetrationB_V(i-1)
        FoutB_V(i) = FoutB_V(i)*COR;
    end;
    FoutB_N_M(:,i) = -FoutB_V(i)*XB_M(:,i)/norm(XB_M(:,i));
    FoutB_T_M(:,i) = mu_out*FoutB_V(i)*[XB_M(2,i); -
XB_M(1,i)]/norm(XB_M(:,i))*sign(-dot([XB_M(2,i); -XB_M(1,i)],V_B));
    FoutB_M(:,i) = FoutB_N_M(:,i)+FoutB_T_M(:,i);
end
% Point C
if norm(XC_M(:,i))>rout
    penetrationC_V(i) = norm(XC_M(:,i))-rout;
    FoutC_V(i) = penetrationC_V(i)*Kwall;
    if penetrationC_V(i)<penetrationC_V(i-1)
        FoutC_V(i) = FoutC_V(i)*COR;
    end;

```

```

FoutC_N_M(:,i) = -FoutC_V(i)*XC_M(:,i)/norm(XC_M(:,i));
FoutC_T_M(:,i) = mu_out*FoutC_V(i)*[XC_M(2,i); -
XC_M(1,i)]/norm(XC_M(:,i))*sign(-dot([XC_M(2,i); -XC_M(1,i)],V_C));
FoutC_M(:,i) = FoutC_N_M(:,i)+FoutC_T_M(:,i);
end
% Point D
if norm(XD_M(:,i))>rout
    penetrationD_V(i) = norm(XD_M(:,i))-rout;
    FoutD_V(i) = penetrationD_V(i)*Kwall;
    if penetrationD_V(i)<penetrationD_V(i-1)
        FoutD_V(i) = FoutD_V(i)*COR;
    end;
    FoutD_N_M(:,i) = -FoutD_V(i)*XD_M(:,i)/norm(XD_M(:,i));
    FoutD_T_M(:,i) = mu_out*FoutD_V(i)*[XD_M(2,i); -
XD_M(1,i)]/norm(XD_M(:,i))*sign(-dot([XD_M(2,i); -XD_M(1,i)],V_D));
    FoutD_M(:,i) = FoutD_N_M(:,i)+FoutD_T_M(:,i);
end
% Calculating penetration forces on the internal wall
a = (XD_M(2,i)-XA_M(2,i))/(XD_M(1,i)-XA_M(1,i)); % slope of the line
AD = orientation of the robot
b = -1;
c = -XA_M(1,i)*(XD_M(2,i)-XA_M(2,i))/(XD_M(1,i)-
XA_M(1,i))+XA_M(2,i);
xc = -a*c/(a^2+b^2);
yc = -b*c/(a^2+b^2);
if norm([xc yc])<rin && (norm(XA_M(:,i)-[xc yc]')<L)
    XCont_M(:,i) = [xc yc];
    VCont = V_A+V_D; % not real speed, only direction
    penetrationCont_V(i) = rin-norm(XCont_M(:,i));
    FoutCont_V(i) = penetrationCont_V(i)*Kwall;
    if penetrationCont_V(i)<penetrationCont_V(i-1)
        FoutCont_V(i) = FoutCont_V(i)*COR;
    end;
    FoutCont_N_M(:,i) =
FoutCont_V(i)*XCont_M(:,i)/norm(XCont_M(:,i));
    FoutCont_T_M(:,i) = mu_in*FoutCont_V(i)*[XCont_M(2,i); -
XCont_M(1,i)]/norm(XCont_M(:,i))*sign(-dot([XCont_M(2,i); -
XCont_M(1,i)],VCont));
    FoutCont_M(:,i) = FoutCont_N_M(:,i)+FoutCont_T_M(:,i);
else
    if norm(XA_M(:,i))<rin
        penetrationA_V(i) = rin-norm(XA_M(:,i));
        FoutA_V(i) = penetrationA_V(i)*Kwall;
        if penetrationA_V(i)<penetrationA_V(i-1)
            FoutA_V(i) = FoutA_V(i)*COR;
        end;
        FoutA_N_M(:,i) = FoutA_V(i)*XA_M(:,i)/norm(XA_M(:,i));
        FoutA_T_M(:,i) = mu_in*FoutA_V(i)*[XA_M(2,i); -
XA_M(1,i)]/norm(XA_M(:,i))*sign(-dot([XA_M(2,i); -XA_M(1,i)],V_A));
        FoutA_M(:,i) = FoutA_N_M(:,i)+FoutA_T_M(:,i);
    end
    if norm(XD_M(:,i))<rin
        penetrationD_V(i) = rin-norm(XD_M(:,i));
        FoutD_V(i) = penetrationD_V(i)*Kwall;
        if penetrationD_V(i)<penetrationD_V(i-1)
            FoutD_V(i) = FoutD_V(i)*COR;
        end;
        FoutD_N_M(:,i) = FoutD_V(i)*XD_M(:,i)/norm(XD_M(:,i));
        FoutD_T_M(:,i) = mu_in*FoutD_V(i)*[XD_M(2,i); -
XD_M(1,i)]/norm(XD_M(:,i))*sign(-dot([XD_M(2,i); -XD_M(1,i)],V_D));
        FoutD_M(:,i) = FoutD_N_M(:,i)+FoutD_T_M(:,i);
    end
    if norm(XC_M(:,i))<rin
        penetrationC_V(i) = rin-norm(XC_M(:,i));

```

```

        FoutC_V(i) = penetrationC_V(i)*Kwall;
        if penetrationC_V(i)<penetrationC_V(i-1)
            FoutC_V(i) = FoutC_V(i)*COR;
        end;
        FoutC_N_M(:,i) = FoutC_V(i)*XC_M(:,i)/norm(XC_M(:,i));
        FoutC_T_M(:,i) = mu_in*FoutC_V(i)*[XC_M(2,i); -
XC_M(1,i)]/norm(XC_M(:,i))*sign(-dot([XC_M(2,i); -XC_M(1,i)],V_D));
        FoutC_M(:,i) = FoutC_N_M(:,i)+FoutC_T_M(:,i);
    end
end

% Plot
dt1 = dt1+dt; % counting larger dt for drawing only every 0.05 sec
if dt1>0.05
    dt1 = 0;
    figure(1); grid off
    if ii>1; delete(p); delete(line1); end
    p = patch(X(:,1:4),Y(:,1:4), [0 0.447 0.741]);
    line1 = line([XA_M(1,i) XB_M(1,i)], [XA_M(2,i)
XB_M(2,i)], 'linewidth',3, 'color', 'k');
    axis equal; axis([-1.1*rout 1.1*rout -1.1*rout 1.1*rout] );
drawnow
    set(gca, 'fontname', 'Times New Roman', 'fontsize',12);
    % pause(0.0);
    ii = ii+1;
end
end

%% Graphs plot %%
Velocity_V = (D_XCOM_V.^2+D_YCOM_V.^2).^(.5); % COM total velocity
FoutB_N_V = (FoutB_N_M(1,:).^2+FoutB_N_M(2,:).^2).^(.5);
FoutB_T_V = (FoutB_T_M(1,:).^2+FoutB_T_M(2,:).^2).^(.5);
FoutD_N_V = (FoutD_N_M(1,:).^2+FoutD_N_M(2,:).^2).^(.5);
FoutD_T_V = (FoutD_T_M(1,:).^2+FoutD_T_M(2,:).^2).^(.5);
time_V = 0:dt:tend;

f = figure; movegui(f, 'south')
plot(time_V, Velocity_V(1:length(time_V)), grid on
xlabel('Time (s)'); ylabel('Velocity of COM (m/s)');
set(gca, 'GridLineStyle', '--', 'fontname', 'Times New
Roman', 'fontsize',12);

f = figure; movegui(f, 'southwest')
plot(time_V, smooth(FoutB_N_V(1:length(time_V)),100), grid on
hold on; plot(time_V, smooth(FoutB_T_V(1:length(time_V)),100));
xlabel('Time (s)'); ylabel('Force of point B (N)'); legend('Normal
force', 'Tangential force')
set(gca, 'GridLineStyle', '--', 'fontname', 'Times New
Roman', 'fontsize',12);

f = figure; movegui(f, 'northwest')
plot(time_V, smooth(FoutD_N_V(1:length(time_V)),100), grid on
hold on; plot(time_V, smooth(FoutD_T_V(1:length(time_V)),100));
xlabel('Time (s)'); ylabel('Force of point D (N)'); legend('Normal
force', 'Tangential force')
set(gca, 'GridLineStyle', '--', 'fontname', 'Times New
Roman', 'fontsize',12);

```

[H] Experiments Results

Table 9.3: Experiments results of the motion between two surfaces and inside tubes

		Backward					Forward								
		L mm	Δx mm	Time sec	Δt sec	ATR mm/sec	L mm	Δx mm	Time sec	Δt sec	Velocity mm/sec				
All brass	Surfaces	1	297	290	3.29	15.77	18.4	2	25	237	20.14	10.47	22.6		
			7		19.22				262		30.28				
		3	248	227	32	9.33		24.3	4	48	178	0.08		7.43	23.9
			21		41.1					226		7.21			
	Tube 1mm	1	182	130	1.03	7.03	18.5		2	58	100	8.16	5.27	19.0	
			52		8.04					158		13.24			
		3	159	108	14.2	5.77		18.7	4	58	101	20.28	5.27		19.2
			51		20.13					159		26.06			
	Tube 2mm	1	187	139	2.23	7.70	18.1		2	55	106	10.29	5.73	18.5	
			48		10.14					161		16.21			
		3	161	112	17.15	6.37		17.6	4	54	112	24.07	5.90		19.0
			49		23.26					166		30.04			
Brass helix	Surfaces	1	250	192	2.2	6.80	28.2		2	20	238	12.21	8.67	27.5	
			58		9.14					258		21.11			
		3	262	139	22.07	5.07		27.4	4	44	226	30.29	8.27		27.3
			123		27.09					270		39.07			
	Tube 1mm	1	185	133	0.21	7.30	18.2		2	50	114	8.15	6.73	16.9	
			52		8					164		15.07			
		3	162	107	15.26	5.83		18.3	4	55	109	22.21	6.70		16.3
			55		21.21					164		29.12			
	Tube 2mm	1	194	138	0.18	6.97	19.8		2	50	115	8.04	6.73	17.1	
			56		7.17					165		14.26			
		3	159	108	15.18	5.70		18.9	4	52	116	22.19	6.40		18.1
			51		21.09					168		29.01			

Table 9.4: Calculated average and STD from the experiments data

	Forward Velocity	Backward Velocity	Velocity
	mm/sec	mm/sec	mm/sec
Average of Surfaces	24.6	25.3	25.0
STD	4.5	2.4	3.4
Average of 1mm tube	18.4	17.8	18.1
STD	0.2	1.5	1.0
Average of 2mm tube	18.6	18.2	18.4
STD	1.0	0.8	0.9
Average of Tubes	18.5	18.0	18.3
STD	0.7	1.1	0.9
Maximum velocity between surfaces	28.2	27.5	28.2
Maximum velocity in tubes	19.8	19.2	19.8
Total Average	20.5	20.5	20.5
STD	3.8	3.8	3.8
Total Maximum velocity	28.2	27.5	28.2

מחקר זה עוסק במידול, ניסויים וחקר תנועה של רובוט גל מיניאטורי בשם SAW – Single Actuator Wave robot. מטרת המחקר היא פיתוח רובוט זעיר שיוכל לשמש בשכלול ושיפור פרוצדורות רפואיות בגוף האדם, כמו למשל במעיים, על ידי שכלול ומזעור של הרובוט SAW הקיים. בנוסף מבוצע ניתוח מקיף של תנועת הרובוט בסביבות שונות וחישוב התנאים שבהם הרובוט מתקדם.

ראשית, מוצגים הדגמים הקודמים של הרובוט ופירוט של דרישות המוצר. מבנה הרובוט והתכן שלו מפורטים, ומוצג הסבר על מכניקת תנועת הרובוט וצורת ההתקדמות שלו. מוצגים מספר מודלים של הרובוט שנבנו בנוסף על פירוט החומרים ושיטות הייצור של הדגמים השונים.

נוסף על כך, מוצגת אנליזה מפורטת של תנועת הרובוט בסביבות ומצבי תנועה שונים. תחילת האנליזה בפיתוח שני מודלים של תנועה לייצוג תנועת הרובוט בשני מקרים שונים: תנועה בין שני משטחים ישרים ותנועה על פני משטח ישר יחיד. עבור כל מודל מחושבים תנאי ההתקדמות של הרובוט שהם מתאפשרת תנועה. עבור התנועה על פני משטח ישר ניתן לראות שהתנועה אינה רציפה, ומבוצע שימוש בסימולציה ממוחשבת על מנת לדמות את תנועת ההתקדמות-החלקה של הרובוט, המושפעת מפרמטרים שונים.

בהמשך מוצג ניתוח ומידול של תנועת הרובוט בין שני משטחים מעוקלים באוריינטציות תנועה שונות. תנועת הרובוט מנותחת עבור תנאים גיאומטריים שונים של הרובוט המשתלבים עם תנאים שונים של המשטחים המעוקלים.

לסיום, מוצגים מספר ניסויים שבוצעו עם דגמים שונים של הרובוט, על מנת לתקף את האנליזה והסימולציה שבוצעו. מוצגות מערכות ניסוי שונות שנבנו לצורך הניסויים, הכוללות משטחים וצינורות גמישים המיוצרים מסיליקון, בנוסף על מערכת ניסוי למדידת כוחות הפועלים על הרובוט בזמן תנועתו בתוך הצינורות הגמישים. לאחר מכן מתוארים הניסויים שבוצעו עם הרובוט בין ובתוך המשטחים הגמישים, וכמו כן ניסויים שבוצעו בתוך מעיים של חזיר.



אוניברסיטת בן גוריון בנגב

הפקולטה למדעי ההנדסה

המחלקה להנדסת מכונות

ניתוח תנועה, מידול וניסויים של רובוט גלי בסביבות שונות

חיבור זה מהווה חלק מהדרישות לקבלת תואר מוגיסטר בהנדסה

מאת: לי-היא דרורי

מנחה: ד"ר דוד זרוק

תאריך: 19.11.2019

מחברת: לי-היא דרורי

תאריך: 19.11.2019

מנחה: דוד זרוק

תאריך: _____

אישור יו"ר ועדת תואר שני מחלקתית: _____



אוניברסיטת בן גוריון בנגב

הפקולטה למדעי ההנדסה

המחלקה להנדסת מכונות

ניתוח תנועה, מידול וניסויים של רובוט גלי בסביבות שונות

חיבור זה מהווה חלק מהדרישות לקבלת תואר מוגיסטר בהנדסה

מאת: לי-היא דרורי

מנחה: ד"ר דוד זרוק